

# **Mathematical Modeling and Testing of a Loop Heat Pipe using a Two – Way Pressure Regulating Valve**

by

**Juan Posada**

A thesis submitted to the Faculty of Graduate and Postdoctoral Affairs in  
partial fulfilment of the requirements for the degree of

**Master of Applied Science**

in

**Aerospace Engineering**

Carleton University  
Ottawa, Ontario

© 2018, Juan Posada

## ABSTRACT

A loop heat pipe (LHP) is a heat transfer device that uses the vaporization of a working fluid to transfer heat from an evaporation section to a condensing section. The operating characteristics of a LHP with a two-way pressure regulating valve (PRV) is experimentally investigated using a flight-qualified LHP. Experiments suggest that an orifice within the PRV causes a premature start-up. It is determined that the LHP is unable to control the evaporator temperature to 31 °C roughly after 130 W under test conditions. The LHP is found to be more sensitive to changes in sink temperatures when operating at higher powers. A steady-state LHP model is developed and is found to compare well with experimental results. It is determined that modeling the effects of the PRV on the LHP operation is not feasible using measurements due to the extreme sensitivity of the model to small changes in fluid pressure.

## ACKNOWLEDGEMENTS

Firstly, I would like to express my sincere gratitude to my supervisor, Prof. Tarik Kaya, for giving me the opportunity to further my education and for providing me with an experience that I will always remember. His guidance, support, patience, flexibility and immense knowledge helped me reach where I am today, and I could not have imagined having a better advisor and mentor.

I thank my lab partner Hooman Jazebizadeh for the many hours he spent helping me throughout my research. His friendship, guidance, and mentorship over the duration of my thesis were instrumental in me reaching this goal.

I would like to thank my friends for their support, encouragement, and sometimes needed distraction. These people include, but are not limited to Noah Marion, Leon Lewis, Ahmed Farag, Mohamed Emara, Shawn Somers-Neal, Tejas Sawant, and Shannon Farquharson.

I would like to give credit to the individuals who helped review my thesis: Cory Fraser, Alex Crain, and Shawn Somers-Neal. Their time is very much appreciated.

Last but not least, I would like to thank my family: Vilma, Felipe and Gabriel for their love and support. Thank you for always being there and helping me become a better version of myself every day.

## TABLE OF CONTENTS

ABSTRACT .....	ii
ACKNOWLEDGEMENTS .....	iii
TABLE OF CONTENTS .....	iv
LIST OF TABLES .....	vii
LIST OF FIGURES .....	viii
ABBREVIATIONS .....	x
NOMENCLATURE .....	xi
<b>CHAPTER 1 INTRODUCTION .....</b>	<b>1</b>
1.1 BACKGROUND .....	1
1.1.1 Conventional Heat Pipes .....	1
1.1.2 Loop Heat Pipes .....	2
1.1.3 Heat Pipe Components .....	3
1.1.3.1 Working Fluid .....	3
1.1.3.2 Wick .....	4
1.1.3.3 Container .....	4
1.2 RESEARCH OBJECTIVES .....	4
1.3 ORGANIZATION .....	5
<b>CHAPTER 2 LITERATURE ANALYSIS .....</b>	<b>7</b>
2.1 LHP OPERATING PRINCIPLES .....	7
2.1.1 Fundamentals .....	8
2.1.2 Thermodynamic Cycle .....	9
2.2 LHP OPERATING CHARACTERISTICS .....	11
2.2.1 Operating Temperature .....	12
2.2.2 Start-up .....	15
2.2.3 Temperature Hysteresis .....	17
2.2.4 Orientation .....	17
2.2.5 Temperature Oscillations .....	18
2.3 LHP TEMPERATURE CONTROL TECHNIQUES .....	20
2.3.1 Temperature Control Methods .....	20
2.3.1.1 External Heating .....	20
2.3.1.2 Thermal Coupling of Transportation Lines .....	21
2.3.2 Pressure Regulating Valves .....	22
2.3.2.1 Three-way PRVs .....	22
2.3.2.2 Two-way PRVs .....	24

<b>CHAPTER 3</b>	<b>TEST SETUP</b>	<b>26</b>
3.1	APPARATUS	26
3.1.1	Loop Heat Pipe	27
3.1.2	Heating System	29
3.1.3	Cooling System	30
3.1.4	Data Acquisition System	31
3.2	INSTRUMENTATION	32
3.3	UNCERTAINTY ANALYSIS	33
3.3.1	Input Power Uncertainty	33
3.3.2	Thermocouple Uncertainty and Variation	36
3.3.3	Chiller Temperature Variation	37
3.3.4	Ambient Temperature Variation	38
3.4	TEST PLAN	39
<b>CHAPTER 4</b>	<b>TEST RESULTS AND LHP CHARACTERIZATION</b>	<b>41</b>
4.1	START-UP	41
4.2	POWER CYCLING	48
4.3	SINK CYCLING	55
<b>CHAPTER 5</b>	<b>MATHEMATICAL MODEL</b>	<b>59</b>
5.1	OVERVIEW	59
5.1.1	Governing Equations	60
5.1.2	Discretization	62
5.1.3	Solid Cell and Fluid Cell Properties	63
5.1.4	General Algorithm	64
5.2	LHP COMPONENT MODELING	67
5.2.1	Inputs and Initial/ Boundary Conditions	67
5.2.2	Evaporator	68
5.2.3	Transportation Lines and Condenser	69
5.2.4	Compensation Chamber	72
5.2.5	Wick	74
5.3	PRESSURE DROP	75
5.4	IN-TUBE HEAT TRANSFER COEFFICIENT	76
5.4.1	Single-Phase Fluid	77
5.4.2	Two-Phase Fluid	78
5.4.3	Transition Regimes	82
5.5	RESULTS & VALIDATION OF MODEL WITHOUT PRV	83

5.5.1	Results .....	84
5.5.2	Experimental Validation .....	86
5.6	PRV IMPLEMENTATION AND RESULTS .....	88
<b>CHAPTER 6</b>	<b>CONCLUSIONS AND RECOMMENDATIONS .....</b>	<b>91</b>
6.1	CONCLUSIONS .....	91
6.2	RECOMMENDATIONS FOR FUTURE WORK .....	92
6.2.1	Experimental Setup .....	92
6.2.2	LHP Testing .....	93
6.2.3	Mathematical Modeling .....	93
<b>REFERENCES</b>	.....	<b>94</b>
<b>APPENDIX A</b>	Wall Temperature Iteration .....	<b>A-1</b>
<b>APPENDIX B</b>	Heat Leak Iteration .....	<b>B-1</b>

## LIST OF TABLES

Table 1: Loop Heat Pipe Physical Properties .....	28
Table 2: Testing Plan Outline .....	39
Table 3: Condenser Behaviour by Thermocouple .....	53

## LIST OF FIGURES

Figure 1: Schematic of a Conventional Heat Pipe.....	2
Figure 2: Loop Heat Pipe Schematic.....	3
Figure 3: Typical Loop Heat Pipe Evaporator (modified) .....	7
Figure 4: (a) LHP Schematic with Points of Interest (b) Pressure vs. Temperature LHP Working Cycle .....	10
Figure 5: LHP Thermal Resistance Network .....	12
Figure 6: LHP Operating Temperature vs. Evaporator Heat Load.....	14
Figure 7: Start-up Scenarios .....	16
Figure 8: LHP Saturation Temperature vs. Input Power .....	21
Figure 9: Three-Way Pressure Regulating Valve Schematic.....	22
Figure 10: PRV Valve Position vs. Working Fluid Pressure.....	23
Figure 11: Two-Way Pressure Regulating Valve Schematic .....	24
Figure 12: Pressure-Temperature diagram of LHP under two scenarios .....	25
Figure 13: Complete Experimental Setup .....	27
Figure 14: IberEspacio Loop Heat Pipe System .....	27
Figure 15: (a) Evaporator Saddle, (b) Condenser Panel .....	28
Figure 16: Evaporator with Cartridge Heater Installed .....	29
Figure 17: Heating System Equipment with Insulated Evaporator.....	30
Figure 18: Heat Exchanger CAD Model .....	30
Figure 19: Heat Exchanger Assembly .....	31
Figure 20: LHP Thermocouple Placement and Schematic .....	32
Figure 21: Condenser Pipe route inside Condenser Panel.....	33
Figure 22: Input Power Percent Uncertainty.....	35
Figure 23: Thermocouple Standard Deviation .....	37
Figure 24: Chiller vs. Thermocouple Standard Deviation .....	38
Figure 25: Test Ambient Temperature Readings.....	38
Figure 26: Test No. 1A - 10 W Start-up Test.....	43
Figure 27: PRV Calibrated Orifice .....	43
Figure 28: Inlet and Outlet Thermocouple Readings for 10 W Startup Test..	44
Figure 29: Test No. 1B - 25 W Start-up Test.....	46
Figure 30: Test No. 1C - 50 W Start-up Test.....	47
Figure 31: Test No. 1D - 100 W Start-up Test.....	47
Figure 32: Test No. 2A – 10/25/50/100/50/25/10 W Power Cycle.....	48
Figure 33: Test No. 2A - Temperatures surrounding PRV .....	50
Figure 34: Test No. 2D - Large Range Power Cycle.....	51
Figure 35: Test No. 2D – Condenser Temperature Readings.....	52
Figure 36: LHP Performance Curve.....	54
Figure 37: Modified LHP Operating Temperature.....	55
Figure 38: Sink Cycle Evaporator Temperatures .....	56
Figure 39: Test No. 3D – 100 W Constants Sink Cycle.....	57

Figure 40: Test No. 3D – Condenser Temperature Readings.....	58
Figure 41: Staggered grid discretization of LHP components .....	62
Figure 42: General Steady-State Model Algorithm .....	66
Figure 43: Wall Temperature Iteration Algorithm.....	70
Figure 44: Flow Patterns Schematic (modified) .....	78
Figure 45: Geometrical parameters for two-phase flow in a circular tube.....	79
Figure 46: Predicted NH <sub>3</sub> flow pattern map (modified) .....	81
Figure 47: Model Heat Transfer Coefficient Distribution along LHP.....	83
Figure 48: Steady-State Model Performance Curve .....	84
Figure 49: Model Temperature and Quality at LHP locations at 15 W.....	86
Figure 50: Model Temperature and Quality at LHP locations at 110 W.....	86
Figure 51: Experimental vs. model results .....	87
Figure 52: Standard Model vs Pressure Adjusted Results.....	88
Figure 53: Derived PRV Pressure Drop Law .....	89
Figure 54: Mathematical Model with PRV effect modelled .....	90

## ABBREVIATIONS

CC	Compensation Chamber
HTC	Heat Transfer Coefficient
IE	IberEspacio
LHP	Loop Heat Pipe
NCG	Non-Condensable Gas
NIST	National Institute of Standards and Technology
PRV	Pressure Regulated Valve
REFPROP	Reference Fluid Thermodynamic and Transport Property Database

## NOMENCLATURE

Symbol	Description	Unit
Latin		
$A$	Surface area	$m^2$
$c$	Specific heat	$J kg^{-1}K^{-1}$
$D$	Diameter	$m$
$e$	Specific internal energy	$J kg^{-1}$
$Fr$	Froude number	
$f$	Friction factor	
$f_i$	Interfacial roughness correction factor	
$G$	Thermal conductance and Mass flux	$W K^{-1}$ $kg m^{-2}s^{-1}$
$g$	Gravitational acceleration	$m s^{-2}$
$h$	Heat transfer coefficient	$W m^{-2}K^{-1}$
$h$	Specific enthalpy	$J kg^{-1}$
$h_{liq,d}$	Height of stratified liquid	
$I$	Current	$A$
$k$	Thermal conductivity	$W m^{-1}K^{-1}$
$L$	Length	$m$
$m$	Mass	$kg$
$\dot{m}$	Mass Flow Rate	$kg s^{-1}$
$N$	Number of readings	
$Nu$	Nusselt number	
$P$	Pressure and Power	$Pa$ $W$
$Pr$	Prandtl number	
$P_{id}$	Length of interface	
$\dot{Q}$	Rate of heat transfer	$W$
$\dot{q}$	Heat flux	$Wm^{-2}$
$R$	Radius	$m$
$Re$	Reynolds number	
$s$	Sample standard deviation	
$T$	Temperature	$K$
$t$	Time	$s$
$U$	Uncertainty	
$u$	Velocity	$m s^{-1}$
$V$	Volume and Voltage	$m^3$ $V$
$v$	Specific volume	$m^3 kg^{-1}$
$We$	Weber number	
$X$	Vapour quality	
$\bar{x}$	Mean value	
$Z$	Height	$m$

Greek		
$\alpha$	Void fraction	
$\Delta$	Difference	
$\delta$	liquid film thickness	
$\varepsilon$	Surface roughness	
$\theta$	Angle	<i>Rad</i>
$\kappa$	Permeability	$m^2$
$\lambda$	Latent heat of vaporization	$J kg^{-1}$
$\mu$	Viscosity	$N s m^{-2}$
$\xi$	Pressure drop coefficient	
$\rho$	Density	$kg m^{-3}$
$\sigma$	Surface tension	$N m^{-1}$
$\varphi$	Any fluid property	
$\omega$	Wick porosity	
Subscripts		
<i>2ph</i>	Two-phase	
<i>amb</i>	Ambient	
<i>c</i>	Characteristic	
<i>cap</i>	Capillary	
<i>cc</i>	Compensation chamber	
<i>con</i>	Condenser	
<i>CV</i>	Control volume	
<i>e</i>	Evaporator	
<i>eff</i>	Effective	
<i>g</i>	Gravity	
<i>gro</i>	Grooves	
<i>homo</i>	Homogeneous	
<i>hl</i>	Heat leak	
<i>i</i>	Node number in staggered grid	
<i>in</i>	Coming in	
<i>int</i>	Interface	
<i>j</i>	Junction number in staggered grid	
<i>liq</i>	Liquid	
<i>lam</i>	Laminar	
<i>out</i>	Going out	
<i>p</i>	Constant pressure	
<i>sat</i>	Saturated	
<i>strat</i>	Stratified	
<i>sc</i>	Subcooled	
<i>tot</i>	Total	
<i>vap</i>	Vapour	
<i>w</i>	Wick	

# CHAPTER 1 INTRODUCTION

## 1.1 BACKGROUND

Advancements in the space industry heavily depend on the ability of satellites to accomplish a wider range of tasks without impacting size and weight. Although technology has been quickly evolving towards smaller and more powerful electronics, major advancements have been limited by the large heat outputs that result from the increasing levels of power and integration complexity [1]. As an improvement to already existing thermal control techniques, heat pipes originated around the early 1960s as a device capable of operating under various orientations. The extensive development of heat pipe technology has led to a variety of heat pipes, in terms of geometry, function and/or operation, each designed to fit specific heat rejection and re-distribution requirements for particular applications.

### 1.1.1 Conventional Heat Pipes

In general terms, a heat pipe is a passive two-phase heat transfer device comprised of a sealed tube filled with saturated fluid. In operation, one end of the device is exposed to a heat source (evaporator region) while the opposite end is exposed to a cold region (condenser). At the evaporator, energy is transferred into the fluid causing it to change from liquid to vapour. Vapour then travels towards the condenser where heat is released and the fluid condenses. Finally, a wicking structure is fixed to the inside surface of the tube to induce capillary forces so as to return the condensate towards the evaporator. A schematic of a conventional heat pipe is shown in Figure 1.

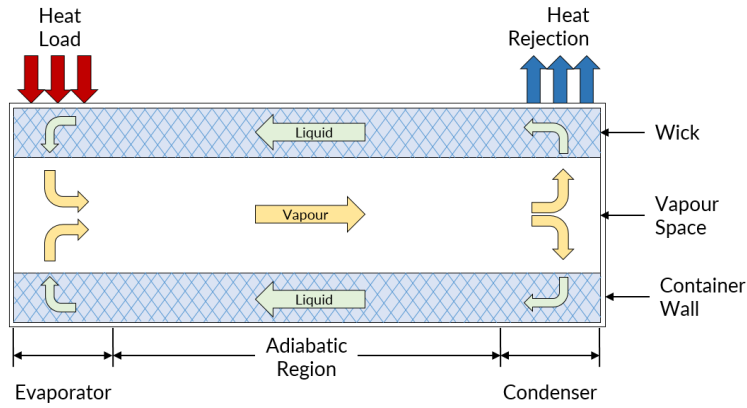


Figure 1: Schematic of a Conventional Heat Pipe

The initial concept of the heat pipe was proposed by Gaugler in 1942; nevertheless, it was not until 1963, when Grover filed a patent for the ‘heat pipe’ backed up with theoretical analysis and experimental results, that the development of this device was pushed forward [2]. Although the use of heat pipes broadened to applications in the areas (e.g. electronics cooling, air conditioning, engine cooling, etc.), emphasis was placed on the use of heat pipes in satellite applications [2]. The first space flight of heat pipes took place in 1967 [3] and since then have been used extensively on spacecraft as thermal control devices.

### 1.1.2 Loop Heat Pipes

As the development of heat pipes continued, Loop Heat Pipes (LHPs) originated in order to meet with increasingly demanding thermal control problems of high-end spacecraft electronics. LHPs have proven particularly useful given their high heat transport capability, efficiency, flexibility, ability to passively transport heat over long distances, and their reduced sensitivity to orientation within a gravitational field [4].

The LHP is comprised of five main components: evaporator, vapour line, condenser, liquid line, and compensation chamber (CC), arranged in a configuration as shown in Figure 2. Unlike traditional heat pipes, LHPs have dedicated lines for vapour and liquid to reduce pressure losses by minimizing thermal and viscous interactions between fluid counter flows [4]. Additionally, the wick in LHPs is designed to only span the evaporation zone. This is done

in order to reduce the fluid travel distance through the wick which would otherwise cause pressure losses, reducing its ability to transfer heat over large distances.

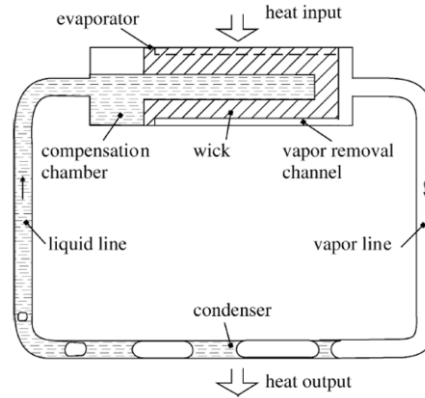


Figure 2: Loop Heat Pipe Schematic [4]

### 1.1.3 Heat Pipe Components

In any heat pipe configuration, there are three common components: the working fluid, wick, and container. Depending on the combination of materials for each of these components, heat pipes can be designed to work in entirely different scenarios and applications. Although LHPs are comprised of more components, most of materials used in conventional heat pipes still apply to the LHP overall system.

#### 1.1.3.1 Working Fluid

The working fluid is largely selected based on the operating vapour temperature range for each specific application; nonetheless, different fluids may satisfy these temperature requirements. Additional factors must be considered such as its compatibility with other heat pipe materials and the wettability of the wick. A working fluid is selected such that it exhibits [2]:

- Good thermal stability to avoid thermal degradation;
- High latent heat to transport large amounts of heat;
- High thermal conductivity to minimize the radial temperature gradient across the heat pipe;
- Low liquid and vapour viscosities to reduce resistance to fluid flow; and
- High surface tension to generate larger capillary forces so as to improve heat pipe performance against gravity.

### **1.1.3.2 Wick**

Selection of the wick is closely linked to the properties of the working fluid because the wick's purpose is to generate sufficient capillary pressure to transport the working fluid. Arguably the most important factor of the wick is its structure, since it can be designed to optimize transport of fluid flow (space environment) or to increase heat transfer (gravity assisted heat pipes) [2].

The wick pore size largely dictates the capillary forces which can be generated by the menisci (refer to Section 2.1). Smaller pore size is generally preferred when capillary forces are required to move fluid in unfavourable directions, as commonly observed in space applications [4]. On the other hand, for horizontal or gravity assisted heat pipes, larger pores prove beneficial due to the resulting reduction in hydraulic resistance caused by the wick [4].

### **1.1.3.3 Container**

The main function of the container is to isolate the working fluid from the exterior. It permits a differential pressure across the walls and allows heat transfer to and from the working fluid. When selecting an appropriate container, the following characteristics are taken into consideration [2]:

- Compatibility with the working fluid and exterior environment;
- A high strength-to-weight ratio (especially for space applications);
- Thermal conductivity to minimize a temperature drop between the source of heat load and the wick; and
- Wettability such that the contact angle between working fluid and container is close to zero.

## **1.2 RESEARCH OBJECTIVES**

The main objective of this study is to gain an understanding of the behaviour and operational characteristics of LHPs with two-way pressure regulating valves for accurate thermal control. This is accomplished through the testing of a flight-proven LHP manufactured by IberEspacio in Spain and the development of a steady-state mathematical model.

The following activities were considered to achieve the above-mentioned objectives:

- Develop the steady-state model in MATLAB using polynomials for estimating working fluid properties;
- Improve the steady-state model by implementing functions in MATLAB that use the Reference Fluid Thermodynamic and Transport Properties Database (REFPROP) for a more accurate estimation of fluid properties;
- Compare various methods for calculating heat transfer coefficient;
- Implement new methods for calculating heat transfer coefficient in the steady-state model;
- Design a heat exchanger system to adapt the flight-like model to a ground testing environment;
- Instrument the LHP for testing;
- Establish an experimental approach and testing procedures; and
- Develop correlations to introduce the effects of a two-way pressure regulating valve on the steady-state model based on experiment data.

### 1.3 ORGANIZATION

This thesis is organized into the following six chapters:

*Chapter 1 – Introduction:* Introduces a background on the history of heat pipes and an overview of the main research objectives and organization of the thesis.

*Chapter 2 – Literature Analysis:* Presents the fundamental concepts and theory behind the operation of LHPs and temperature control techniques.

*Chapter 3 – Test Setup:* Presents the necessary information on the experimental apparatus and methods used for testing the LHP. An uncertainty analysis is also presented.

*Chapter 4 – Test Results and LHP Characterization:* Presents the results of the experimental work and a detailed discussion and analysis of the operation of the LHP based on the results.

*Chapter 5 – Mathematical Model:* Presents the theory and techniques used for the development of the LHP steady-state model. Provides results for the model operating as a non-regulated LHP and results implementing a law describing the effects of the PRV.

*Chapter 6 – Conclusion and Recommendations:* Summarizes the work completed, provides a conclusion, and discusses future work and recommendations.

# CHAPTER 2 LITERATURE ANALYSIS

## 2.1 LHP OPERATING PRINCIPLES

The operating principles that govern the functioning of LHPs are, in essence, very similar to those of conventional heat pipes. However, as illustrated in Section 1.1, various LHP components are structured and organized in a different fashion. The evaporator section is arguably the most dissimilar component when compared to conventional heat pipes given the more complex role of the wicking structure.

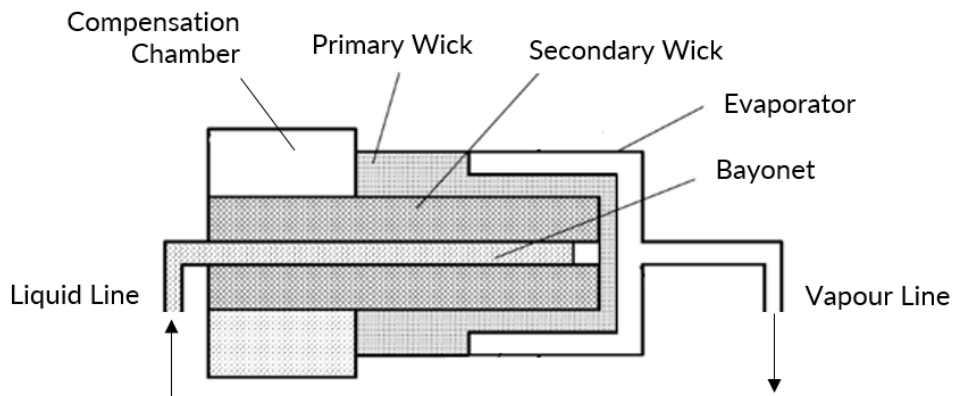


Figure 3: Typical Loop Heat Pipe Evaporator (modified) [5]

The evaporator section in LHPs is defined by the evaporator, compensation chamber and a primary and secondary wick as shown above. Before start-up, the wick is saturated with liquid. As a heat load is applied on the evaporator, liquid evaporates at the free surface of the wick in the evaporator and CC. This occurs at different rates due to differences in thermal resistance of the primary

and secondary wick. Temperature and vapour pressure in the evaporator become higher than that of the CC and the wick acts as a “hydraulic lock,” such that vapour cannot penetrate into the CC through the wick due to capillary forces [4]. Finally, the increasing pressure difference between the evaporator and the compensation chamber causes the working fluid to displace from the evaporator, through the vapour line, condenser, and liquid line, back to the compensation chamber in a loop as shown in Figure 2. This pressure difference can be considered the driving force behind LHP operation. The subsequent section provides a more in-depth explanation behind the operating principles that govern the functioning of LHPs.

### 2.1.1 Fundamentals

As previously mentioned, the pressure difference between the evaporator and CC as a result of the temperature difference across the wick is the driving mechanism for the circulation of working fluid. Since this pressure difference is caused by the applied heat load, the LHP operates without the need of an external pump. In order for the LHP to function, the pressure difference developed across the wick must overcome the system total pressure drop (sum of frictional pressure drops in the evaporator grooves, vapor line, condenser, liquid line, and evaporator wick plus any static pressure drop due to gravity) [5]:

$$\Delta P_{tot} = \Delta P_{groove} + \Delta P_{vap} + \Delta P_{con} + \Delta P_{liq} + \Delta P_w + \Delta P_g \quad (1)$$

The pressure difference between evaporator and CC is attributed to the menisci formed along the pores of the wick and is thus referred to as capillary pressure:

$$\Delta P_{cap} = \frac{2\sigma}{R} \cos \theta \quad (2)$$

where  $\sigma$  is the surface tension of the working fluid,  $R$  is the radius of curvature of the meniscus in the wick, and  $\theta$  is the contact angle between the liquid and the wick. The meniscus radius of curvature automatically adjusts itself such

that the resulting capillary pressure is equal to the system total pressure drop; however, it cannot be smaller than the wick pore radius. At this point, the wick has reached its maximum pumping capacity [5].

The pressure drop along the liquid and vapour transportation lines and the condenser heavily depend on conditions of the flow such as phase and Reynolds number. Pressure losses due to the LHP orientation in a gravitational field can be found using:

$$\Delta P_g = \rho g L \sin \theta \quad (3)$$

Finally, pressure losses across the wick heavily depend on the type of wicking structure being used (homogeneous or non-homogeneous) and may change in a case-by-case basis.

### **2.1.2 Thermodynamic Cycle**

To analyze LHP operation, the pressure-temperature relation of the working fluid at various points along the LHP can be plotted with respect to the fluid saturation line as shown in Figure 4. This graph provides a useful insight into the working cycle of the LHP.

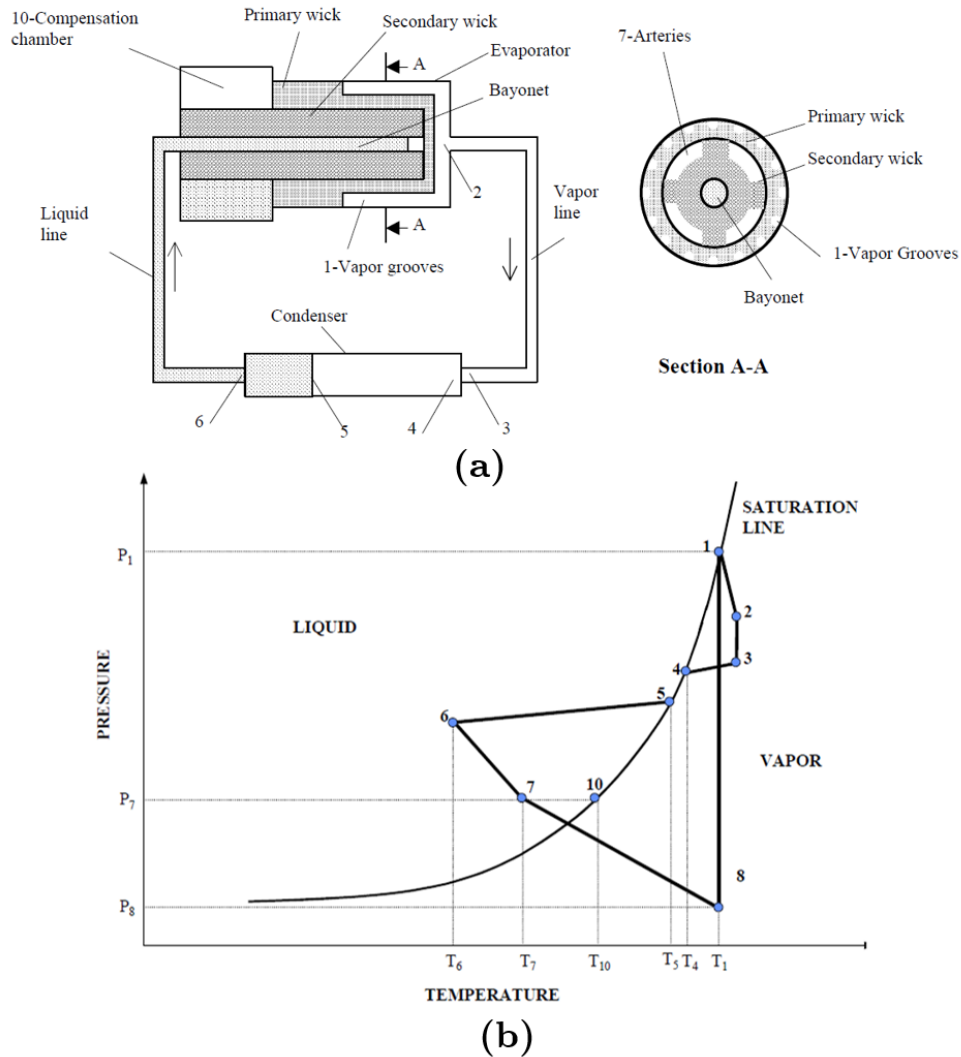


Figure 4: (a) LHP Schematic with Points of Interest (b) Pressure vs. Temperature LHP Working Cycle [5]

The cycle shown above starts at point 1 which is located just above the evaporating surface of the wick menisci in the evaporator. As vapour moves along the vapour grooves to the evaporator exit (point 2) friction causes a drop in pressure but temperature continues to increase due to heat from the evaporator walls. Movement through the vapour line (point 2 to 3) is ideally isothermal with a pressure drop due to friction. Having reached the condenser (point 3), vapour is condensed with almost negligible pressure losses until reaching saturation (point 4), commonly referred to as the vapour-liquid interface. As vapour moves through the condenser, it is further cooled until condensation is complete (point 5), and then subcooled until exiting the condenser at point 6. Between points 6 and 7, liquid is moved towards the evaporator core (considered an extension of the CC) and a large pressure drop

is observed. Unlike the vapour line, temperature in the liquid line is more likely to increase or decrease due to parasitic heat transfer with the environment. As the fluid moves within the CC, it travels through the wick which causes a pressure drop and an increase in temperature until reaching the vicinity of the evaporating menisci at point 8 [5].

Based on the working cycle described above, it can be deduced that for LHP operation, a pressure difference between the evaporator and compensation chamber can only exist if there is a proportional difference in saturation temperatures. This can be expressed as:

$$P_{tot} - P_w = \left(\frac{dP}{dT}\right)(T_e - T_{cc}) \quad (4)$$

where  $T_e$  corresponds to the saturation temperature in the evaporator grooves, and  $T_{cc}$  corresponds to the saturation temperature in the compensation chamber, and  $dP/dT$  is the slope of the saturation line at the given pressure and temperature of the compensation chamber [5]. The slope of the saturation line can be related to physical properties of the working fluid by using the Clausius-Clapeyron equation:

$$\frac{dP}{dT} = \frac{\lambda}{(T_{cc}\Delta v)} \quad (5)$$

where  $\Delta v$  is the difference in the vapour and liquid specific volumes and  $\lambda$  is the latent heat of vaporization of the working fluid.

## 2.2 LHP OPERATING CHARACTERISTICS

The operating characteristics of LHPs are dependent on various parameters which can be related to specifics of the LHP itself, or its application and environment.

### 2.2.1 Operating Temperature

The LHP operating temperature is primarily driven by the compensation chamber given that it is closely related to various parameters all around the LHP such as the evaporator heat load, condenser sink temperature, and the temperature surrounding the liquid return line. Figure 5 can be used to better demonstrate the complex relations that exist between LHP components.

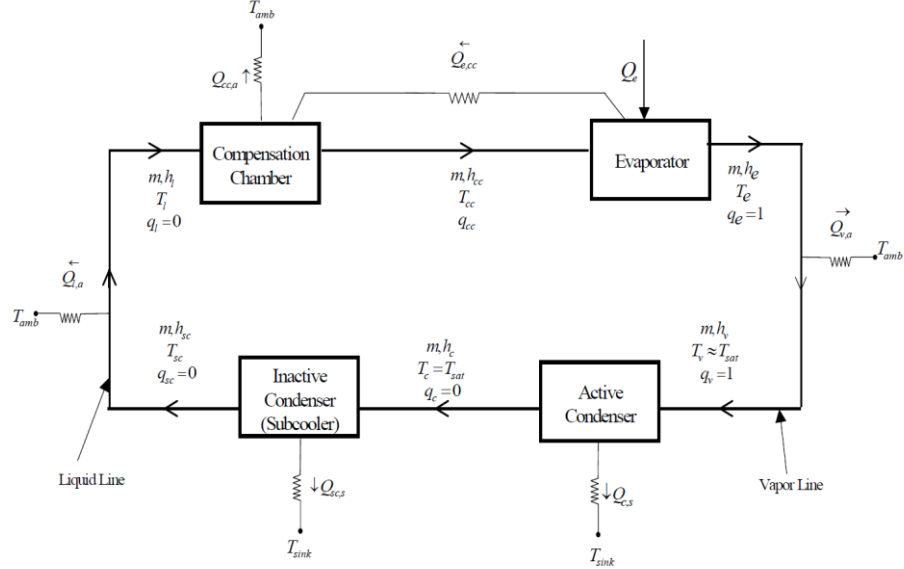


Figure 5: LHP Thermal Resistance Network [5]

The temperature of the compensation chamber is closely related with that of the evaporator given their connection through the primary and secondary wick. Heat applied to the evaporator ( $\dot{Q}_e$ ) is mainly transferred to the vaporization of the liquid; however, some heat leaks to the CC. The energy balance equation for the evaporator can thus be expressed as:

$$\dot{Q}_e = G_{e,cc} (T_e - T_{cc}) + \dot{m}\lambda \quad (6)$$

The first term on the right-hand side of Eq. 6 denotes the heat leak from the evaporator to the CC and is a function of the thermal conductance between these two components ( $G_{e,cc}$ ), and their respective temperatures. The second term represents the heat used for the vaporization of the working fluid which depends on the mass flow rate ( $\dot{m}$ ) and the fluid latent heat ( $\lambda$ ). The heat load

to the evaporator directly impacts the heat leak to the compensation chamber [5]. As the heat load increases, more vapour may present itself within the evaporator core and additional heat leak is caused by the evaporation and the condensation of bubbles between the evaporator and CC.

Assuming steady-state, heat exchange between the evaporator and compensation chamber must be balanced out by the subcooled liquid from the condenser [5]. Assuming the CC has negligible heat transfer with the environment, the energy balance equation for the CC may be written as:

$$G_{e,cc}(T_e - T_{cc}) = \dot{m}c_p(T_{cc} - T_{in}) \quad (7)$$

where  $T_{in}$  is the liquid temperature at the entrance of the compensation chamber and  $c_p$  is the liquid specific heat [5].

Liquid travelling from the condenser to the CC is affected by parasitic heat exchange with its surroundings. The change in temperature of the subcooled liquid from the condenser exit ( $T_{sc}$ ) to the CC inlet can be expressed as:

$$T_{in} - T_{sc} = \frac{\dot{Q}_{liq,amb}}{\dot{m}c_p} \quad (8)$$

where  $\dot{Q}_{liq,amb}$  is the heat exchange between the surroundings and the liquid. Finally, the subcooled liquid temperature is a function of the condenser sink temperature.

Eq. 6 to Eq. 8 relate all major parameters that contribute to the CC fluid temperature as had been previously mentioned (evaporator heat load, liquid line surrounding temperature, and condenser sink temperature). Since the mass flow rate is a function of the applied heat load, it is easy to notice that the heat load is arguably the parameter which affects the LHP operating temperature the most. Figure 6 shows the general trend of the LHP operating temperature as a function of the evaporator heat load.

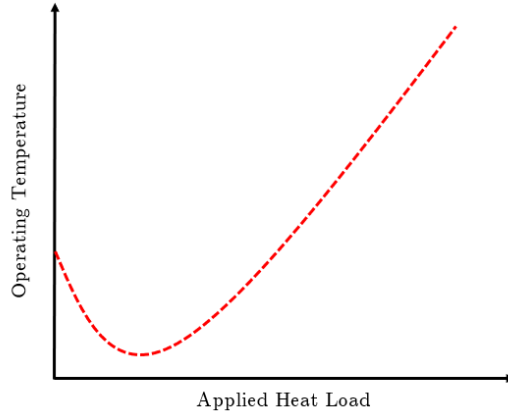


Figure 6: LHP Operating Temperature vs. Evaporator Heat Load (typical trend)

At low heat loads, the condenser is only partially utilized for vapour condensing and low mass flow rates are observed. This slow motion exposes the fluid in the liquid line to ambient temperature for longer periods of time, increasing heat gain from the environment and hence warm fluid returns to the CC. As the heat load is increased, the mass flow rate increases and less heat gain in the liquid line is observed. This leads to a decrease in fluid temperature entering the CC. This trend continues until the condenser is being fully utilized and the condenser can no longer dissipate larger amounts of energy. At this point, warmer fluid starts gradually arriving at the CC and an increase in operation temperature is observed as higher heat loads are experienced by the evaporator. Furthermore, an increase in the heat load causes an increase in the heat leak from the evaporator to the CC which in turn increases the CC temperature. It is important to also note that the decreasing temperature - because of increasing mass flow rate - would still be observed even if the liquid line was completely insulated. This occurs because the increase in fluid velocity causes an increase in pressure drop along the liquid line which also causes a decrease in temperature.

Kaya and Ku [6] noticed that when the sink temperature was located above the ambient temperature, the LHPs saturation temperature tended to increase with increasing power to reject the heat load. By increasing the saturation temperature, the difference between saturation temperature and sink temperature increased to allow for larger heat transfer rates. This caused the LHP to operate as a constant conductance device; the saturation temperature varied almost linearly across all the entire range of heat loads.

On the other hand, Kaya and Ku [6] also concluded that when the sink temperature is below the ambient temperature, subcooled liquid from the condenser decreases the saturation temperature. It was noted that at low heat loads, greater heat is required to raise the temperature of the subcooled liquid to saturation temperature. As the heat load increased, the increase in mass flow rate causes even further fluid subcooling. In addition, Ku [5] noted that variations in the condenser sink temperature have a more prominent effect on the LHP operating temperature when at high heat loads. To achieve minimum operating temperatures, a high power and low sink temperature configuration is required.

Larger temperature differences cause larger heat transfer. Unlike variations in the sink temperature, the effects of the surrounding temperature on the LHP become more pronounced at low powers since the temperature difference is greater (assuming surrounding temperature is greater than sink temperature) [5]. Moreover, work by Kaya and Ku [6] also demonstrated that heat exchange between the CC and the ambient is dominant at low powers to match the heat leak from the evaporator to the CC. In a scenario when the surrounding temperature is less than the sink temperature, heat is transferred away from the liquid line to the surroundings. In this case, the liquid line acts as a subcooler section and the operating temperature would continue to decrease through the entire power range.

### **2.2.2 Start-up**

Due to the presence of a secondary wick, the evaporator is replenished with liquid and start-up can be achieved by just applying power to the evaporator. Nevertheless, the start-up process is complex and heavily depends on the compensation chamber and evaporator construction, initial conditions inside the evaporator, and the operation immediately prior to start up [5].

The three major factors that play a role in the behaviour of LHPs during start-up are the evaporator grooves, the evaporator core, and the evaporator heat load. Firstly, if the evaporator grooves are filled with liquid, it is necessary to superheat the working fluid to initiate nucleate boiling. On the other hand, if the vapour grooves already contain vapour, evaporation will occur once power is applied [5, 7]. Secondly, if the evaporator core is filled with liquid, then there

is minimum heat transfer from the evaporator to the CC; nonetheless, if vapour is present in the core, heat leak through the primary wick to the CC is increased as discussed in Section 2.3.1. Last of the three is the evaporator heat load which affects start-up through interaction with the previous two factors.

Four situations arise from the different combinations of these three factors and are shown in Figure 7.

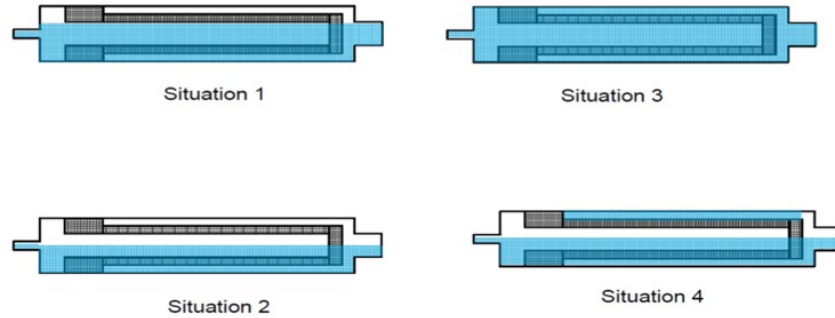


*Figure 7: Start-up Scenarios [5]*

In situation 1, vapour is found within the vapour grooves and the evaporator core is filled with liquid. The liquid starts evaporating immediately once the heat load is applied and small heat leak is observed from the evaporator to the CC. This situation is the more desirable case.

Situation 2 corresponds to a case when vapour is within both vapour grooves and the evaporator core. Start-up occurs in a similar fashion to situation 1, but larger amounts of heat leak from the evaporator to the compensation chamber is expected.

In situation 3, the vapour grooves and the evaporator core are both filled with liquid. As a heat load is applied, temperature within the CC remains the same while the temperature in the evaporator increases (little heat leak). Start-up is delayed since the fluid must be superheated before nucleation can be initiated, and vapour may be generated inside the evaporator core or may even penetrate the evaporator wick.

Situation 4 occurs when the evaporator grooves are filled with liquid and the evaporator core contains vapour. Superheat is required to initial nucleation but

temperature rise in the compensation chamber is also observed. Unless temperature of the liquid in the evaporator grooves increases at a faster rate than in the compensation chamber, the loop will not start [5].

In addition to the distribution of fluid within the evaporator grooves and evaporator core, the presence of non-condensable gas (NCG) has shown to both degrade the performance of LHPs and affect start-up [7]. Although NCG can be found in almost every part of the system loop, it tends to accumulate in the CC which causes a modification of the system pressure. With a higher pressure within the CC, the evaporator temperature during start-up must first increase to the saturation temperature that corresponds to the higher pressure (see Eq. 4) and then attain superheat to initiate nucleate boiling. This results in a direct increase of the temperature overshoot during start-up, and a delayed onset of nucleate boiling in the vapour grooves, causing an increased start time accordingly [7].

### **2.2.3 Temperature Hysteresis**

“Hysteresis” is used to describe cases in which the output depends on current and past inputs, resulting in different outputs for the same test conditions. In LHPs, depending on whether power applied to the evaporator increased or decreased, different responses are observed regardless of having the same testing conditions [5].

When the applied heat load on the evaporator decreases, liquid is injected from the compensation chamber through the evaporator core to the condenser to reduce the area for condensation. With a large decrease in heat load, the pressure head required to expel liquid may exceed the capillary limit of the secondary wick and vapour may accumulate in the evaporator core [5]. This causes an increase in heat leak from the evaporator to the CC. LHPs operating at high powers are not susceptible to hysteresis since large mass flow rates collapse vapour bubbles inside the evaporator core.

### **2.2.4 Orientation**

The presence of vapour in the evaporator core has a strong effect on heat leak from the evaporator to the CC. Simultaneously, the amount of vapour in

the evaporator core is strongly correlated to elevation and tilt of the LHP which translates to large effects on the LHP operating temperature. Tests done by Ku [5] have shown that at low heat loads, the LHP operating temperature increases when the evaporator is located above the condenser. As gravity head increases, the difference in saturation temperature must also increase as per Eq. 4. The increase in pressure drop can only be satisfied by increasing the evaporator vapour temperature which in turn causes an increase in heat leak from the evaporator to the CC. As temperatures within the CC increase, the evaporator vapour temperature also increases which creates an overall increase in operating temperature.

### 2.2.5 Temperature Oscillations

Temperature pulsations occur in two-phase heat transfer devices under stable conditions of heat supply and removal. These pulsations are also accompanied by oscillations of the pressures and volumes of phases of the working fluid within the LHP. Temperature oscillations are characterized based on their frequency and amplitude. Historically, it has been observed that oscillations in operation temperature in LHP rise with decrease in volume of the working fluid and that the character of these fluctuations depend on the heat load and condenser cooling conditions [8]. Depending on their magnitude, these oscillations may even affect the temperature of all LHP parts and thus the LHP operating temperature [8].

The first type of oscillations are those with low amplitude (less than 1 °C) and high frequency fluctuations of the evaporating liquid front in the wick. They are created by changes in the amount of working fluid available in the LHP, its orientation and the condenser sink temperature [8]. These types of fluctuations can be observed in low and high heat-loads and do not affect LHP heat transfer capabilities.

The second mode of oscillations are characteristic of low amplitude and medium frequency (period of several minutes) fluctuations. These oscillations are observed at low heat loads and have synchronous temperature fluctuations in both liquid and vapour lines [8]. The amplitude of these fluctuations are generally larger in the liquid line and have been observed to arise when the vapour-to-liquid interface in the condenser is situated close to one of its ends.

Finally, the last mode of temperature oscillations corresponds to those with high amplitude (reaching tens of degrees) and low frequency (tens of minutes) fluctuations. These pulsations may occur in all parts of the LHP including the compensation chamber, and can lead to crisis in the LHP operation. These are observed when the amount of working fluid in the LHP is extremely low, when operating in an unfavourable orientation, and when there is intensive cooling at the condenser [8]. Additionally, they are observed at both low and high heat-loads. Moreover, these types of oscillations are observed with the presence of a large heat source with low capacity (low thermal mass) and when the sink temperature is below ambient temperature.

Oscillations of the bulk of the vapour phase in the compensation chamber are responsible for pulsations observed in LHP. As the heat load and sink temperature increase, the amplitude and period of these oscillations decrease. In general, temperature oscillations are not fatal for the operation of LHP, however they may have negative consequences on equipment whose temperature must be precisely controlled. On the other hand, oscillations of the third type may cause crisis in the LHP operation, especially at sufficiently high heat-loads [8].

In [8], experiments were conducted on a miniature LHP in order to investigate temperature oscillations in a LHP under various conditions. It was observed that temperature pulsations were initiated when the amount of working fluid in the LHP was lowered below the optimum amount. As the amount of working fluid was further decreased, these pulsations increased in both amplitude and period. Further testing also revealed that when the LHP was placed in unfavourable orientations (i.e. evaporator above condenser or CC above evaporator), considerable operating temperature fluctuations are initiated. This occurrence is attributed to the shortage of liquid in the compensation chamber as a result of gravitational effects which redistributes the working fluid between the CC and condenser. Lastly, the authors of [8] concluded that a more intensive cooling of the condenser can stimulate the initiation of intense operating temperature fluctuations. These results are similar to that of orientation since a lower condenser sink temperature draws more fluid to the condenser away from the CC. If the cooling temperature is below the ambient temperature, the amount of fluid in the CC decreases which

may cause the overshoot of vapour or insufficiently cooled condensate into the compensation chamber.

## **2.3 LHP TEMPERATURE CONTROL TECHNIQUES**

Various components and spacecraft payloads have very narrow temperature ranges which have traditionally been met using active systems; nevertheless, passive control techniques are generally preferred given their reduced complexity, lower cost, and higher reliability. LHPs have proven to be not only efficient heat removal devices, but also useful in applications requiring accurate temperature control.

### **2.3.1 Temperature Control Methods**

While a normal LHP (no temperature control technique implemented) is capable of removing and re-distributing heat away from an equipment of interest, it is not capable of ensuring temperature is kept above a desired threshold. In other words, LHPs by themselves can cool equipment, however the degree of cooling is not regulated by the LHP, but instead depends on external factors such as sink temperature. Various temperature control techniques exist to ensure equipment attached to the evaporator is kept within a desired range.

#### **2.3.1.1 External Heating**

If the LHP saturation temperature (which is a function of input power and sink conditions) is below a desired set point, the LHP operating temperature can be maintained by externally heating the CC and thus maintaining a constant CC temperature as illustrated in Figure 8. If the desired temperature cannot be maintained, additional power can be applied to the external heating source which would allow for control at this higher saturation temperature.

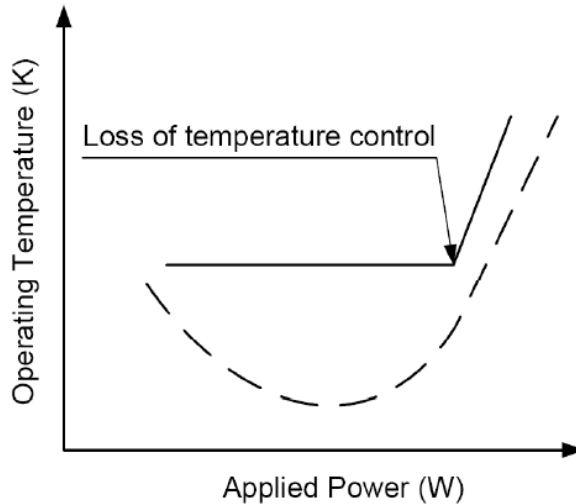


Figure 8: LHP Saturation Temperature vs. Input Power. The dashed line indicates no external heating at the CC. The solid line represents external heating applied at the CC [9]

There are multiple drawbacks to applying external heating to the CC. First, a large control power (to the order of 20% of input power) may be required. In addition, the location of the control sensors greatly influences this technique's accuracy and sensitivity. Undesirable LHP shutdowns were observed on the ICESat mission due to the use of an on/off controller for the CC heater [9]. Large control heat power was required during start-up (due to the rapid arrival of subcooled liquid) causing heating of the CC to occur faster than the evaporator. Lastly, due to the large thermal mass of the CC, the response time of the CC set point is large (creating lag) when subjected to transients such as sink temperature change [9].

### 2.3.1.2 Thermal Coupling of Transportation Lines

This technique involves coupling the vapour and liquid lines to raise the temperature of the returning subcooled liquid. In doing so, the required external heater control power at the CC is reduced. Coupling lines are implemented such that the heater control power is minimized without vastly affecting the LHP thermal conductance [9]. This is done through the optimization of the number of coupling lines. The operation temperature rises as more coupling lines are added because of the reduced subcooling. Thus, less power is required to bring the CC temperature to the required set point.

### 2.3.2 Pressure Regulating Valves

Previously discussed temperature control techniques require the use of an external heat source. Pressure regulating valves (PRVs) on the other hand make use of vapour in the vapour line to increase the CC temperature and may hence operate without the need of additional power. PRVs are commonly used in the precise temperature control of satellite equipment to prevent overcooling and have proven functional for temperature control requirements of up to  $\pm 2$  K [9]. Two main types of PRVs are used for temperature control in LHPs: three-way-valves and two-way-valves.

Three-way valves operate by re-distributing vapour flow in the LHP and it does so by connecting the condenser, vapour line and compensation chamber. Vapour from the vapour line is by-passed to the CC to heat up and increase the LHP operating temperature above the minimum threshold. The main drawback with the use of a three-way PRV in LHPs is the possibility of heat source overheating. This can be caused by the undesired leakage of vapour into the by-pass line as the device operates as a conventional LHP. Two-way PRVs overcome this problem by eliminating the need of a bypass line [9]. This lack of a bypass line results in a completely different law of valve regulation: while the three-way valve adjusts the CC temperature, the two-way valve adjusts the LHP pressure drop which results in the control of the operation temperature.

#### 2.3.2.1 Three-way PRVs

A schematic of a three-way PRV is shown in Figure 10. The cavity around the bellows is filled with an inertial gas to a pre-determined pressure which determines the set point temperature (temperature at which thermal regulation from the PRV must initiate).

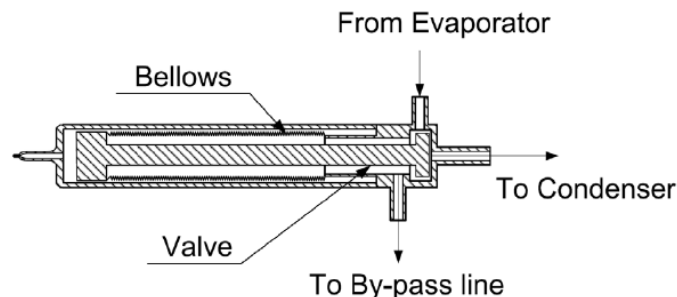


Figure 9: Three-Way Pressure Regulating Valve Schematic [9]

The valve position is dictated by the back pressure caused by the inert gas (typically argon), the working fluid pressure, and the bellows force (which behaves similarly to a spring) [10]. The back pressure is set such that flow is completely diverted to the bypass line if the working fluid pressure (and hence temperature) is below a desired threshold. If the working fluid pressure is above this set point, the valve starts opening to allow vapour flow towards the condenser. As the working fluid pressure increases, the valve continues to open to allow for more cooling by the condenser, until the pressure reaches its regulation point. Here, the valve is fully open, and the system operates like a normal LHP (maximizing cooling). By controlling the amount of cooling (vapour moving to the condenser) and heating of the CC (bypass vapour moving towards the CC), the three-way PRV regulates the LHP operating temperature between a predetermined range. Figure 10 shows the position of the valve with respect to the working fluid pressure in order to better illustrate its operation.

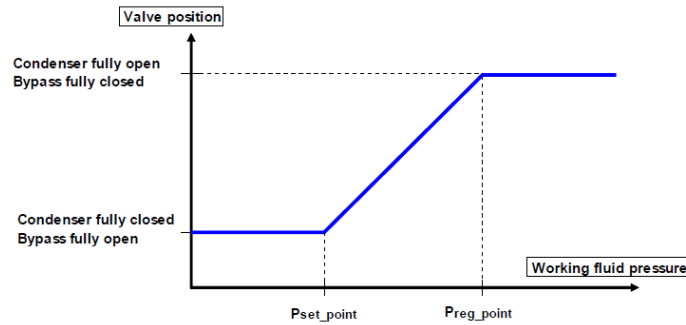


Figure 10: PRV Valve Position vs. Working Fluid Pressure [10]

For the three-way PRV to operate, the evaporator temperature cannot be below the set point (for a given power and regardless of the sink temperature) as flow circulation would only be established in the bypass line [10]. In this state, no power removal would be performed since the evaporator and equipment temperature would be equal. The PRV set point can thus be defined as the minimum possible evaporator temperature when the LHP is in operation.

To properly define the control law for this type of PRV, it is important to identify the relation between how much vapour is allowed to flow towards the condenser as a function of the working fluid pressure when above the desired threshold/ set point. This can be done by examining the heat which must be removed by the condenser to maintain the appropriate operating temperature

[10]. Additional parasitic heat exchange at the valve must be considered in addition to the potentially excessive subcooling that is required if too much vapour is being bypassed towards the CC. Valve operating conditions usually correspond to small amounts of bypass vapour and the condenser line being almost fully open [10].

### 2.3.2.2 Two-way PRVs

A schematic of a two-way PRV is shown in Figure 11. Similarly to the three-way PRV, the cavity around the bellows is filled with an inertial gas to a pre-determined pressure, but its operation is strictly based on limiting the amount of vapour travelling towards the condenser.

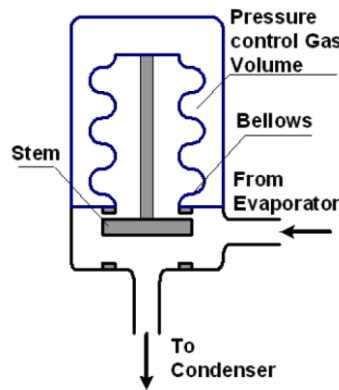


Figure 11: Two-Way Pressure Regulating Valve Schematic [10]

More specifically, the two-way PRV in a LHP operates through the degradation of conductance of the LHP. Conductance is degraded by the addition of an external pressure drop created by the valve. If the induced heat load is too large and/or the sink temperature too low, the LHP performance is degraded, which causes a decrease to the amount of heat transfer and an increase to the operational temperature. By decreasing the amount heat transfer between the LHP and the equipment, overcooling can be controlled.

The additional pressure drop is caused by hydraulic resistance that is introduced in the vapour line through the changing of the cross section of the line (at the valve location). This allows the temperature of the evaporator to be controlled and maintained almost constant and independent of the condenser temperature. Figure 12 can be used to further explain the effects of the added pressure drop along the vapour line.

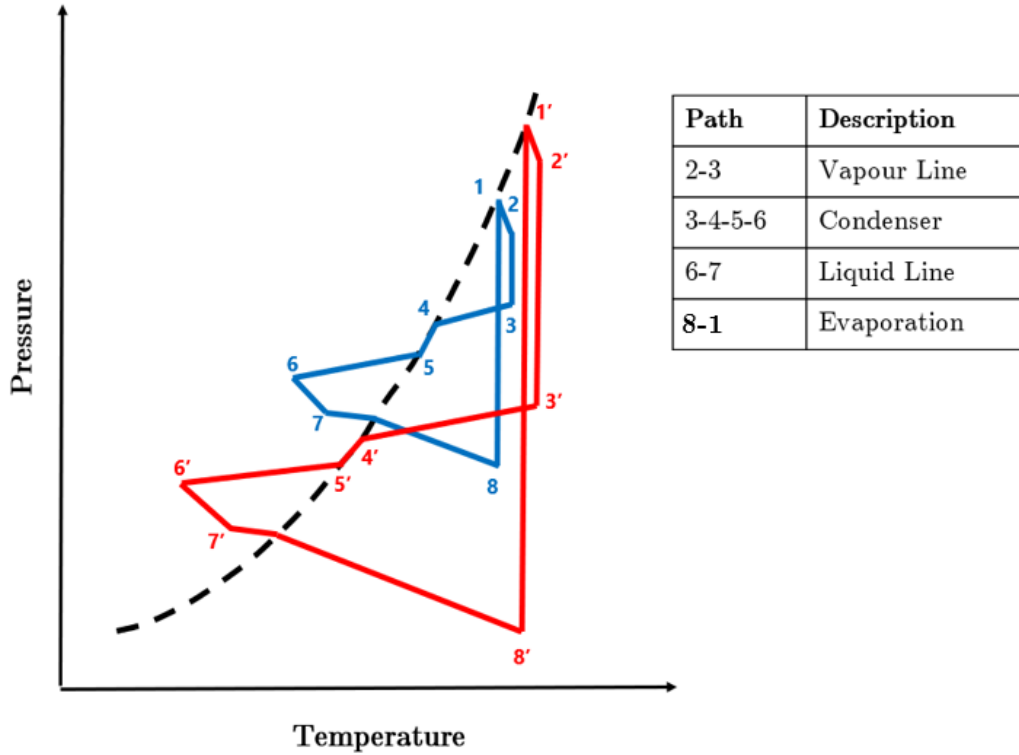


Figure 12: Pressure-Temperature diagram of LHP under two scenarios: without PRV (blue) and with PRV (red)

Points numbered in Figure 12 correspond to those mentioned in Section 2.1.2. As the valve closes, an increase in heat leak is observed which causes an increase in the evaporator temperature, shown by the graph shifting from 1 to 1'. As is clear from the diagram, increasing the pressure drop within the vapour line (point 2 to 3) causes an increase in the temperature difference between the evaporator and condenser [10]. This is further backed up by Eq. 4. By increasing the temperature difference between these two components, the amount of heat leak across the wick into the compensation chamber increases. As previously explained, this causes an increase in the LHP operation temperature which leads to a performance degradation in the LHP: less heat is extracted from the equipment and overcooling is controlled. Similarly to the three-way PRV, once the valve is open, the system operates as a normal LHP under constant conductance at its maximum heat rejection mode.

## CHAPTER 3 TEST SETUP

The following chapter presents the experimental setup and equipment used in the testing of a LHP with a two-way PRV, and the uncertainty analysis done. Testing was performed to characterize the LHP's behaviour and operational characteristics and to gain better understanding of the temperature regulation of LHPs using two-way PRVs. All experimental work was performed in the Heat Pipe Laboratory in room 2233 in the Mackenzie Engineering building at Carleton University.

### 3.1 APPARATUS

The tests are performed on a flight-proven LHP with a two-way PRV on the vapour line, designed and manufactured by IberEspacio in collaboration with Carleton University [11]. Given that the LHP is designed for operation in space, modifications had to be made for its suitable testing in ground level conditions.

The overall apparatus layout is shown in Figure 13. The LHP was placed on a levelling steel table using the supporting structure provided by IberEspacio. A cartridge heater was attached to the bottom of the LHP evaporator and attached to a power regulator. A custom heat exchanger was attached to the LHP condenser plate and fluid is circulated by the chiller to and from the heat exchanger to act as the sink. Ambient temperature and pressure was not regulated throughout the experiments; hence, the entire system was insulated using polyethylene foam rubber insulation with an approximate R-value of  $4 \text{ K m}^2/\text{W}$  to reduce the effect of temperature variations on the results.



Figure 13: Complete Experimental Setup

### 3.1.1 Loop Heat Pipe

Figure 14 shows the LHP as provided by IberEspacio. The system is supported by a frame made of 4 cm x 4 cm slotted aluminium and plastic supports along the evaporator and transportation lines.

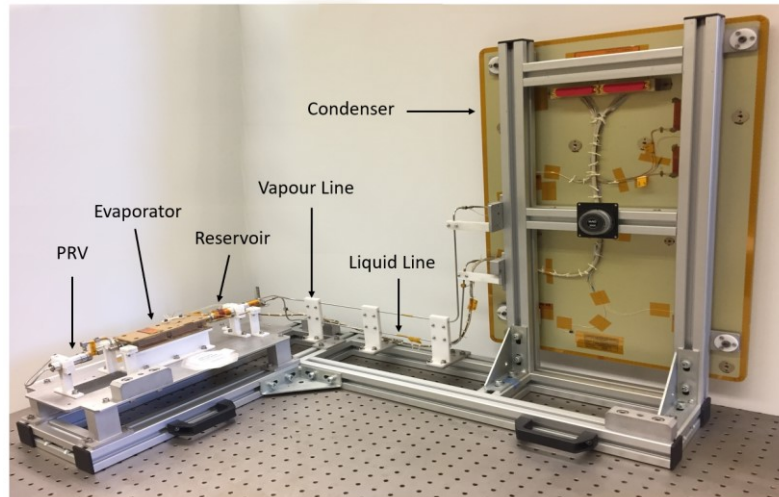


Figure 14: IberEspacio Loop Heat Pipe System

Transportation lines and evaporator/ compensation chamber casings are made of AISI 316L, and the condenser line is routed inside of a panel made of aluminium honeycomb with aluminium skins. The evaporator is encased by a saddle made of Al 6082 T6, shown in the following figure. Table 1 shows all relevant LHP physical dimensions and specifications.

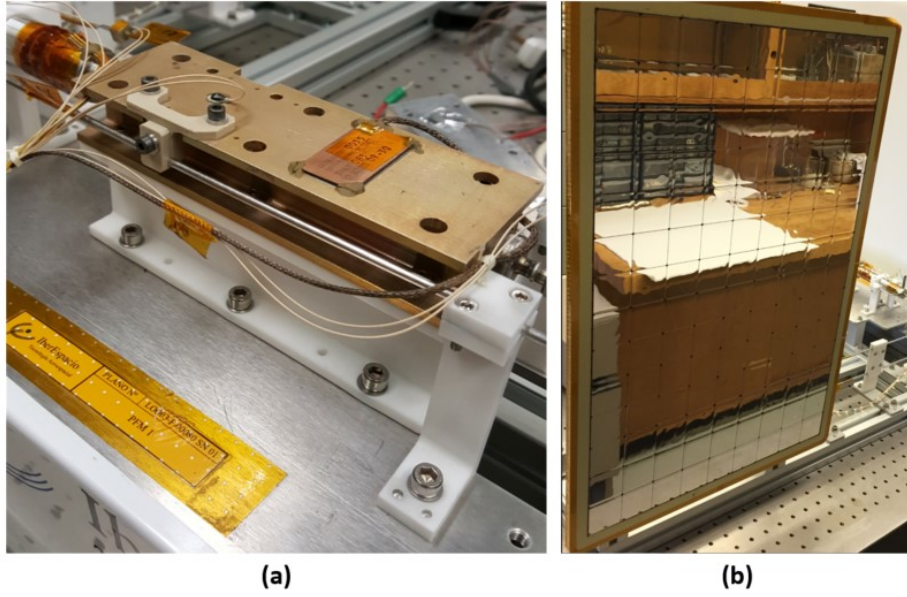


Figure 15: (a) Evaporator Saddle, (b) Condenser Panel

Table 1: Loop Heat Pipe Physical Properties

Component	Property	Value
Working Fluid	Type	Ammonia
	Amount	27.2 g
Evaporator Casing	Cross Section Shape	Circular
	Inner Diameter	14 mm
	Outer Diameter	15.4 mm
	Length	174.5 mm
Primary Wick	Material	Nickel
	Outer Diameter	14 mm
	Length	160 mm
	Porosity	60 %
Vapour Line	Wick Effective Diameter	1.4 micron
	Inner Diameter	2 mm
	Outer Diameter	3 mm
Condenser Line	Length	1504 mm
	Inner Diameter	2.5 mm
	Outer Diameter	3 mm
Liquid Line	Length	1187 mm
	Inner Diameter	2 mm
	Outer Diameter	3 mm
	Length	901 mm

Compensation Chamber	Cross Section Shape	Circular
	Inner Diameter	19.5 mm
	Outer Diameter	21.5 mm
	Length	127 mm
PRV	Control Fluid	Argon
	Set Point	29 – 31 deg C
	Type	Two-way
Condenser Panel	Cross Section Shape	Rectangle
	Cross Section Size	(406 x 610) mm <sup>2</sup>
	Thickness	10.8 mm

### 3.1.2 Heating System

To provide power to the LHP, a cartridge heater made of Al 6082 T6 was attached on the underneath of the evaporator saddle as shown in Figure 16. To ensure better heat transfer, thermal conductive paste was applied to the cartridge before installation. Six custom-made plastic supports were introduced to provide structural support to the entire evaporator.

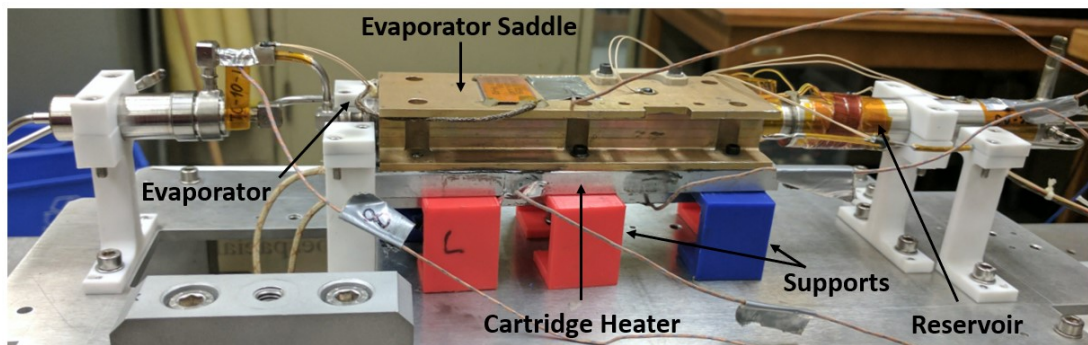


*Figure 16: Evaporator with Cartridge Heater Installed*

A power regulator (Powerstat® variable autotransformer, 3PN116B) was used to control the power applied to the cartridge heater. Two digital multimeters (Mastech® M9502) are used to measure AC voltage with an uncertainty of 0.8 % of reading, and AC current with an uncertainty of 3.0 % of reading.

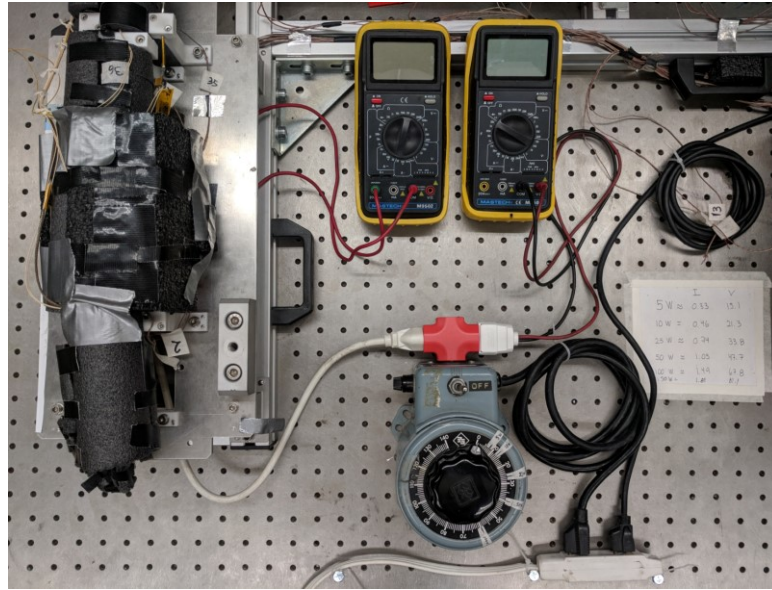


Figure 17: Heating System Equipment with Insulated Evaporator

### 3.1.3 Cooling System

A custom heat exchanger was designed and built to be attached to the LHP condenser panel and act as the sink. Figure 18 shows the CAD model of the heat exchanger as well as the underlying piping and input and output ports used to circulate the cold fluid through.

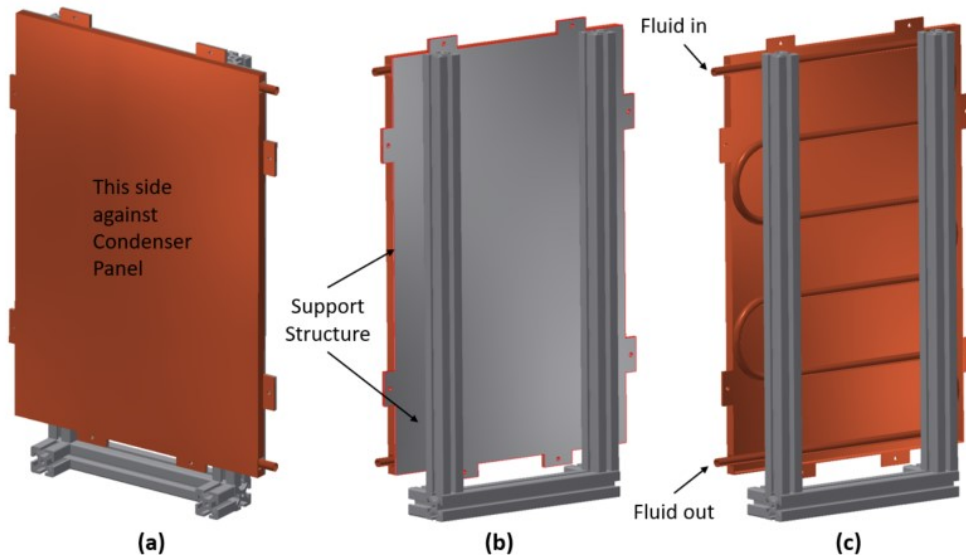


Figure 18: Heat Exchanger CAD Model. (a) front view - full assembly, (b) back view - full assembly, (c) back view - back support panel removed

Fluid flows through the heat exchanger through 1/2-inch outer diameter copper tubing that is attached to a copper plate using thermal conductive epoxy (E30-500 by Alfa International Corporation) with a thermal conductivity of 3.6 W/m K. A thermal gap filler (Tpli™ 200 by Laird Technologies) with a thermal conductivity of 6 W/m K was used on the condenser facing side of the heat exchanger to help improve thermal conduction between the heat exchanger and the condenser panel. The heat exchanger is fastened to the condenser panel by fastening the LHP support frame to the heat exchanger support structure, and c-clamps are used to provide contact pressure between both panels.

A chiller (Kodiak® Recirculating Chiller, RC011) was connected to the heat exchanger and used to circulate a mixture of 70 % Ethylene Glycol and 30 % water at 5 ° C with an uncertainty of  $\pm 0.1$  °C. The mean flow rate of the coolant was 10 LPM as measured using a flow meter with an uncertainty of  $\pm 0.2$  LPM across the full-scale range.

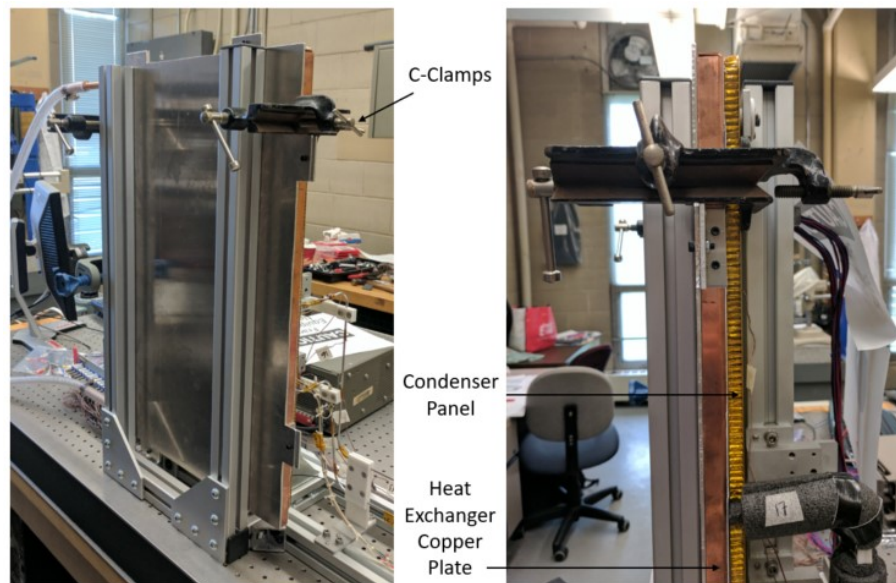


Figure 19: Heat Exchanger Assembly

### 3.1.4 Data Acquisition System

Data was collected using a Keithley Model 2700 data acquisition system with 6 1/2-digit (22 bit) resolution. The Keithley used an internally regulated reference in all temperature acquisition [12]. The data was passed to a Pentium

4, 3.2 GHz PC where it was recorded to the hard drive. The analogue to digital conversion error is estimated to be  $\pm 0.8\%$  [13] [14].

### 3.2 INSTRUMENTATION

Thirty-nine copper/constantan (type T) thermocouples were positioned along the heat pipe at various positions as shown in Figure 20. Three thermocouples ( $TC_{113}$ ,  $TC_{114}$ , and  $TC_{115}$ ) were left near the test setup to measure ambient temperature and one ( $TC_{138}$ ) was placed on the inside of the chiller reservoir tank. Thirteen thermistors that had been previously installed by IberEspacio were left on for comparison purposes with thermocouple results.

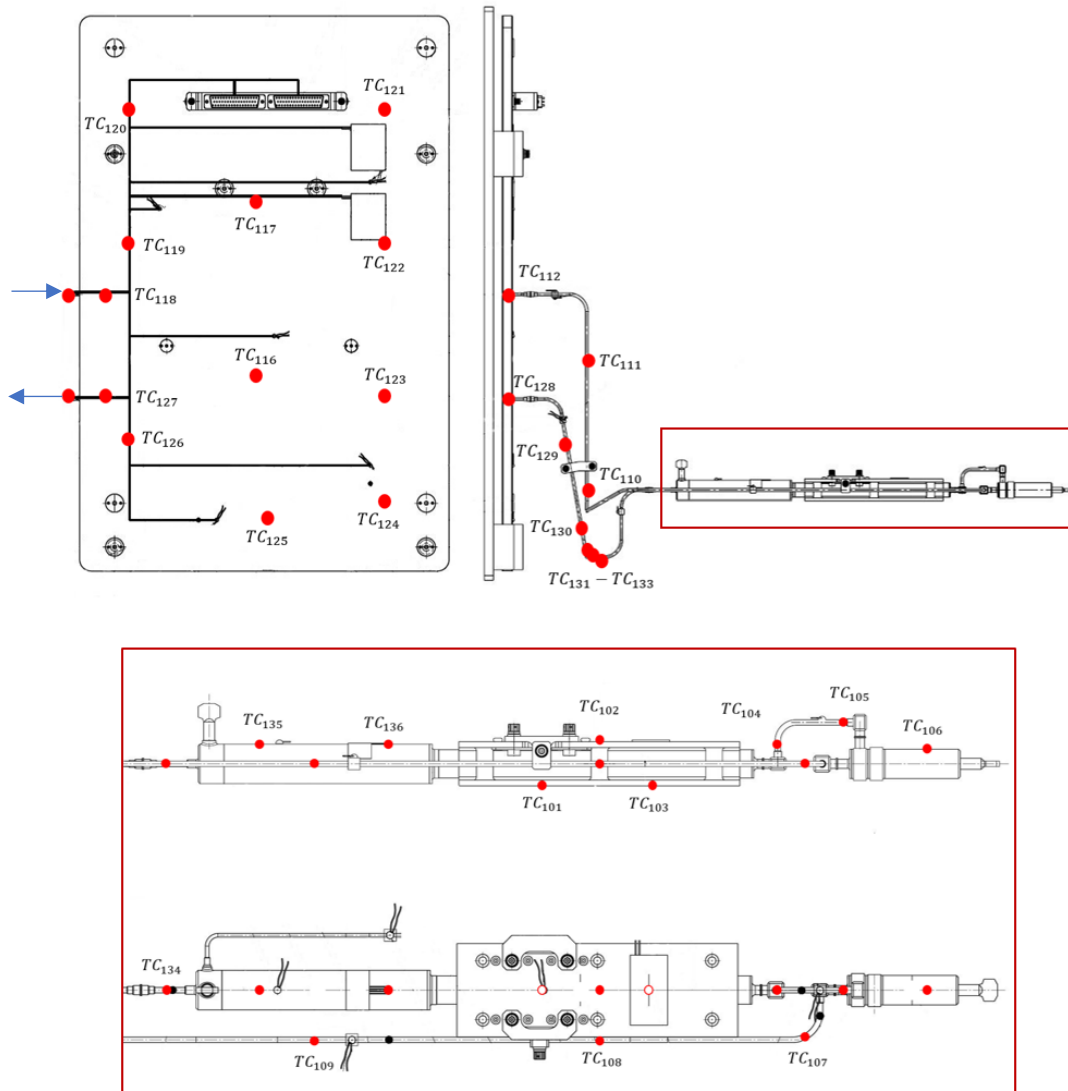


Figure 20: LHP Thermocouple Placement and Schematic

The thermocouples on the condenser panel were located in such a way that they would follow the path of the condenser tubing inside the panel. Images of a 3D model of the condenser, provided by IberEspacio, were used to get a general sense of pipe routing, and a thermal imaging camera was used to identify the position more accurately. Sample images are shown in Figure 21.

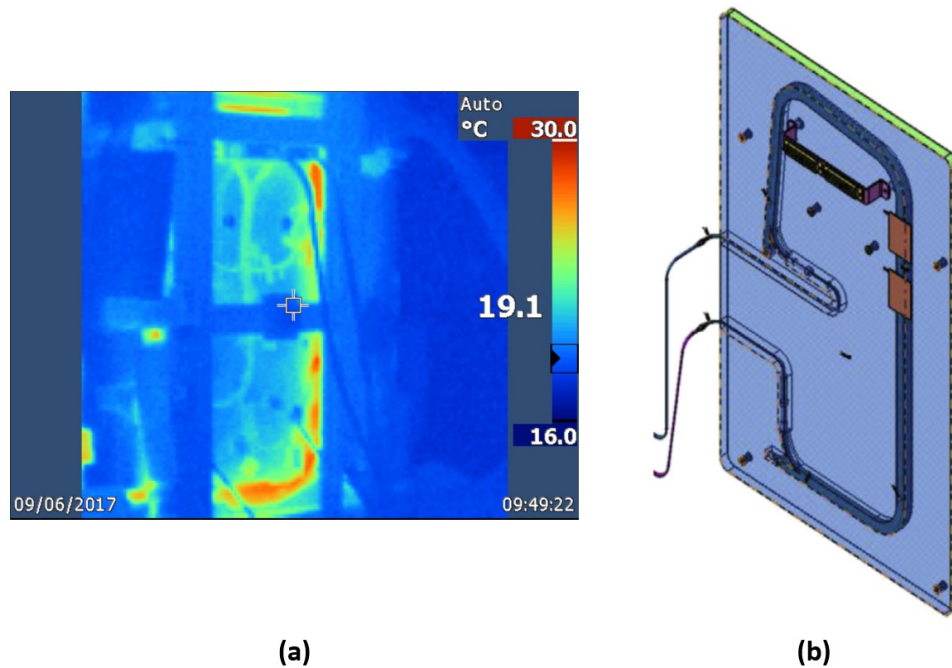


Figure 21: Condenser Pipe route inside Condenser Panel (a) Thermal Image, (b) CAD Model

### 3.3 UNCERTAINTY ANALYSIS

The following analysis was done to obtain an estimate of the uncertainty likely to exist in experimental results, considering the propagation of errors through all measurements. This initial analysis was useful to determine if the available equipment and the measurement techniques were appropriate for all tests.

#### 3.3.1 Input Power Uncertainty

To calculate the uncertainty of the input power, a general uncertainty analysis using the Taylor Series Method found in [15] was used. By implementing this method, it is possible to determine how uncertainties from

the measured voltage ( $V$ ) and current ( $I$ ) propagate into the calculated power ( $P$ ), given that

$$P = VI \quad (9)$$

The general uncertainty equation presented in [15] can be modified for this specific case and expressed as

$$U_P^2 = \left(\frac{\partial P}{\partial V}\right)^2 U_V^2 + \left(\frac{\partial P}{\partial I}\right)^2 U_I^2 \quad (10)$$

where  $U_P$ ,  $U_V$ , and  $U_I$  correspond to the uncertainties in the resultant power and measured voltage and current, respectively.

Dividing both sides of the equation above by  $P^2$  and multiplying the first right hand term by  $(V/V)^2$  and the second by  $(I/I)^2$  yields

$$\frac{U_P^2}{P^2} = \left(\frac{V}{P} \frac{\partial P}{\partial V}\right)^2 \left(\frac{U_V}{V}\right)^2 + \left(\frac{I}{P} \frac{\partial P}{\partial I}\right)^2 \left(\frac{U_I}{I}\right)^2 \quad (11)$$

In Eq. 11, terms of the form  $U_X/X$  are referred to as *relative uncertainty*, and the factors in parentheses that multiply the relative uncertainties of the variables are known as *uncertainty magnification factors* (UMFs). Calculating these UMFs result in

$$UMF_V = \frac{V}{P} \frac{\partial P}{\partial V} = \frac{V}{VI} \frac{\partial(VI)}{\partial V} = \frac{VI}{VI} = 1 \quad (12)$$

$$UMF_I = \frac{I}{P} \frac{\partial P}{\partial I} = \frac{I}{VI} \frac{\partial(VI)}{\partial I} = \frac{VI}{VI} = 1 \quad (13)$$

A value of 1 for both UMFs indicate that the influence of the uncertainty in both variables is neither magnified nor diminished as it propagates through the data reduction equation into the result.

Finally, taking the square root of both sides of Eq. 11 and replacing the corresponding UMF values, the relative uncertainty in terms of fraction of applied power can be express as the following.

$$\frac{U_P}{P} = \sqrt{\left(\frac{U_V}{V}\right)^2 + \left(\frac{U_I}{I}\right)^2} \quad (14)$$

The above equation was evaluated over the range of input powers expected throughout the LHP testing and using the measurement uncertainties of the equipment available. The results, presented below in Figure 22, indicate a significant relative power uncertainty at low powers which quickly decreases as the applied power increases.

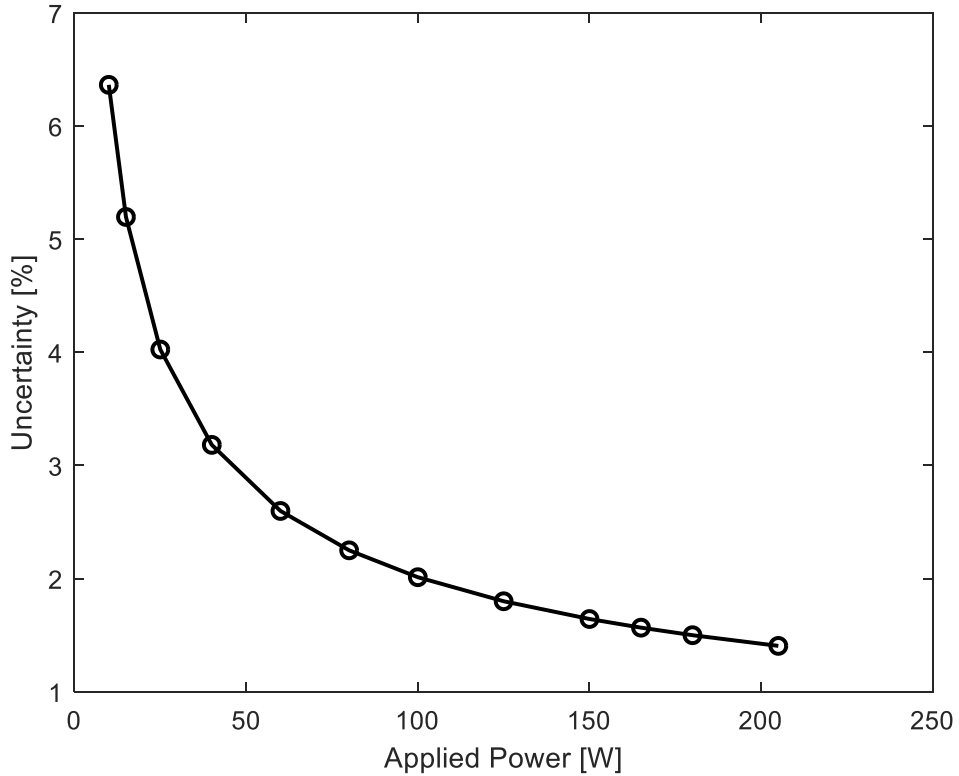


*Figure 22: Input Power Percent Uncertainty*

While low power uncertainties are more significant, the range of LHP operation in all tests is above 10 W which has an absolute uncertainty of 0.63 W. This degree of uncertainty is deemed acceptable for LHP characterization since it is not large enough to distort the data trends observed through testing at powers ranging from 10 W to over 180 W. Nevertheless, these errors must

be taken into consideration when determining the correlation between experimental results and the developed mathematical model and must be taken into consideration when determining correction factors.

### 3.3.2 Thermocouple Uncertainty and Variation

Given that temperatures measured throughout the tests do not exceed 50 °C, the T type thermocouples used are considered to have an uncertainty of  $\pm 0.5$  °C [14]. Nevertheless, to get a better understanding of the variation of thermocouple measurement data on this specific test setup, the instability of readings was determined via experimentation. Temperature data was collected every three seconds over a one-day period at ambient conditions without any applied power. Data from thermocouple  $T_{117}$  was then divided into one-minute segments and the sample standard deviation ( $s$ ) was calculated for each of these segments using the following formula:

$$s = \sqrt{\frac{1}{N-1} \sum_{i=1}^N (x_i - \bar{x})^2} \quad (15)$$

where  $N$  is the number of temperature readings in the interval,  $x_i$  is the temperature value of each reading, and  $\bar{x}$  is the mean of the temperature readings in the interval.

By reducing data into one-minute segments, random variations due to fluctuations in ambient temperature are isolated. As such, ambient temperature is assumed to remain constant over each time segment. Furthermore,  $T_{117}$  was chosen given that this thermocouple is in a well-insulated location on the test setup so as to further minimize the effect of ambient temperature changes on the data.

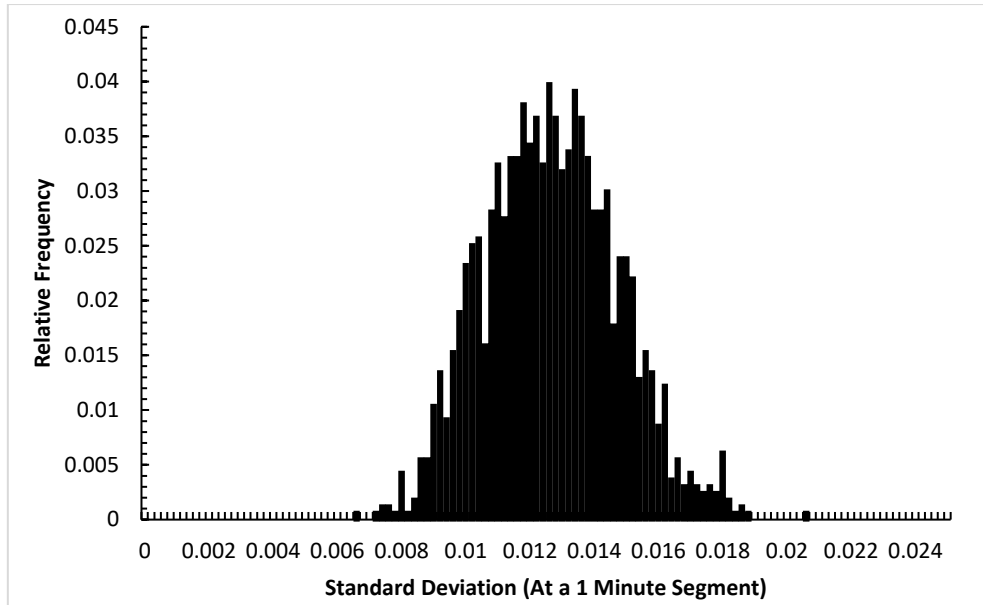


Figure 23: Thermocouple Standard Deviation

Figure 23 shows the relative frequency of standard deviation in thermocouple data for one-minute segments. Because standard deviation is a measure of dispersion of a set of data values, it gives a good insight into the amount of variation that should be expected from thermocouple measurements. The maximum standard deviation in the thermocouple data was found to be 0.02 °C.

### 3.3.3 Chiller Temperature Variation

Temperature data from the condenser plate was collected for 5 hours with no applied power and with the chiller running at its lowest temperature (5 °C). Similarly to above, the data was reduced into one-minute blocks and the standard deviation for each block was determined and plotted in the figure below. In comparison to the thermocouple measurement standard deviation, the spread of standard deviation for the chiller temperature is smaller than those for the thermocouples. This indicates that the chiller can hold a constant temperature at the condenser plate sufficiently such that the fluctuations due to random precision error of the thermocouples are more prominent and noticeable. The maximum standard deviation from the condenser plate was 0.019 °C.

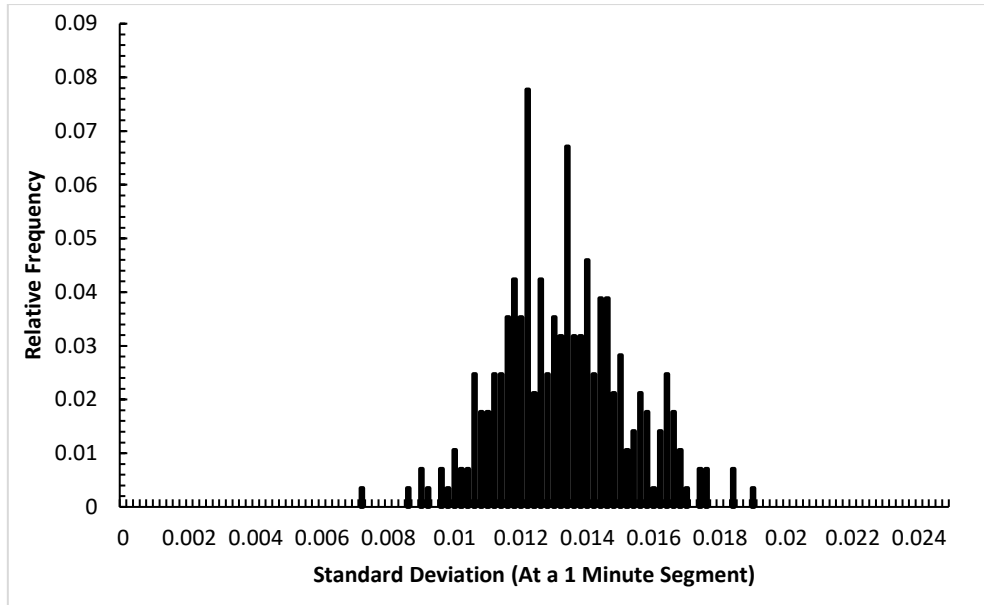


Figure 24: Chiller vs. Thermocouple Standard Deviation

### 3.3.4 Ambient Temperature Variation

The relative frequency of ambient temperature data collected throughout all testing is shown below. The lowest ambient temperature while running a test was recorded as 17.2 °C and the highest temperature was 24.05 °C. The graph below indicates that, although an ambient temperature of 22 °C was most frequently observed throughout the various tests, the variation in ambient temperature is a large source of error.

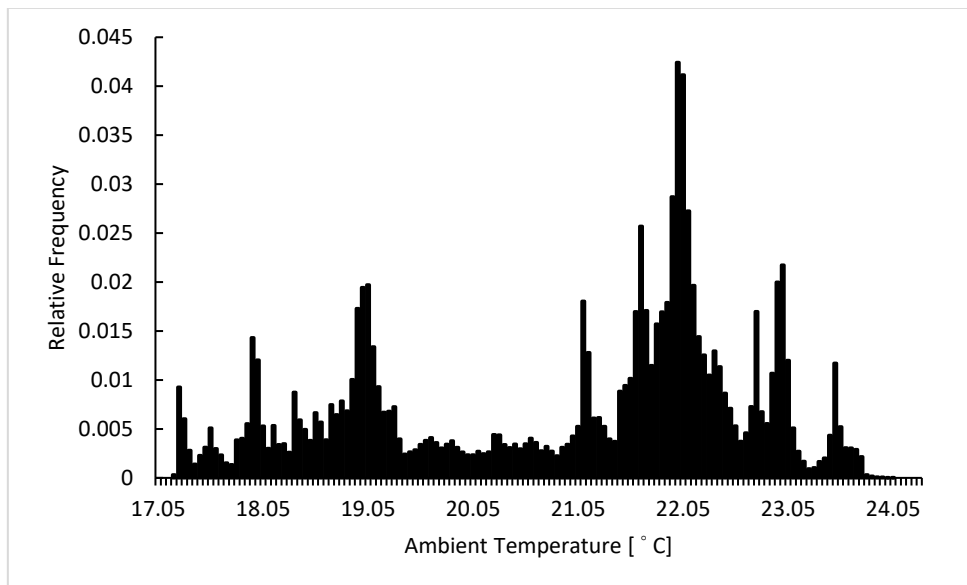


Figure 25: Test Ambient Temperature Readings

### 3.4 TEST PLAN

To obtain an in-depth understanding of the LHP operating characteristics, a specific series of tests were conducted. These were divided in the following major categories:

- Start-up at various heat loads
- Power cycle (sudden power changes)
- Sink cycle (sudden sink temperature changes)

Table 2 below gives an outline of what tests were performed and the different settings used for each test. For all tests, data was collected from all thermocouples every 2 seconds at the fastest setting possible by the DAS.

*Table 2: Testing Plan Outline*

Test No.	Start-up Power [W]	Sink Temp [ $^{\circ}$ C]	Power/ Sink Profile
1A	10	5	-
1B	25	5	-
1C	50	5	-
1D	100	5	-
2A	10	5	10W/25W/50W/100W/50W/25W/10W
2B	10	5	10W/50W/10W
2C	10	5	10W/100W/10W
2D	25	5	25W/50W/100W/150W/180W/210W/170W/160W/150W/125W/25W/10W/8W/6W/4W/3W/2W/1W
3A	10	5	5 $^{\circ}$ C /10 $^{\circ}$ C/15 $^{\circ}$ C/10 $^{\circ}$ C/5 $^{\circ}$ C
3B	25	5	5 $^{\circ}$ C /10 $^{\circ}$ C/15 $^{\circ}$ C/10 $^{\circ}$ C/5 $^{\circ}$ C
3C	50	5	5 $^{\circ}$ C /10 $^{\circ}$ C/15 $^{\circ}$ C/10 $^{\circ}$ C/5 $^{\circ}$ C
3D	100	5	5 $^{\circ}$ C /10 $^{\circ}$ C/15 $^{\circ}$ C/10 $^{\circ}$ C/5 $^{\circ}$ C

While the specific procedures for each of the tests vary, the general approach is the same. An example of the test procedure for test number 1A is provided below:

1. Start data acquisition
2. Set the condenser chiller to 5 $^{\circ}$ C. Wait 30 min or until steady-state is reached

3. Apply 10 W to the evaporator for start-up. Wait 30 min or until steady-state is reached
4. Turn power to the evaporator OFF. Wait 30 min
5. Stop data acquisition

As seen above, for each change applied to the LHP, a 30-min minimum waiting period is permitted for the LHP to achieve steady-state. This waiting period was previously determined through preliminary testing where, during data reduction, it was made sure that steady-state was reached for each case within the 30-minute window. Thirty minutes has shown to be sufficiently long to reach steady-state.

# CHAPTER 4 TEST RESULTS AND LHP CHARACTERIZATION

Although regular LHPs have been extensively studied, there is little open literature regarding those which make use of a two-way pressure regulating valve for temperature control. Testing of the LHP provides the required data to characterize the behaviour of the pressure regulated LHP and serves as a reference point against which the steady-state model can be compared.

This chapter presents the tests that were performed on the two-way PRV LHP to characterize its operation as a whole system and identify the behaviour of the pressure regulating valve. Multiple tests were explored to understand the LHP start-up and provide insight into the behaviour of the PRV. Tests consisting of step changes in applied power were further executed to understand the operation of the LHP under varying payload powers and the coupling effects, if any, between the evaporation zone and the condenser region. Finally, tests to examine the system response to step changes in the condensing region were performed.

## 4.1 START-UP

To gain an understanding of the whole-system response during start-up, thermocouple temperatures were averaged out among the LHP evaporator ( $T_e$ ) and CC ( $T_{cc}$ ) using the following expressions:

$$T_{evap} = \frac{1}{2} \left[ \frac{1}{2} (T_{101} + T_{103}) + T_{102} \right] \quad (16)$$

$$T_{cc} = \frac{1}{2} (T_{135} + T_{136}) \quad (17)$$

These values, along with inlet and outlet liquid and vapour line temperatures and temperatures in the middle of the condenser line, were then plotted as a function of time and presented as is shown below in Figure 26. It is important to note that the method used to average temperature readings in the evaporator differs from the CC because of the thermocouple locations. As such, values from both bottom thermocouples ( $T_{101}$  and  $T_{103}$ ) are first averaged and then averaged with the value from the top thermocouple ( $T_{102}$ ).

Sink temperatures were regulated by the water chiller which was set to its lowest setting at 5 °C. Ambient temperatures were recorded using thermocouples  $T_{113}$ ,  $T_{114}$ , and  $T_{115}$ , and were seen to fluctuate no more than 1.54 °C during all start-up tests.

Given the slow increase in saturation temperature at 10 W, Figure 26 provides great insight into the LHP behaviour during start-up prior to the PRV fully opening. As seen below, five major events in the start-up process were identified and labelled, each indicating different behaviours of the working fluid and LHP operation.

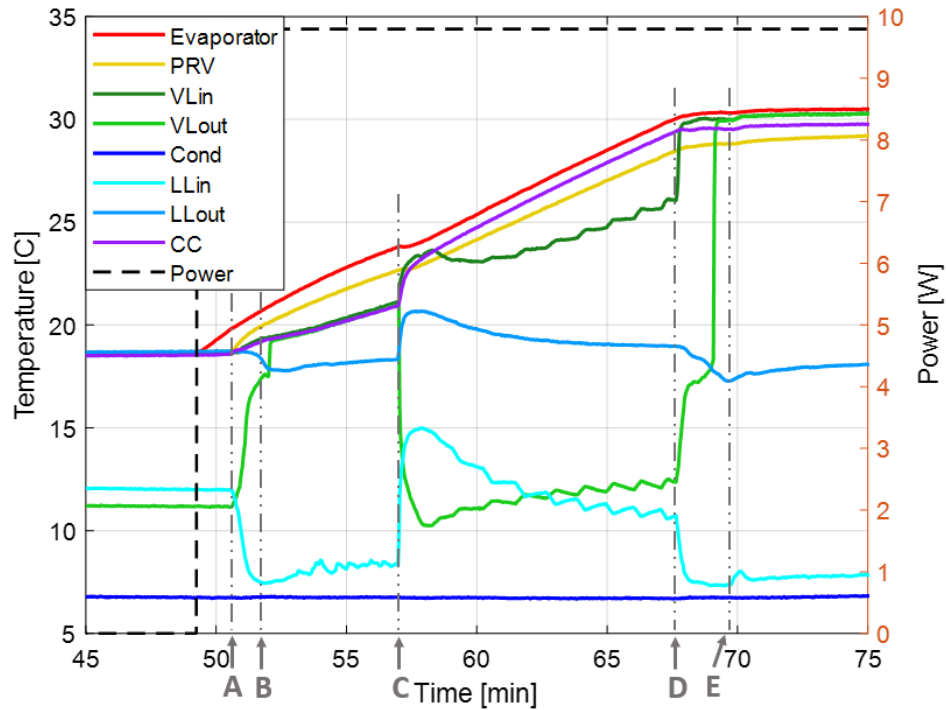


Figure 26: Test No. 1A - 10 W Start-up Test

Prior to A, power is applied, and heat is transferred to the LHP causing the evaporator temperature to rise and the ammonia to evaporate. Between A and B, the increase in vapour line and decrease in liquid line temperatures indicate fluid flow throughout the entire LHP which is only possible because of the presence of an orifice in the PRV as shown in Figure 27.

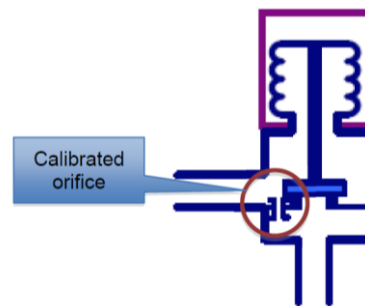


Figure 27: PRV Calibrated Orifice [16]

Vapour is seen to move from the evaporator to the vapour line causing these temperatures to increase, and liquid from the condenser is pushed into the liquid line causing temperatures to rapidly decrease in this section. Because the fluid saturation temperature is below the PRV setpoint temperature, the valve is

closed but some ammonia vapour is allowed to escape the evaporator region through the orifice. The LHP was designed such that it could achieve start-up under a wide range of combinations of low power and low temperature environments. Hence, the addition of the orifice allows for fluid to flow within the LHP under conditions which would normally not allow start-up [16].

Once all the subcooled liquid in the condenser moves into the liquid line and warmer fluid from the vapour line goes into the condenser, temperatures across the LHP gradually increase as seen between B and C. Because the mass flow rate of vapour escaping the evaporator is limited by the orifice, temperatures within the evaporator continue to rise and heat is mostly conserved in the system rather than being rejected by the condenser.

At approximately 57 minutes, liquid line temperatures increase, the vapour outlet temperature decreases. Although the LHP had achieved start-up, this was not sustainable because of the large restriction in mass flow rate imposed by closed PRV. Instead, data indicates a reverse flow in the LHP which can be best explained using Figure 28 which shows inlet and outlet thermocouple readings for both liquid and vapour lines in more detail.

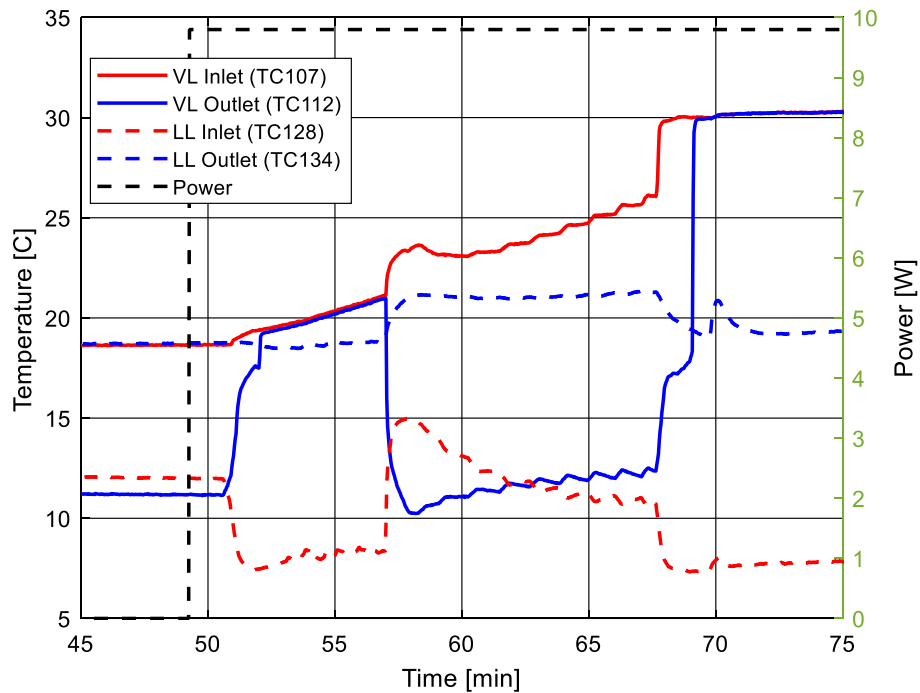


Figure 28: Inlet and Outlet Thermocouple Readings for a 10 W Startup Test

As seen above, the temperature at the exit of the vapour line ( $T_{112}$ ) drastically decreases, while the temperature at the exit of the liquid line ( $T_{134}$ ) increases. This suggests cold fluid from the sink was drawn into the vapour line and warm fluid from the CC was drawn into the liquid line. Because the vapour escaping through the orifice is not superheated, some of it may have condensed within the vapour line and created a momentary void which would draw fluid out of the CC into the liquid line. This also explains why both the liquid line and vapour inlet temperatures increase at this point.

Near point D, at approximately 68 minutes into the test, the drastic rise in vapour line temperatures and drop in liquid line temperatures suggest a second start-up together with the movement of the PRV piston that allows a larger flow of vapour into the vapour line. This behaviour is as expected because the average evaporator temperature is roughly 30 °C which, in accordance with the ammonia saturation line, corresponds to a saturation pressure slightly higher than that of the PRV setpoint pressure. The low oscillations observed in the vapour line indicate fluttering of the PRV piston as vapour is released into the line which cause oscillations at the vapour line inlet and outlet due to the movement of fluid interfaces. Past this point (between points D and E), the piston in the PRV settles on a position at which the system reaches steady-state operation.

Figure 29 to Figure 31 show the same experiment previously described but applying higher powers to the evaporator (25 W, 50 W, and 100 W). At 25 W, a quick increase in the vapour line outlet temperature and decrease in liquid line inlet temperature at 38 minutes once again suggest a premature start-up due to the presence of the orifice, followed by a second, more sustainable start-up, similarly to what was observed at 10 W. Figure 30 also shows the same behaviour at roughly 47 minutes although the amplitude and duration of these drastic changes in temperature decrease. In other words, the behaviour described for 10 W is also observable at higher start-up powers, and it becomes less apparent as can be seen in the figures below. This occurs due to the LHP achieving a faster start-up at higher levels of power. Comparing values recorded between the 10 W and 100 W start-up tests, the LHP reaches steady-state operation approximately 20 minutes after a power of 10 W is applied, as opposed to 5 minutes with a 100 W startup. This behaviour can be explained in terms of the rate at which the working fluid is superheated. With a larger power,

ammonia in the evaporator is superheated quicker than at a lower power. As a result, the saturation temperature within the evaporator reaches the PRV setpoint temperature quicker, causing the valve to open and allowing the condenser to reject heat from the system. The LHP starts regulating the evaporator temperature instead of simply conserving heat, and the system reaches steady-state.

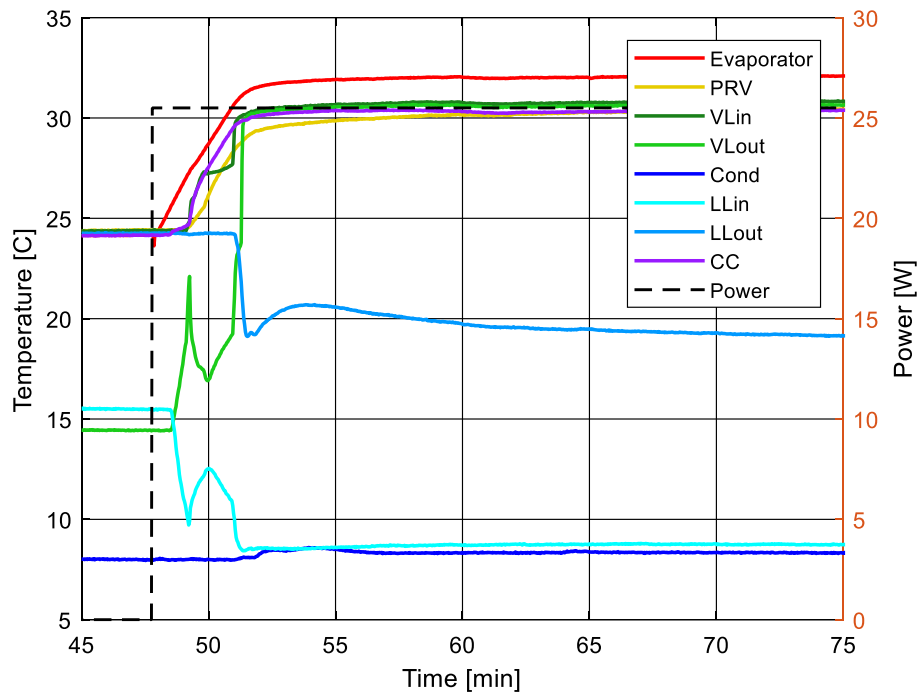


Figure 29: Test No. 1B - 25 W Start-up Test

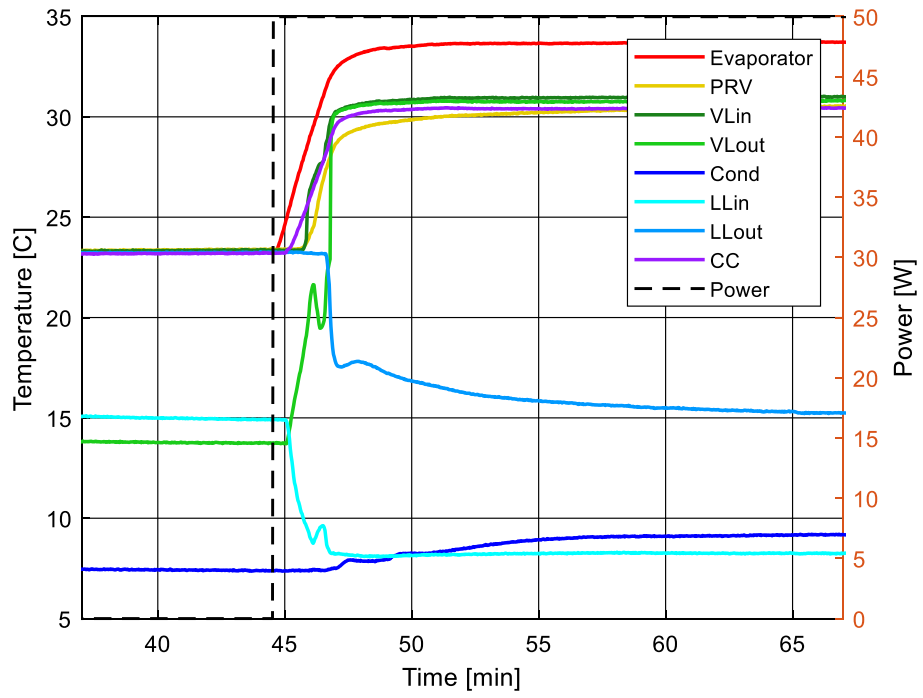


Figure 30: Test No. 1C - 50 W Start-up Test

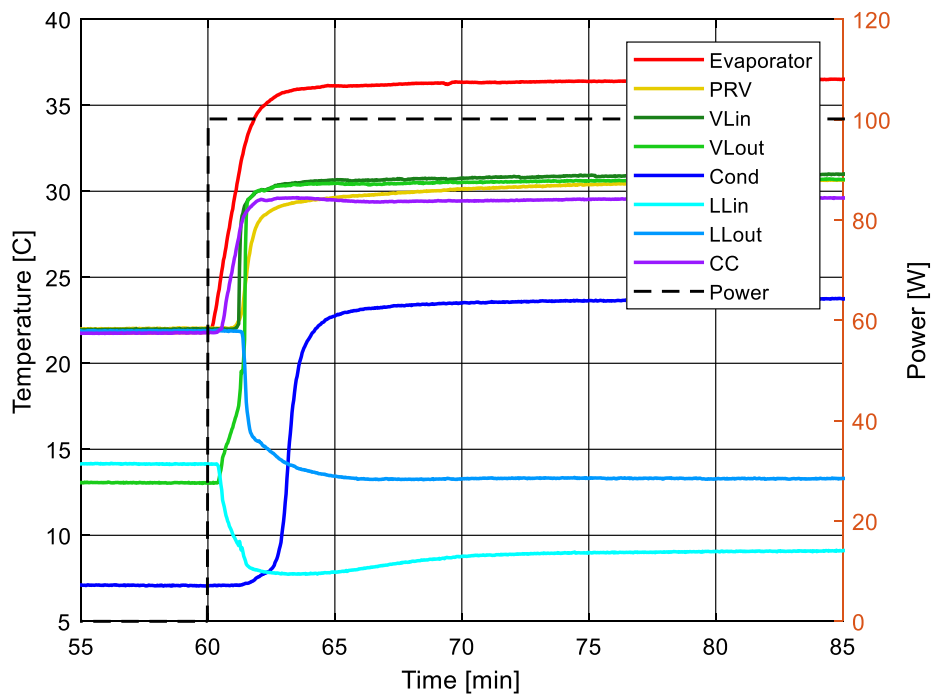


Figure 31: Test No. 1D - 100 W Start-up Test

## 4.2 POWER CYCLING

Power cycling tests consisted of measuring the temperature at various points along the LHP as successive stepwise increases and decreases of the heat load were executed. This was done in various combinations of power, as shown in Section 3.4, in order to understand the range of behaviour of each component of the LHP, and their step response.

Figure 32 shows temperature values for all components of the LHP as a function of time at a constant sink temperature of  $5^\circ\text{C}$ . The CC temperature is averaged out using Eq. 17 but, as opposed to before, the evaporator temperature is determined only using thermocouple  $T_{102}$  to obtain a better estimate of the LHP saturation temperature rather than the entire evaporator region temperature. A step increase or decrease was applied either after 30 minutes or once the system was deemed to have reached steady-state operation as previously explained.

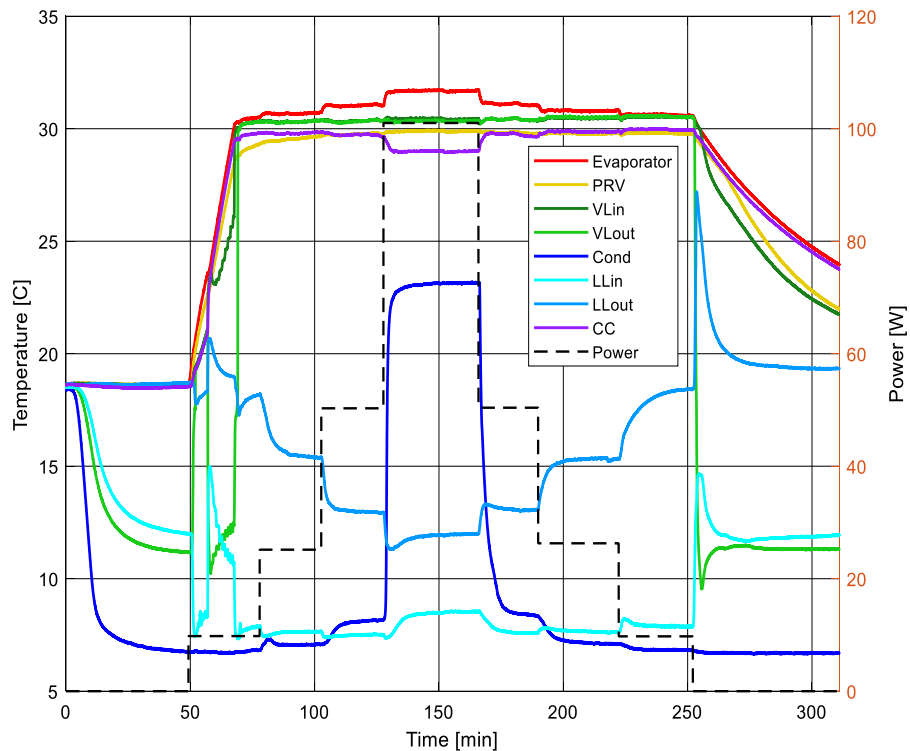


Figure 32: Test No. 2A – 10/25/50/100/50/25/10 W Power Cycle

As seen above, after start-up, an increase in applied power causes a rise in evaporator, condenser and liquid line inlet temperatures, and a decrease in compensation chamber and liquid line outlet temperatures. With increasing power, a larger amount of heat must be removed from the system and the vapour-to-liquid interface moves further along the condenser. This is shown by the increase in condenser temperature. With the movement of the interface closer to the condenser exit, liquid line inlet temperatures increase with increasing heat load since there is less distance within the condenser to sub-cool the working fluid. With more power supplied to the evaporator, an increase in the working fluid mass flow rate is expected which translates to the fluid being in the liquid line for a shorter duration. As a result, parasitic heat exchange with the ambient is reduced and the liquid line outlet temperature decreases between each step increase. Finally, colder fluid from the liquid line moves into the CC and hence the CC temperature is observed to slightly decrease.

Upon first inspection, the behaviour of the vapour line temperature is not as expected since it seems to remain constant as power is increased. Intuitively, an increase in evaporator temperature should cause an increase in vapour line temperature. This is the result of the presence of the PRV at the exit of the evaporator which serves the purpose of regulating evaporator temperatures. Vapour exiting the evaporator is expected to have a similar temperature to the evaporator if the PRV is not fully open (in regulating mode) since it is degrading LHP performance to maintain the desired evaporator temperature. Nevertheless, data from thermocouple  $T_{104}$ , which is located just after the evaporator and before the PRV, indicates the expected correlation between vapour temperature and heat load where, as power is increased, vapour temperature also increases as seen in Figure 33.

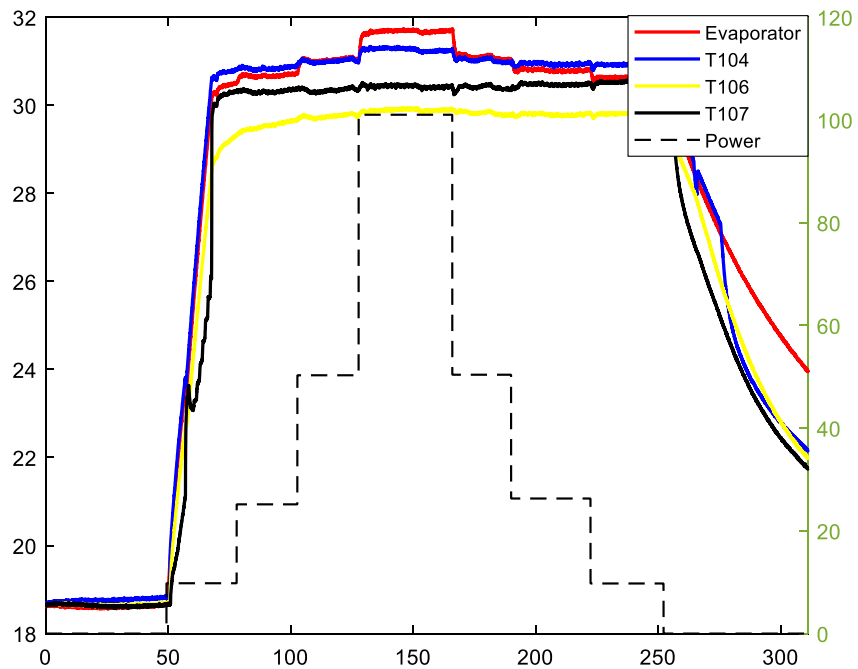


Figure 33: Test No. 2A - Temperatures surrounding PRV

Based on the behaviour of the evaporator and condenser temperatures, it can be concluded that between 50 W and 100 W, the LHP loses its regulating ability and switches to constant conducting mode. A noticeable increase in evaporator temperature and the drastic increase in the condenser temperature both are strong indications of this behaviour change. Nevertheless, since the condenser temperature in Figure 32 corresponds to a thermocouple located in the middle of the condenser path ( $T_{116}$ ), the spike in condenser temperature may only indicate that the vapour-to-liquid interface has moved past the middle of the condenser. To better access the regulating capacities of the LHP, a greater range of input powers were applied as shown below.

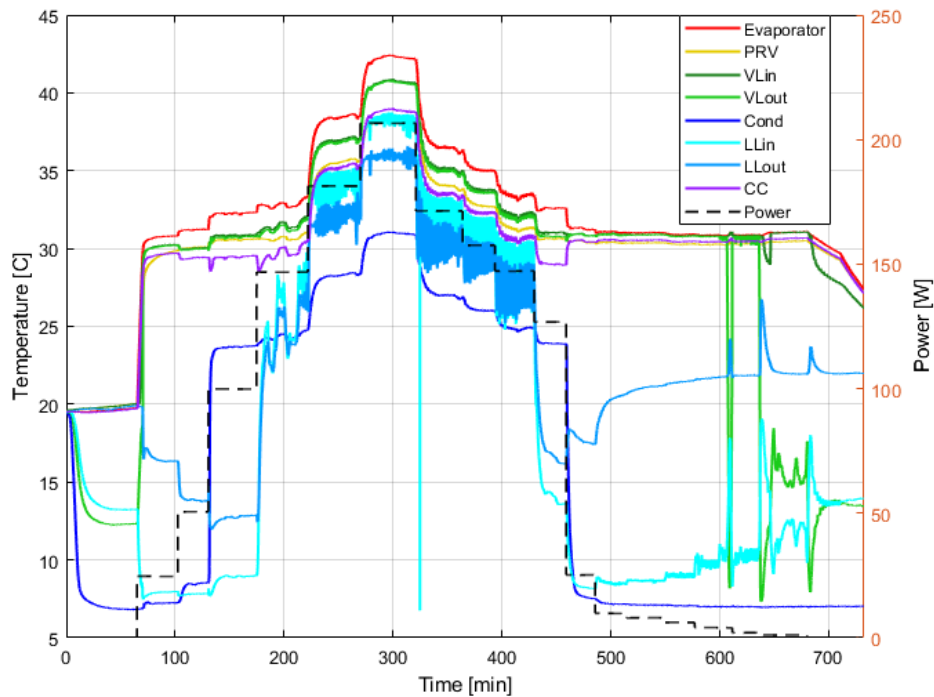


Figure 34: Test No. 2D - Large Range Power Cycle

Figure 34 shows a similar power cycle which was carried out over a larger range of powers than the test case previously discussed, testing the LHP at large heat loads from approximately 210 W, down to 1 W. During this test, the sink was kept at a constant 5 °C, and the stepwise increases and decreases were selected to encompass a larger variety of powers instead of being equally spaced apart at discrete heat loads. Based on the random oscillations seen above, information collected from powers below 6 W were discarded since they indicate that the LHP is no longer functioning. The observed spikes in LHP vapour and liquid line temperatures can be attributed to the effects of parasitic heat exchange being the same order of magnitude or higher than the input LHP power. Fluid within the LHP may thus randomly stop and move at such low powers resulting in the observed trend.

From start-up power to 100 W, the trends observed in Figure 34 match those observed in Figure 32, but once the heat load was increased to 150 W, differences in the LHP behaviour are noted. Large temperature oscillations in the liquid line become very prominent, and small temperature oscillations are also observed at the compensation chamber, vapour line, and evaporator. Furthermore, liquid line temperatures drastically increase suggesting that the

condenser is fully open and no longer able to sub-cool the working fluid. To better observe and explain this behaviour, the individual condenser thermocouple readings are plotted below as a function of time.

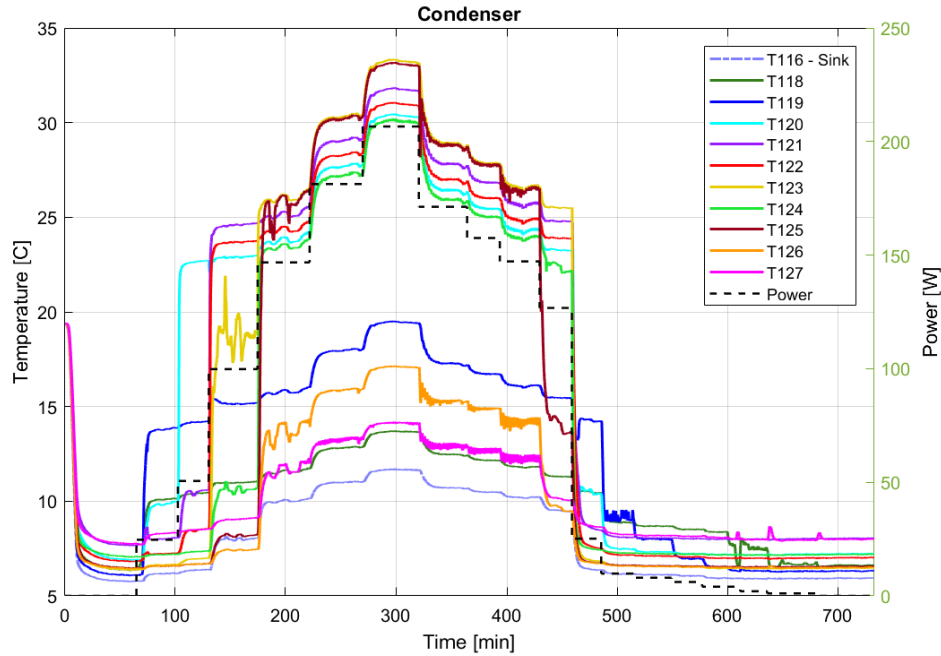


Figure 35: Test No. 2D – Condenser Temperature Readings

At the lower range of powers (below 100 W) some fluctuations with a small amplitude are visible. As power is increased from 25 W to 50 W, these fluctuations move from thermocouple  $T_{120}$  to  $T_{121}$  which indicates a movement of the vapour to liquid interface along the condenser. When the applied power is increased to 100 W, large fluctuations are clearly observed in thermocouple  $T_{123}$  which is also accompanied by a drastic increase in the temperature of  $T_{121}$  and  $T_{122}$ . This indicates that the interface is located around thermocouple  $T_{123}$  and past  $T_{121}$  and  $T_{122}$ . Following this logic, it is possible to determine the position of the interface along the condenser throughout the entire test. These results can be consulted in Table 3 below, although it is important to note that in some instances large temperature increases, or decreases are not noticeable.

Table 3: Condenser Behaviour by Thermocouple

Power [W]	Oscillations	Temp. Increase	Temp. Decrease	Conclusion
25	$T_{120}$	$T_{119}$	--	Int. after $T_{119}$
50	$T_{121}$	$T_{120}$	--	Int. after $T_{120}$
100	$T_{123}$	$T_{122}$	--	Int. after $T_{122}$
150	$T_{125}, T_{126}, T_{127}$	$T_{124}$	--	Int. after $T_{124}$
180	$T_{127}, T_{128}, T_{129}$	--	--	Int. after $T_{126}$ and at condenser exit
210	LL	--	--	Int. at liquid line. Condenser is fully open
170, 160	$T_{126}, T_{127}$	--	--	
150	$T_{125}$	--	--	
125	$T_{124}$	--	$T_{125}$	Int. before $T_{125}$
25	$T_{120}$	--	$T_{119}$	Int. after $T_{119}$

The thermocouple readings discussed above can be linked to the trends observed in the liquid line in Figure 34 because condenser and liquid line behaviours are effectively coupled. When the power is increased to 150 W, the temperature oscillations indicate that the vapour-to-liquid interface is located at the condenser exit which explains why oscillations become noticeable in the liquid line. Physically speaking, the oscillations indicate the presence of vapour and liquid simultaneously which explains why the liquid line temperature drastically increases; vapour at the interface (near the liquid line) causes temperature spikes along the liquid line. Because the interface is moving between the liquid line and the condenser, the oscillations present at this point have larger amplitudes. As power is further increased to 180 W, the oscillations decrease in amplitude but move further near the condenser exit. Upon inspection of liquid line thermocouples, the larger amplitude oscillations are at thermocouples  $T_{128}$  and  $T_{129}$  which are located on the liquid line. At 210 W, oscillations are not prominent in the condenser, but are observed in the liquid line, indicating the condenser is fully open and the vapour to liquid interface is now located in the liquid line. As power is decreased from the maximum applied value, the temperature oscillations in the liquid line behave similarly to when power was increased but have larger amplitudes. This is due to hysteresis effects which are common in LHPs.

With the interface moving near the exit of the condenser and into the liquid line, the LHP can be expected to behave as a constant conduction device and as such, the pressure regulating valve is expected to be fully open. Because the purpose of the valve is to control the evaporator temperature by degrading the LHP performance, test no. 2D can be expected to provide insight into how the valve affects the LHP performance as the valve piston moves from being fully closed with flow only through an orifice to fully opened. The corresponding performance curve is displayed below in Figure 36.

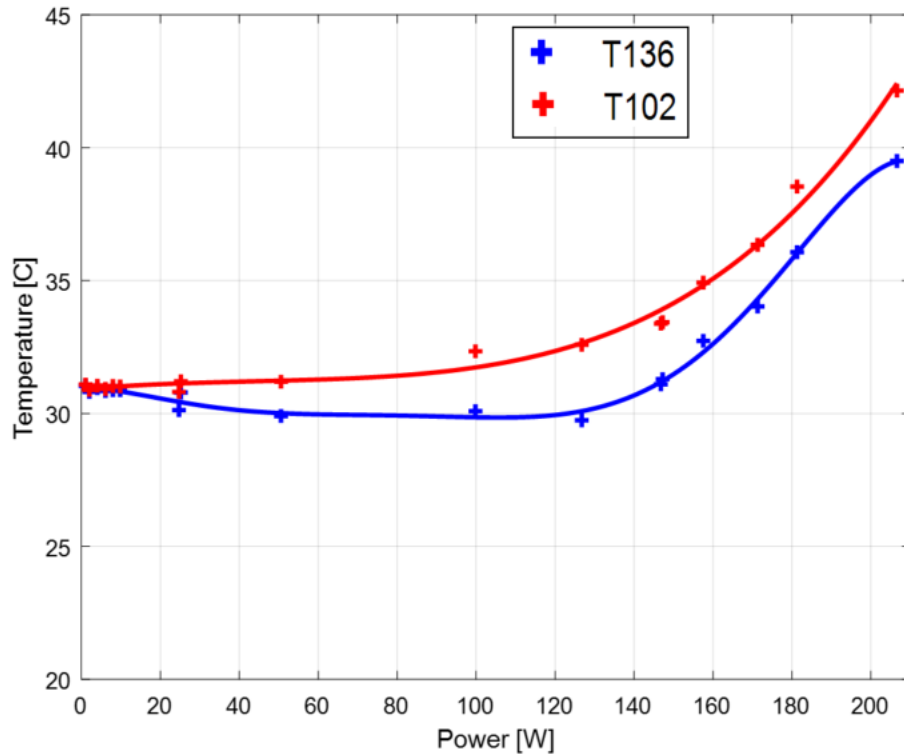


Figure 36: LHP Performance Curve

To obtain the performance curve above, the steady-state temperature values at each power step were plotted by using temperature readings recorded two-time steps before a change in heat load. Thermocouples  $T_{102}$  and  $T_{136}$  were plotted since they are located on the evaporator and compensation chamber, respectively, and provide the best indication of the LHP operation temperature. As clearly seen in Figure 36, the LHP is generally able to maintain a nearly constant operating temperature ( $30.49 \pm 0.17$  and  $31.28 \pm 0.18$  for CC and evaporator values, respectively) at heat loads below 130 W, after which it loses its ability to regulate temperature and operates in constant conductance mode.

Because of this, it is possible to say that at this point both the PRV and condenser are fully opened. It is important to note that temperatures recorded in the evaporator start increasing at lower powers compared to the CC due to conduction from the heater cartridge through the evaporator saddle as opposed to actual changes in fluid temperature. The trend observed in the LHP performance curve agrees with the trends reported in [10] which indicate an almost constant operation temperature maintained by a LHP with a 2-way PRV as opposed to a LHP without a PRV as shown below.

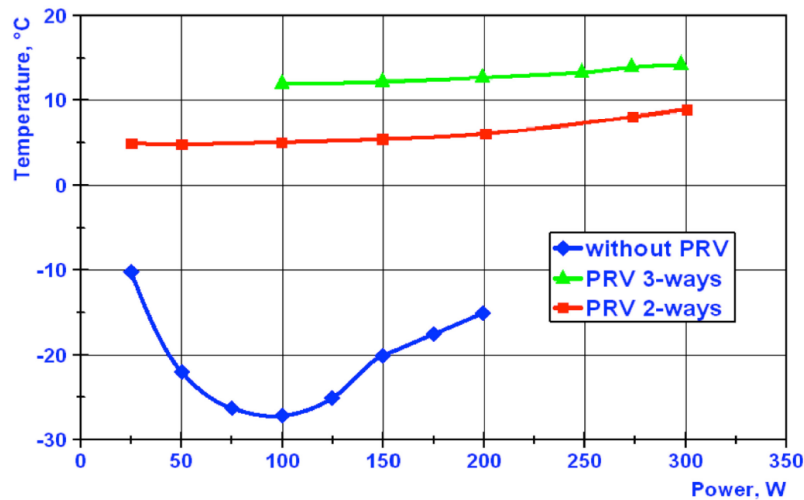


Figure 37: Modified LHP Operating Temperature [10]

### 4.3 SINK CYCLING

To gain an understanding of the system response to a variation in sink temperature, tests were performed at a constant power and by varying the chiller temperature from 5 °C to 15°C as indicated in Table 2. A minimum of 30 minutes between each step change in sink temperature was chosen to allow for the system to reach steady-state behaviour as done in previously mentioned tests. A plot of temperature versus time as shown in Figure 38 was constructed by combining the results obtained in tests 3A, 3B, 3C, and 3D and using Eq. 16 to calculate the evaporator temperatures. Since these tests were repeated at different power settings, some required longer waiting periods than others to reach steady-state and the results have been adjusted for visualization purposes and to better explain the underlying trends. To do so, sections which showed no variation in temperature were removed from the 10 W, 25 W, and 50 W

plots to fit the period of the 100 W test. When doing so, times at which a change in sink temperature were conserved to ensure all lines showed the instance when a temperature step was applied simultaneously.

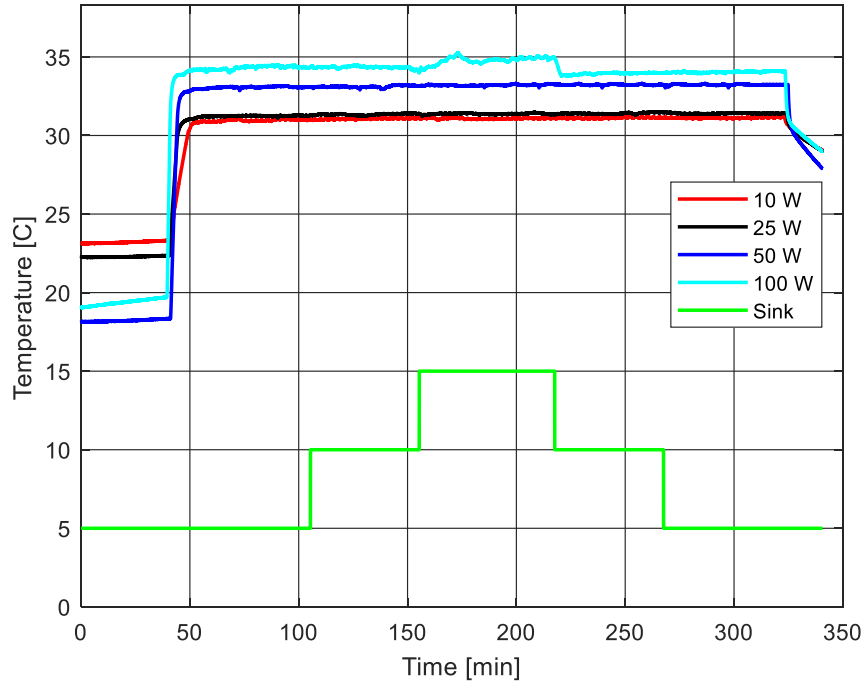


Figure 38: Sink Cycle Evaporator Temperatures

As seen above, the LHP is able to better control and maintain the evaporator temperature throughout the sink cycle at lower powers. By determining the minimum and maximum evaporator temperatures at each power, it was calculated that the average evaporator temperature varied within 1.69 °C, 0.58 °C, 0.44 °C and 0.43 °C at when the applied power was 100 W, 50 W, 25 W, and 10 W, respectively. At 100 W, the largest variation in temperature was observed when the sink was at its highest temperature setting, and a rapid jump in evaporator temperature is observed, followed by temperature fluctuations. By plotting thermocouple temperature readings of major sections of the LHP, it is identified that the fluctuations observed in the evaporator region are caused by abnormal behaviour in the liquid line as shown in Figure 39.

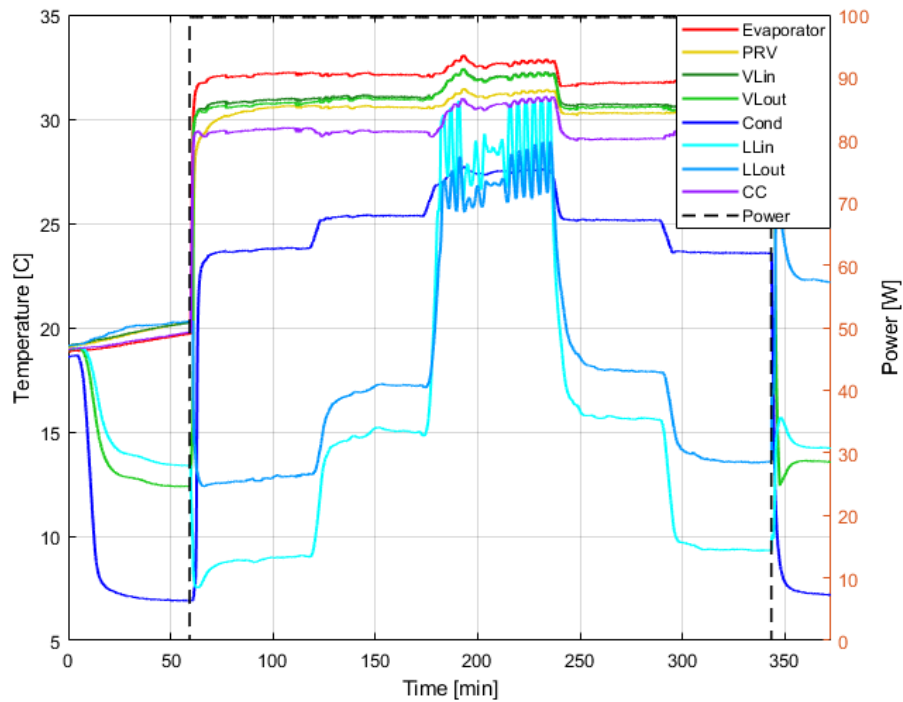


Figure 39: Test No. 3D – 100 W Constants Sink Cycle

In comparison to all other sink cycling tests, the one shown above was the only scenario in which liquid line temperatures increased past the condenser temperature. At this point, the LHP condenser is expected to be fully open and the interface is located within the liquid line, causing these fluctuations. Because this section of the LHP is directly linked to the compensation chamber, it greatly influences the evaporator’s ability to control and maintain a stable saturation temperature. Investigating the condenser using Figure 40 shows the motion of the interface through the different thermocouples. As the sink temperature is increased, the interface moves from being at the location of  $T_{123}$  to  $T_{124}$  and then to  $T_{126}/T_{127}$ . This can be deduced from the following graph by tracking the thermocouple temperatures which show oscillations after each increasing step input power. These two thermocouples display oscillations that have the same trend as those observed in the liquid line but with a lower amplitude. This further indicates that the location of the interface is within the liquid line.

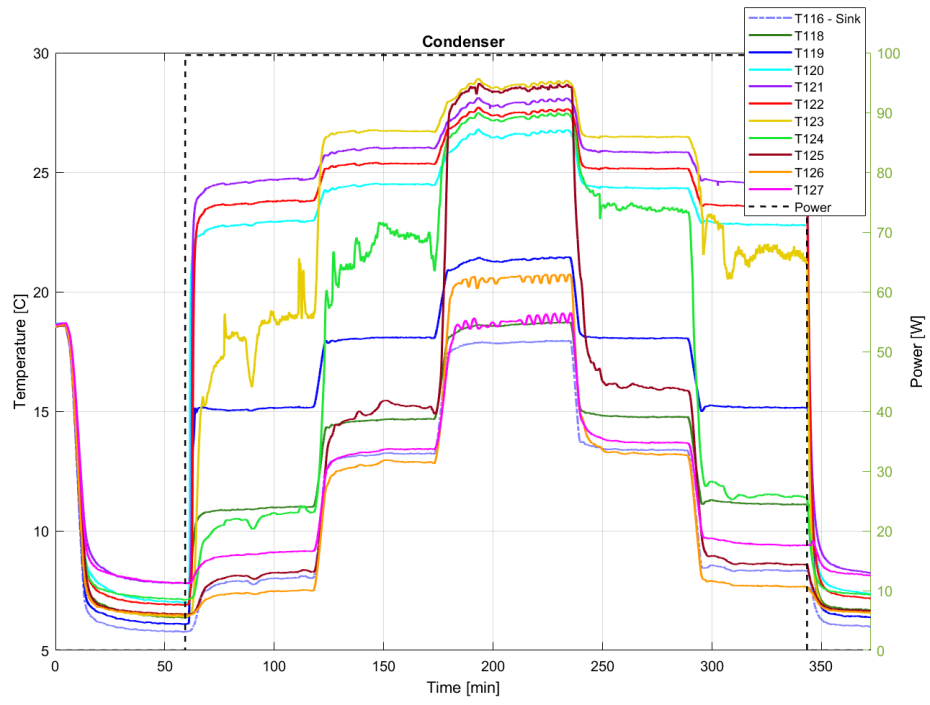


Figure 40: Test No. 3D – Condenser Temperature Readings

# CHAPTER 5 MATHEMATICAL MODEL

Mathematical models have been extensively used to understand and predict the operation and behaviour of LHPs. Steady-state models are useful to study and size LHP characteristics and run parametric studies to determine optimum layouts for a heat pipe for any given application.

Various steady-state models with several degrees of complexity have been developed, as found in [1] [13] [17]; nevertheless, few transient models have been developed to predict LHP behaviour when transitioning from one steady state to another. In this chapter, a new steady-state model is presented as an improvement upon previous models and for the goal of being used as an input for a new transient model. In addition, this new steady-state model introduces the effects of a two-way PRV on the LHP operation as opposed to other models commonly found in literature which are only developed for unregulated LHPs.

## 5.1 OVERVIEW

In general terms, the steady-state model operates by dividing the entire LHP into various main components and propagating the properties of the working fluid from one component to the next based on the initial and boundary conditions specified. The model uses the governing equations of fluid dynamics and the state equations of the working fluid's properties to model the heat transfer process and flow of working fluid from the evaporator, through the vapour line, condenser, and liquid line, back to the compensation chamber. Once the loop is complete, the model checks if the final state of the compensation

chamber agrees with the initial state of the evaporator and continues iterating until convergence has been achieved. The overall process is described below.

### 5.1.1 Governing Equations

Mass conservation, energy conservation, and linear momentum conservation equations are used as the governing equations in the steady-state model. Since the majority of LHP components are made from pipes, a cylindrical coordinate system is adapted throughout the model. Furthermore, fluid flow in the model is restricted to axial flow and thus assumed to be one-dimensional; although some sections such as the evaporator transfer heat radially to the pipe (specific cases shall be highlighted ahead). Using a control volume approach to analyze the fluid flow through components in the LHP, an Eulerian approach is used to develop these three equations.

The mass conservation equation was derived based on the assumptions stated above and modified to show that the density is the main parameter that changes with time, taking the form of

$$\left( V \frac{d\rho}{dt} \right)_{cv} = (A \rho u)_{in} - (A \rho u)_{out} \quad (18)$$

where  $A$  is cross sectional area,  $\rho$  is density,  $u$  is velocity, and  $V$  is volume. This form of the equation comes from the fact that the control volume has a fixed volume.

The momentum conservation equation shown below explains that across a control volume, viscous and gravity forces result in a change in pressure of the fluid. This can be expressed as

$$(P A)_{in} - (P A)_{out} = (\rho g A \Delta Z)_{cv} + \xi \frac{\rho u^2}{2} A_{cv} \quad (19)$$

where  $P$  is pressure,  $\Delta Z$  is a change in height across the control volume, and  $\xi$  is the pressure drop coefficient, which can be calculated from the control volume effective length ( $L$ ), diameter ( $D$ ), and the friction factor ( $f$ ) as shown below.

$$\xi = \frac{L}{D} f \quad (20)$$

It is important to note that the inertia term in the momentum equation was ignored given that it is negligible [18] [19]. The energy conservation equation takes on different forms based on the type of material and the dominant methods of heat transfer. As such, two forms are used in the model: one for solid components and another for the working fluid, shown respectively as Eq. 21 and Eq. 22.

$$\left( V \rho c_p \frac{dT}{dt} \right)_{cv} = (h A \Delta T)_{in} - (h A \Delta T)_{out} + \dot{Q} \quad (21)$$

$$\left[ V \left( \rho \frac{de}{dt} + e \frac{d\rho}{dt} \right) \right]_{cv} = (A \rho u \mathit{h})_{in} - (A \rho u \mathit{h})_{out} + (h A \Delta T)_{conv} \quad (22)$$

where  $c_p$  is the specific heat,  $h$  is the heat transfer coefficient,  $e$  is the internal energy per unit mass,  $\mathit{h}$  is the enthalpy of the fluid, and  $\dot{Q}$  represents any heat source at the control volume (such as the heater).

When deriving the energy equation for the control volume of a solid component, the thickness of the solid along the heat transfer path was deemed negligible compared to the other dimension and, as a result, resistance of the solid to heat conduction was assumed to be zero. This assumption applies particularly to solid components such as the pipes of the LHP given their small thickness yet may not be valid for the evaporator or the sink given their complex geometry or contact resistance between solid component.

For the control volume of the working fluid, the energy equation was derived based on heat transfer occurring from the mass flow entering and exiting the control volume. It was assumed that the density and internal energy of the fluid can change across the control volume.

### 5.1.2 Discretization

To apply the governing equations and propagate fluid properties, each component of the LHP is discretized into smaller control volumes. As a result, the control volume for the fluid is defined based on a staggered grid as shown below, with most solid components (piping walls) being discretized similarly to match the fluid cells.

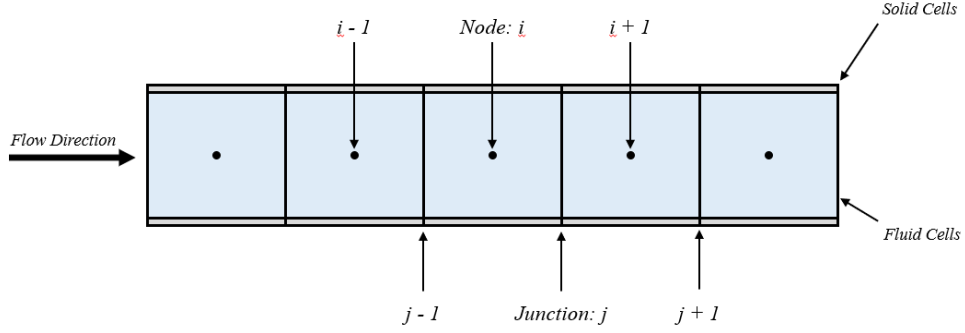


Figure 41: Staggered grid discretization of LHP components

Using this staggered grid approach, it is possible to specify boundary conditions at each control volume to solve the three governing equations. Fluid properties are defined at the centre of the control volume, denoted ‘node’, except for the fluid velocity that is specified at the boundaries of the control volume, called ‘junction.’ Because of this allocation, the mass conservation and energy conservation equations are solved for the nodes and the linear momentum conservation equation is solved for the junctions. Using the concept of nodes and junctions, these three equations can be rewritten as:

$$(V \dot{\rho})_i = (A \rho u)_{j-1} - (A \rho u)_j \quad (23)$$

$$(P A)_i - (P A)_{i+1} = (\rho g A)_j (Z_{i+1} - Z_i) + \left( \xi \frac{\rho u^2}{2} A \right)_j \quad (24)$$

$$(V(\rho \dot{e} + e \dot{\rho}))_i = (A \rho u h)_{j-1} - (A \rho u h)_j + (h A \Delta T)_i \quad (25)$$

where “i” represents nodes and “j” represents junctions. It is important to clarify that the energy equation for solid components does not get rewritten using the node and junction convention since solid cells are not using a staggered grid;

they are simply discretized to match the same dimensions as the fluid cells. The left-hand side of Eq. 23 and Eq. 25 is set to zero to obtain the steady-state solution.

In certain instances, such as Eq. 24, fluid properties other than velocity need to be defined at junctions. For such cases, the direction of the flow is used to define these properties based on adjacent nodes. This is accomplished by means of Eq. 26. On the other hand, if velocity is required at a node, the value is obtained by using the two adjacent junction velocities as shown below.

$$\begin{aligned} \varphi_j &= \delta \varphi_i + (1 - \delta) \varphi_{i+1} \\ \delta &= \begin{cases} 1 & \text{if } u_j \geq 0 \\ 0 & \text{if } u_j < 0 \end{cases} \end{aligned} \tag{26}$$

Figure 41 shows the discretization of LHP piping as an example for the control volumes used for solid parts of the system. More specifically, piping control volumes are defined as hollow cylinders of equal length to the fluid cell it surrounds. Control volumes for other solid parts of the LHP are defined based on the main component's geometry and the direction of heat flow.

### 5.1.3 Solid Cell and Fluid Cell Properties

Similarly to how solid and fluid cells are discretized differently, the material properties that are required to solve the governing equations also depend on the type of cell being analyzed. For solid cells, the properties that need to be defined in the steady-state model are specific heat, density and thermal conductivity, which are determined from material properties of the solid component. These properties are assumed to be constant through the conditions at which the LHP operates under.

On the other hand, properties of the working fluid heavily depend on temperature and pressure which greatly vary during the operation of the LHP. The required fluid properties consist of density, internal energy, enthalpy, viscosity, thermal conductivity, specific heat at constant pressure and surface tension. To determine these fluid properties, the steady-state model makes use of the tables and state equations defined within Reference Fluid

Thermodynamic and Transport Properties Database (REFPROP), a program developed by the National Institute of Standards and Technology (NIST). Using add-ons developed by NIST which allow the user to call REFPROP using MATLAB code, the model is able to determine fluid properties of the working fluid regardless of its fluid state (liquid, vapour or two-phase).

#### 5.1.4 General Algorithm

Figure 42 summarizes the general algorithm which is implemented in the model to solve for the steady-state behaviour of the LHP. This section gives a general explanation of the algorithm and references subsequent sections where more detail is presented on individual parts of the model.

The model starts by calling scripts which provide the necessary physical properties that describe and define the LHP and its operational envelope. This includes LHP component dimensions, material properties, surrounding temperatures, as well as the power which is applied to the evaporator region, among others. Next, the model proceeds to discretize all LHP components into smaller control volumes as previously mentioned, assigning the corresponding properties to each cell based on their location within the LHP.

With these initial and boundary conditions defined (see Section 5.2.1 for further detail), the model generates an initial guess of the interface temperature and the evaporator to compensation chamber heat leak. Using these guesses, the model proceeds to solve for the cells within the evaporator case, determining mass flow rates and solving for fluid properties within the vapour grooves as described in Section 5.2.2.

Now that fluid properties are defined at the initial boundary of the vapour line, the model proceeds to loop through each cell of the transportation line (vapour line, condenser, and liquid line). For each cell, as described in Section 5.2.3, mass continuity and linear momentum conservation equations are used to propagate fluid properties forwards and calculate fluid pressures. Saturation and solid cell wall temperatures are calculated, resulting in the state of fluid and solid cells being propagated from the first cell of the vapour line to the last cell of the liquid line.

Having propagated working fluid properties to the CC boundary, fluid properties at the compensation chamber are calculated as shown in Section 5.2.4. The heat leak across the wick (from the evaporator to the compensation chamber) is then calculated using two different approaches: energy conservation and conduction through the wick and compared to determine if the steady-state model has converged or not. If it has not, the model calculates a new interface temperature and, using the new evaporator-to-compensation chamber heat leak, repeats the process starting from the evaporator case, and continues iterating until convergence has been achieved. After this point, the model proceeds to solve the wick as described in Section 5.2.5 and presents the results.

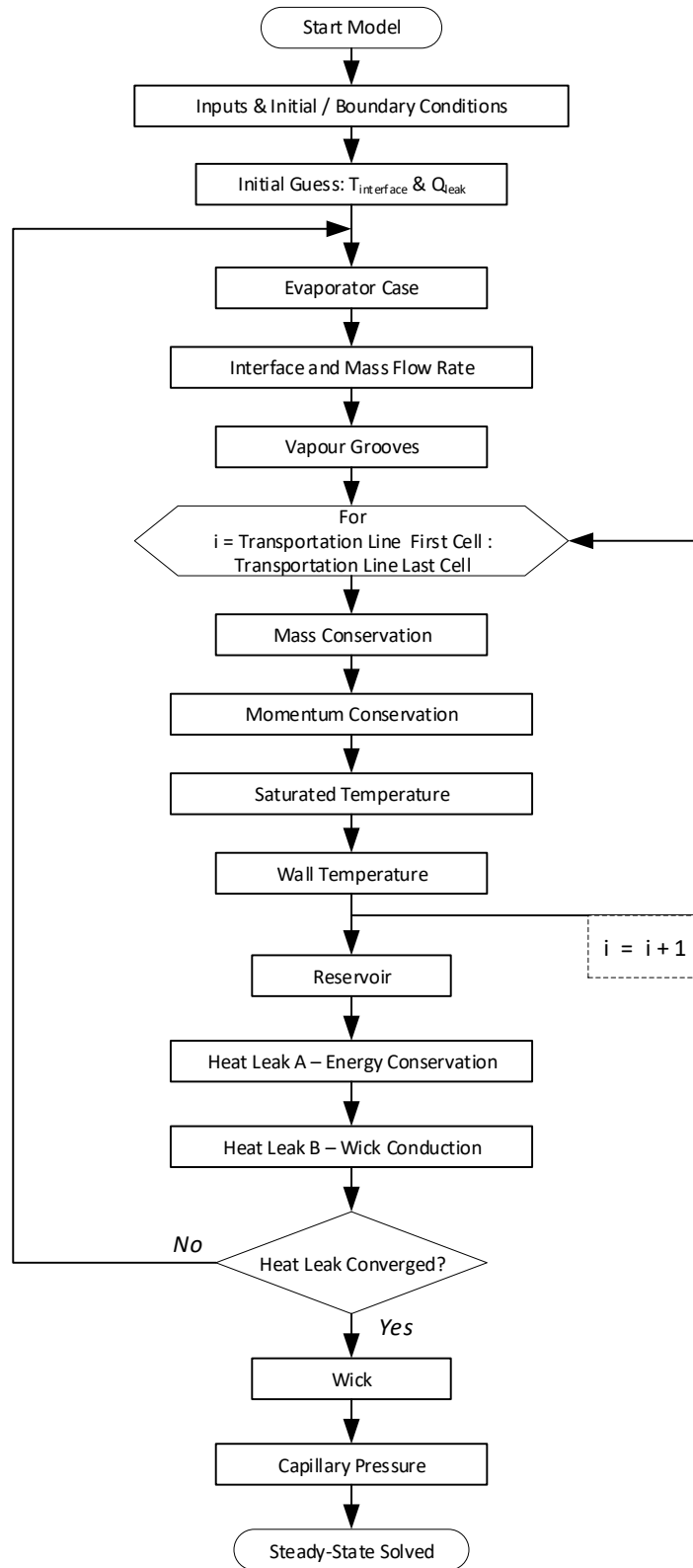


Figure 42: General Steady-State Model Algorithm

## 5.2 LHP COMPONENT MODELING

This section provides information on the specific inputs used in the mathematical model and a more in-depth explanation of the steady-state model and how each of the individual components of the LHP are treated.

### 5.2.1 Inputs and Initial/ Boundary Conditions

The first step in the mathematical model consists of defining the geometry of the LHP and its components. To do so, a MATLAB script is used to define all the dimensions and properties that are listed below. Note that specific properties of the working fluid do not need to be defined given that they are frequently obtained using REFPROP based on other properties (such as temperature, pressure and quality).

- Wick: length, internal diameter, external diameter, porosity, permeability, pore radius, conductivity, density, and specific heat
- Evaporator Casing: length, internal diameter, external diameter, density, and specific heat
- Vapour Grooves: length, diameter, and number of grooves
- Vapour Line: length, internal diameter, external diameter, density, and specific heat
- Condenser: length, internal diameter, external diameter, density, and specific heat
- Liquid Line: length, internal diameter, external diameter, density, and specific heat
- Compensation Chamber Casing: length, internal diameter, external diameter, density, and specific heat

The conditions under which the LHP operates must then be defined by the user. This includes the power applied to the evaporator (to simulate the device that the LHP needs to reject heat from), the temperatures which define the LHP surroundings (ambient temperature and sink temperature), and the type and amount of working fluid contained within the LHP. The user must also specify whether different parts of the LHP are insulated or not and the

corresponding heat transfer coefficients (HTC) between the casing-wick, and wall-sink.

Once the program is initiated, the model proceeds to discretize each of the LHP components and assigns corresponding properties to the newly defined control volumes. This is done by creating matrices for each component where each row corresponds to each discretized control volume, and each column defines different properties. This is done to keep track of not only physical properties (for example, solid cell No. 1 has a density of  $7900 \text{ kg/m}^3$  because it corresponds to the evaporator, which is made of stainless steel), but also to ensure that boundary conditions are properly applied (for example, solid cell No. 80 is located inside the condenser and hence has a boundary condition that matches the sink temperature).

As initial conditions, the interface temperature is set to be equal to the ambient temperature, and the heat leak is set to be 0.1 % of the applied power. These initial guesses were deemed suitable based on the results of various trial and errors, taking into consideration solving speed and model convergence.

### 5.2.2 Evaporator

The first component that is analyzed within the iterative scheme is the evaporator. Having defined a percentage of the applied power that goes to the grooves, the applied power is divided to determine the heat going to the wick ( $\dot{Q}_{case2wick}$ ) and into the grooves ( $\dot{Q}_{case2grooves}$ ) and to determine the temperature of the evaporator casing. It was found that assuming 0.1 % of the total power goes to the grooves produced the most stable model results, with the remaining amount being directed to the wick. Assuming that fluid entering the wick is purely liquid and that fluid leaving the interface is purely vapour, and using the initial guess of heat leak ( $\dot{Q}_{hl}$ ) and interface temperature, the fluid enthalpy entering and leaving the interface can be determined using REFPROP and the mass flow rate can be calculated using:

$$\dot{m} = \frac{\dot{Q}_{case2wick} - \dot{Q}_{hl}}{h_{int,out} - h_{int,in}} \quad (27)$$

The fluid pressure in the grooves can be determined with REFPROP by using the interface temperature and assuming saturated vapour. Enthalpy leaving the grooves can be calculated with Eq. 28 because of conservation of energy and, with enthalpy and pressure, fluid temperature, quality and density at the grooves can be determined with REFPROP.

$$h_{gro,out} = h_{int,out} + \frac{\dot{Q}_{case2grooves}}{\dot{m}} \quad (28)$$

Finally, the velocity of the fluid exiting the grooves is calculated using the mass flow rate, the density of fluid at the grooves ( $\rho_{gro}$ ), and the total groove cross-sectional area ( $A_{gro}$ ).

$$u_{gro,out} = \frac{\dot{m}}{\rho_{gro} A_{gro}} \quad (29)$$

### 5.2.3 Transportation Lines and Condenser

As described in Section 5.1.4, the transportation line and condenser portion of the model is characterized by a loop that cycles through each of the cells, one by one, solving for and propagating fluid properties and solid cell temperatures. First, the model calculates the velocity-density product as per mass conservation, obtaining these properties from the past junction.

Next, the pressure of the fluid is determined by calculating the frictional pressure drop across the cell and using the linear momentum equation. Given that this pressure drop is dependent on the fluid state (vapour, liquid or mixture), these calculations shall be explained separately in greater detail in Section 5.3. Furthermore, when implementing the PRV in the steady-state model, an additional pressure drop is introduced at a specific cell which would correspond to the position of the PRV along the vapour line. Since this pressure drop is not fixed and depends on various factors such as the applied power (which dictates the valve position), an explanation of the PRV modeling and implementation in the model shall be explained separately in Section 5.6.

Using the newly obtained fluid pressure, the saturated temperature is calculated using REFPROP and the model proceeds to calculate the solid cell (wall) temperature. Because the wall temperature does not only depend on the fluid temperature, but also depends on the outside temperature (either ambient or sink, depending on location) and heat transfer coefficients between the ambient and wall, an iterative scheme is used to ensure these values match. As such, the 'Wall Temperature' block in Figure 42 can be expanded to the flow chart shown in Figure 43.

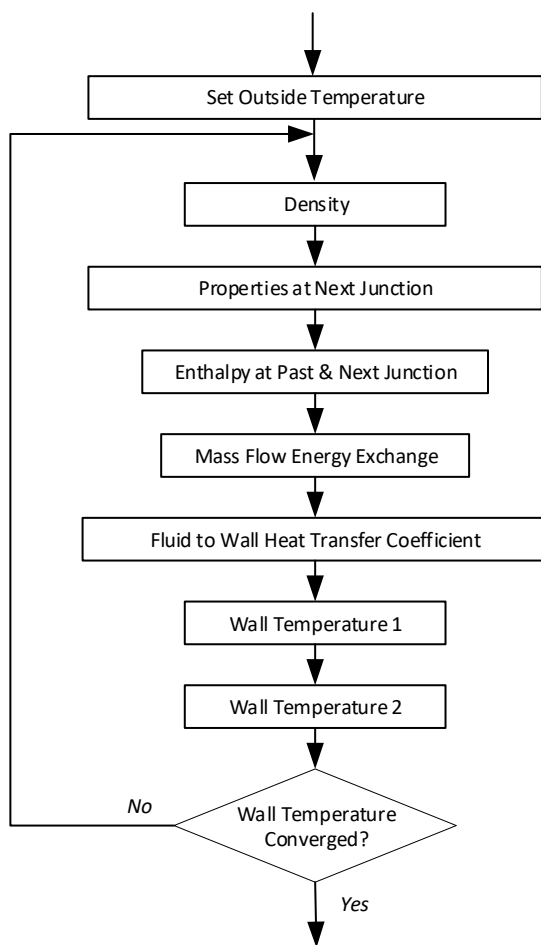


Figure 43: Wall Temperature Iteration Algorithm

Based on the location of the cell with respect to the entire LHP, the temperature outside of the solid cell is set to either ambient or sink. The density at the fluid cell is calculated using REFPROP which is then used to determine the velocity at the next junction using the velocity-density product that had previously been mentioned. Temperature, quality and density are then

propagated forwards from the node to the next junction. REFPROP is once again used to determine the enthalpy at both the past ( $i$ ) and next ( $i + 1$ ) junction surrounding the cell, and the mass flow energy exchange ( $\dot{q}$ ) is subsequently calculated using:

$$\dot{q} = (\rho u h)_j - (\rho u h)_{j+1} \quad (30)$$

Knowing all fluid properties in the cell and the conditions outside the cell wall, the fluid to wall heat transfer coefficient can be estimated. The method used to calculate this value is discussed in Section 5.4. Finally, the solid cell (wall) temperature is calculated using two different approaches and compared to determine convergence. The first method calculates the wall temperature ( $T_{wall}$ ) from the fluid cell energy balance equation:

$$T_{wall1} = T_i - \frac{\dot{q}}{4h_{fluid,wall}(L/D_{inner})} \quad (31)$$

where  $T_i$  is the temperature of the fluid cell and  $h_{fluid,wall}$  is the heat transfer coefficient calculated in the step above. The second method calculates the wall temperature from the solid cell energy balance equation. Depending on the location of the cell, a different form of the equation is used, with Eq. 32 used when the cell is in the condenser, Eq. 33 when the cell is in an insulated transportation line, and Eq. 34 when the cell is in a non-insulated transportation line.

$$T_{wall2} = T_{sink} + \frac{\dot{q} D_{inner}^2}{4 L h_{sink,wall} D_{outer}} \quad (32)$$

$$T_{wall2} = T_{amb} + \frac{\dot{q} D_{inner}^2}{4 L D_{outer}} \quad (33)$$

$$0 = \dot{q} - \left( \frac{1.32}{D_{outer}^{0.25}} \right) |T_{wall2} - T_{amb}|^{0.25} (T_{wall2} - T_{amb}) \quad (34)$$

Eq. 34 is solved using MATLABs 'fsolve' function, with the average between solid and fluid cell temperatures as the initial guess. Both wall temperatures are

compared, and the model iterates by adjusting the fluid cell temperature until the difference between both wall temperatures is less than the predetermined tolerance value, typically set to  $10^{-7}$ . An overview of the method of iteration is shown in Appendix A.

#### 5.2.4 Compensation Chamber

The last component that is analysed by the steady-state model is the CC, which is done as a single cell in the loop. With properties of the previous cell defining the past junction of the CC cell, the pressure of the fluid is calculated as explained in Section 5.3 and the saturated temperature is calculated, assuming saturated liquid within the CC, using REFPROP. Similarly to the transportation lines, the enthalpy at the past and next junction surrounding the CC are determined using REFPROP, and the mass flow energy exchange ( $\dot{q}$ ) is calculated using an alternative form of Eq. 30 which uses mass flow rate instead of the density-velocity product:

$$\dot{q} = \dot{m} (h_j - h_{j+1}) \quad (35)$$

The heat leak from the evaporator to the CC is then calculated using two methods, and the difference between both is used to determine whether or not the entire LHP steady-state solution has converged. The first method consists of calculating the heat leak using energy balance at the CC, and the second method calculates the heat leak by means of conduction through the wick. The former approach requires the need to calculate the heat transfer coefficient (HTC) between the CC wall and the surroundings if the CC is not insulated. Assuming natural convection, the HTC is calculated for both laminar and turbulent conditions with Eq. 36 and Eq. 37 respectively [20].

$$h_{laminar} = \frac{1.32}{D_{outer}^{0.25}} |T_{cc} - T_{amb}|^{0.25} \quad (36)$$

$$h_{turbulent} = 1.24 |T_{cc} - T_{amb}|^{0.333} \quad (37)$$

The heat being transferred between the CC and the surroundings ( $\dot{q}_{cc,amb}$ ) is calculated using

$$\dot{q}_{cc,amb} = h_{cc,amb}(T_{cc} - T_{amb}) \quad (38)$$

where  $h_{cc,amb}$  is the greater between the laminar and turbulent heat transfer coefficient for a more conservative approach,  $A$  is the interface area between the CC and its surroundings, and  $T_{cc}$  is the CC saturated temperature [20]. Writing the energy balance equation, the heat leak from the CC ( $\dot{q}_{hl,e}$ ) is balanced out by the energy transferred from the mass flowing into the cell ( $\dot{q}$ ), and the heat transfer with the surroundings ( $\dot{q}_{cc,amb}$ ).

$$\dot{q}_{hl,e} = \dot{q}_{cc,amb} - \dot{q} \quad (39)$$

The second method used to calculate the heat leak involves calculating heat leak by conduction through the wick. To do so, the effective thermal conductivity of the fluid in the wick is calculated assuming only saturated liquid exists in the wick at all times. Since the wick is comprised of both a solid (wicking material) and a liquid (working fluid), the effective wick conductivity ( $k_{w,eff}$ ) is calculated using Maxwell's correlation proposed by Dunn and Reay for sintered metal wicks [19].

$$k_{ratio} = \frac{k_{fluid}}{k_w} \quad (40)$$

$$k_{w,eff} = k_w \frac{[2 + k_{ratio} - 2\omega(1 - k_{ratio})]}{[2 + k_{ratio} + \omega(1 - k_{ratio})]} \quad (41)$$

where  $k_{fluid}$  and  $k_w$  are the thermal conductivities of the working fluid and the wick material, respectively, and  $\omega$  is the wick porosity. The heat conducted across the wick ( $\dot{q}_{hl,w}$ ) is then calculated using the equation below, where  $D_{outer,w}$  and  $D_{inner,w}$  are the wick outer and inner diameters, respectively, and  $L_w$  is the wick length.

$$\dot{q}_{hl,w} = \frac{2\pi k_{w,eff} L_w (T_{int} - T_{cc})}{\ln\left(\frac{D_{outer,w}}{D_{inner,w}}\right)} \quad (42)$$

Finally, the model proceeds to iterate upon heat leak values as shown in Appendix B.

### 5.2.5 Wick

Once the model has converged and a steady-state solution has been obtained, the last step in the model is to solve the wick assuming a single layer and zero thickness interface. The density and viscosity of the fluid within the wick is calculated using REFPROP, and the pressure drop caused by the wick is calculated using the Darcy equation [19]:

$$\Delta P_w = \frac{\dot{m}}{2\pi L_w \kappa} \left(\frac{\mu_w}{\rho_w}\right) \ln \frac{D_{outer,w}}{D_{inner,w}} \quad (43)$$

where  $\kappa$  is the wick permeability and  $\mu_w$  is the viscosity of fluid within the wick.

A check is then done to ensure that the total pressure drop is less than the capillary pressure drop. Calculating the surface tension ( $\sigma$ ) using REFPROP, and assuming a contact angle ( $\theta$ ) of 30 degrees, the maximum capillary pressure is determined using

$$P_{cap} = \frac{2\sigma \cos \theta}{R_{pore}} \quad (44)$$

where  $R_{pore}$  is the wick pore radius.

Finally, the fluid charge in the loop is checked to identify if the CC dried out. After calculating the total fluid mass and determining the fluid that remains in the CC, the quality in the CC ( $X_{cc}$ ) determined from the mean value of density for two-phase flow:

$$\frac{1}{\rho_{cc}} = \frac{X_{cc}}{\rho_{cc,vap}} + \frac{(1 - X_{cc})}{\rho_{cc,liq}} \quad (45)$$

where liquid ( $\rho_{cc,liq}$ ) and vapour ( $\rho_{cc,vap}$ ) CC densities are determined using REFPROP assuming saturated liquid and saturated vapour respectively, and the CC density ( $\rho_{cc}$ ) is calculated using the total fluid remaining in the CC ( $m_{cc}$ ) and the CC volume ( $V_{cc}$ ).

$$\rho_{cc} = \frac{m_{cc}}{V_{cc}} \quad (46)$$

If the CC quality is greater than 0.75, the CC is assumed to have dried out.

### 5.3 PRESSURE DROP

The pressure of the fluid at the next junction ( $j + 1$ ) is calculated based on momentum conservation, knowing the fluid pressure at the past junction ( $j$ ) and the frictional pressure loss introduced across the cell. Depending on the phase of the fluid (liquid, vapour, or two-phase), REFPROP is used to calculate the viscosity at the current junction in one of two ways. If the fluid is purely liquid or vapour, the known temperature and pressure is used to calculate the viscosity. If the fluid is a mix of both, the two-phase viscosity is calculated assuming a homogeneous mix and using

$$\mu_{2ph} = \left( \frac{X_j}{\mu_{vap}} + \frac{1 - X_j}{\mu_{liq}} \right)^{-1} \quad (47)$$

where  $\mu_{vap}$  and  $\mu_{liq}$  are the saturated vapour and liquid viscosities at the known temperatures, and  $X_j$  is the fluid quality [21].

The frictional pressure is calculated using the Churchill correlation for the friction factor ( $f$ ) shown in Eq. 48 which is valid for laminar, transient and turbulent flow [22].

$$f = 8 \left[ \left( \frac{8}{Re} \right)^{12} + \frac{1}{(A+B)^{\frac{3}{2}}} \right]^{\frac{1}{12}} \quad (48)$$

$A$  and  $B$  in the equation above are calculated using the two correlations below [22], assuming a smooth pipe with surface roughness ( $\varepsilon$ ) of 0, and the Reynolds number ( $Re$ ) is defined by Eq. 51 where  $L_c$  is the characteristic length equal to the internal diameter of the pipe [23].

$$A = \left\{ 2.457 \ln \left[ \frac{1}{\left( \frac{7}{Re} \right)^{0.9} + 0.27 \frac{\varepsilon}{D}} \right] \right\}^{16} \quad (49)$$

$$B = \left( \frac{37530}{Re} \right)^{16} \quad (50)$$

$$Re = \frac{\rho V L_c}{\mu_{2ph}} \quad (51)$$

Finally, the frictional pressure loss is calculated using Eq. 52 and subbed into Eq. 53 to calculate the pressure at the next junction.

$$\Delta P_{friction} = \frac{4f\rho u^2}{2} D\pi L_c \quad (52)$$

$$P_{i+1} = \frac{(P_i A_i - \Delta P_{friction})}{A_{i+1}} \quad (53)$$

## 5.4 IN-TUBE HEAT TRANSFER COEFFICIENT

Because of the different behaviour of the heat transfer coefficient depending on the fluid phase (liquid, two-phase, or vapour), two different approaches are used to calculate this parameter. The first method is discussed in Section 5.4.1 and applies to single phase fluid (i.e. purely liquid or vapour) and the second method is discussed in Section 5.4.2 and applies to two-phase fluid. To smoothen the transition between the different heat transfer coefficient behaviours between fluid phases, smoothing functions near the boundaries are implemented as described in Section 5.4.3.

### 5.4.1 Single-Phase Fluid

The heat transfer coefficient between the fluid and solid is calculated using Eq. 54 from the characteristic length ( $L_c$ ), Nusselt number ( $Nu$ ) and thermal conductivity ( $k$ ) [24].

$$h = Nu \frac{k}{L_c} \quad (54)$$

The Nusselt number takes different forms depending on whether the flow is laminar or turbulent. First, in laminar flow inside a circular tube and assuming a fully developed flow with constant viscosity, the Nusselt number can be calculated analytically as either 3.66 or 4.36 under uniform surface temperature and uniform surface heat flux conditions respectively [23]. As a result, the mean between both values is used in this model.

$$Nu_{lam} = \frac{3.66 + 4.36}{2} \quad (55)$$

For a turbulent flow, the Nusselt number is calculated using the Gnielinski correlation [23] [25]:

$$Nu_{turb} = \frac{\left(\frac{f}{8}\right) (Re - 1000) Pr}{1 + 12.7 \left(\frac{f}{8}\right)^{\frac{1}{2}} \left(Pr^{\frac{2}{3}} - 1\right)} \quad (56)$$

where  $f$  is the friction factor which is calculated using Eq. 48 – Eq. 51,  $Pr$  is the Prandtl number which must lie within the range of  $[0.5 < Pr < 2000]$  and  $Re$  is the Reynolds number in the range of  $[3000 < Re < 5 \times 10^6]$ . To determine the Prandtl number, Eq. 57 is using the fluid specific heat at constant pressure ( $c_p$ ), viscosity ( $\mu$ ) and thermal conductivity ( $k$ ).

$$Pr = \frac{c_p \mu}{k} \quad (57)$$

### 5.4.2 Two-Phase Fluid

The method used to calculate the ammonia in-tube condensation heat transfer coefficient discussed below is based on work done by Park and Hrnjak [26], who developed the empirical correlation shown in Eq. 58 based on measured NH<sub>3</sub> in-tube condensation heat transfer:

$$h_{in-tube} = 9.803 \cdot 10^{-4} \left[ \frac{4G(1-X)\delta}{(1-\alpha)\mu_{liq}} \right]^{0.79} \text{Pr}_l^{0.3} \left( \frac{k_{liq}}{\delta} f_i \right) \left( \frac{2\pi - \theta}{2\pi} \right) + 0.279 \left[ \frac{\rho_{liq}(\rho_{liq} - \rho_{vap})g\lambda k_l^3}{\mu_{liq}D(T_{sat} - T_{wall})} \right]^{0.25} \left( \frac{\theta}{2\pi} \right) \quad (58)$$

where  $G$  is the mass flux,  $X$  is the fluid quality,  $\delta$  is the liquid film thickness,  $\alpha$  is the void fraction,  $f_i$  is the interfacial roughness correction factor,  $\theta$  is the angle in a tube where stratified liquid does not flow at a stratified flow region,  $D$  is the tube diameter, and  $\lambda$  is the latent heat of vaporization [26].

To calculate most of the parameters required to evaluate Eq. 58, the flow pattern must be identified as one of three possibilities: annular, stratified-wavy, and stratified as show below.

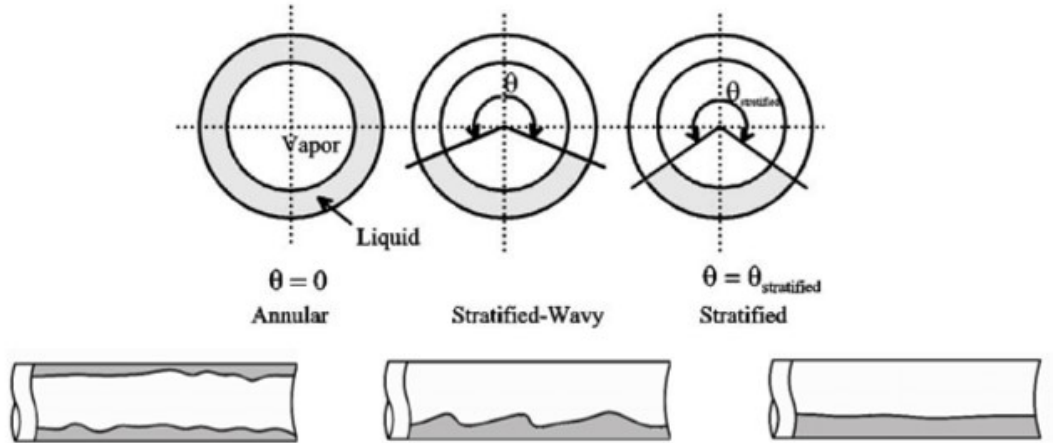


Figure 44: Flow Patterns Schematic (modified) [26] [27]

To identify the flow pattern, Eq. 59 to Eq. 61 are first used to determine the void fraction using fluid surface tension ( $\sigma$ ) and liquid and vapour densities ( $\rho_{liq}$  and  $\rho_{vap}$ ), respectively [26] [28]:

$$\alpha_{homo} = \left[ 1 + \left( \frac{1-X}{X} \right) \frac{\rho_{vap}}{\rho_{liq}} \right]^{-1} \quad (59)$$

$$\alpha_{drift} = \frac{X}{\rho_{liq}} \left[ \{1 + 0.12(1-X)\} \left( \frac{X}{\rho_{vap}} - \frac{1-X}{\rho_{liq}} \right) + \frac{1.18(1-X)[g\sigma(\rho_{liq} - \rho_{vap})]^{0.25}}{G\rho_{liq}^{0.5}} \right]^{-1} \quad (60)$$

$$\alpha = \frac{\alpha_{homo} - \alpha_{drift}}{\ln\left(\frac{\alpha_{homo}}{\alpha_{drift}}\right)} \quad (61)$$

From the cross-sectional area ( $A$ ) of the tube, additional geometrical parameters that are later used can be directly calculated using:

$$A_{liq} = A(1 - \alpha) \quad , \quad A_{vap} = A\alpha \quad , \quad A_{liq,d} = \frac{A_{liq}}{d^2} \quad , \quad A_{vap,d} = \frac{A_{vap}}{d^2} \quad (62)$$

where  $A_{liq}$  and  $A_{vap}$  are the corresponding cross-sectional areas occupied by the liquid and vapour as illustrated in the Figure 45.

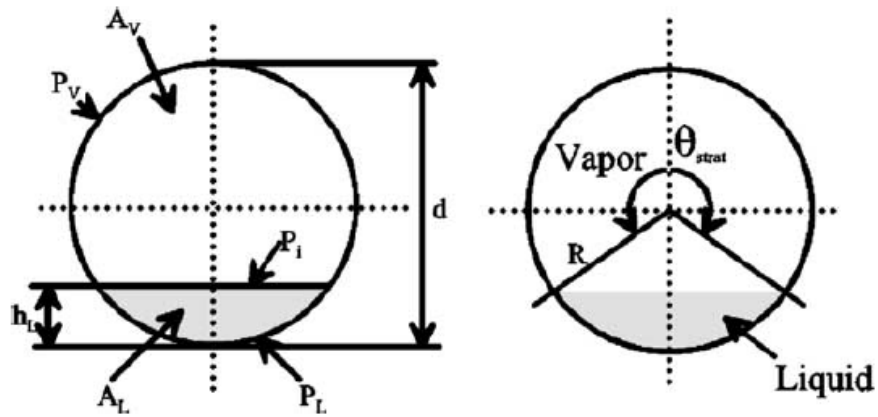


Figure 45: Geometrical parameters for two-phase flow in a circular tube [28].

The stratified angle (see figure above) is calculated by Eq. 63 [26] [29], which is then used to calculate the height of the stratified liquid ( $h_{Ld}$ ) and the length of the interface ( $P_{id}$ ), parameterized by the pipe diameter [28].

$$\begin{aligned} \theta_{strat} = & 2\pi - 2\{\pi(1 - \alpha) \\ & + (3\pi/2)^{1/3}[1 - 2(1 - \alpha) + (1 - \alpha)^{1/3} - \alpha^{1/3}] \\ & - 1/200(1 - \alpha)\alpha[1 - 2(1 - \alpha)][1 + 4(1 - \alpha)^2 \\ & + \alpha^2]\} \end{aligned} \quad (63)$$

$$h_{Ld} = 0.5 \left( 1 - \cos \left( \frac{2\pi - \theta_{strat}}{2} \right) \right) \quad (64)$$

$$P_{id} = \sin \left( \frac{2\pi - \theta_{strat}}{2} \right) \quad (65)$$

The flow pattern present in the pipe is determined based on the mass flux and quality of the fluid as shown by the regions highlighted in Figure 46. For the model to identify whether the flow is annular, stratified-wavy, or fully stratified flow, Eq. 63 to Eq. 65 are evaluated at qualities ranging from 0.05 to 0.95, and used to calculate the stratified flow transition mass flux ( $G_{strat}$ ), and wavy flow transition mass flux ( $G_{wavy}$ ) [28]. Given that only the condensation heat transfer coefficient is to be used, the minimum value of  $G_{wavy}$  is identified and then extrapolated on horizontally to the vapour quality of 1.0, as shown in Figure 46.

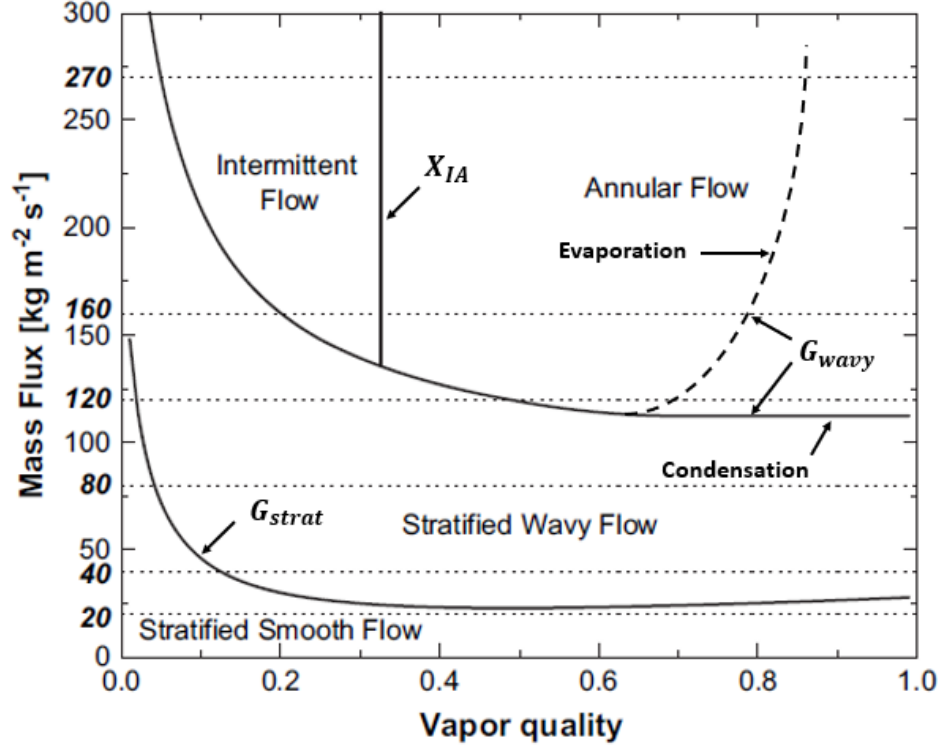


Figure 46: Predicted  $\text{NH}_3$  flow pattern map (modified) [26]

$$G_{strat} = \left\{ \frac{226.3^2 A_{liq,d} A_{vap,d}^2 \rho_{vap} (\rho_{liq} - \rho_{vap}) \mu_{liq} g}{X^2 (1-X) \pi^3} \right\}^{1/3} + 20X \quad (66)$$

$$G_{wavy} = \left\{ \frac{16 A_{vap,d}^3 g d \rho_{liq} \rho_{vap}}{X^2 \pi^2 (1 - (2h_{Ld} - 1)^2)^{0.5}} \left[ \frac{\pi^2}{25 h_{Ld}^2} \times \left( \frac{We}{Fr} \right)_l^{-1.023} + 1 \right] \right\}^{0.5} \quad (67)$$

$$+ 50 - 75 e^{-(x^2 - 0.97)^2 / X(1-X)}$$

The equation above makes use of the liquid Weber number and liquid Froude number which represent the ratio between inertial force and the surface tension force and the ratio of inertial force to the weight of the fluid, respectively [30]. The ratio of both these dimensionless parameters is calculated using [28].

$$\left( \frac{We}{Fr} \right)_l = \frac{g D^2 \rho_{liq}}{\sigma} \quad (68)$$

Finally, the angle  $\theta$  is calculated using Eq. 69 for annular flow, Eq. 70 for stratified wavy flow, and Eq. 71 for fully stratified flow. The liquid film

thickness ( $\delta$ ) is calculated using Eq. 72 for all three flow patterns, and Eq. 73 is used to calculate the interfacial roughness correction factor for annular and stratified wavy flow, and Eq. 74 for fully stratified flow [26] [29].

$$\theta = 0 \quad (69)$$

$$\theta = \theta_{strat} \left( \frac{G_{wavy} - G}{G_{wavy} - G_{strat}} \right) \quad (70)$$

$$\theta = \theta_{strat} \quad (71)$$

$$\delta = \frac{D}{2} \left\{ 1 - \left[ 1 - 2\pi \left( \frac{1 - \alpha}{2\pi - \theta} \right) \right]^{0.5} \right\} \quad (72)$$

$$f_i = 1 + \left( \frac{u_{vap}}{u_{liq}} \right)^{0.5} \left( \frac{(\rho_{liq} - \rho_{vap})g\delta^2}{\sigma} \right)^{0.25} \quad (73)$$

$$f_i = 1 + \left( \frac{u_{vap}}{u_{liq}} \right)^{0.5} \left( \frac{(\rho_{liq} - \rho_{vap})g\delta^2}{\sigma} \right)^{0.25} \left( \frac{G}{G_{strat}} \right) \quad (74)$$

where  $\left( \frac{u_{vap}}{u_{liq}} \right)$  is the phase velocity, and is calculated from [29]

$$\left( \frac{u_{vap}}{u_{liq}} \right) = \frac{X}{1 - X} \left( \frac{\rho_{liq}}{\rho_{vap}} \right) \left( \frac{1 - \alpha}{\alpha} \right) \quad (75)$$

### 5.4.3 Transition Regimes

Two distinct smoothing functions were implemented for the transition regions, one used at the liquid-to-two-phase transition region ( $0 > X > 0.2$ ) and the other at the two-phase-to-vapour region ( $0.95 > X > 1$ ), to avoid large discontinuities in the heat transfer coefficient across the vapour quality and improve the stability of the steady-state model. The boundaries specified for the transition periods were determined through trial and error.

At the liquid to two-phase transition region, Eq. 76 is used to obtain the maximum heat transfer coefficient between the single phase (liquid) and two-phase HTC. This avoids situations such as the heat transfer coefficient at the quality near zero being less than the value at a quality of zero.

$$h_{liq,2ph} = (h_{liq}^{16} + h_{2ph}^{16})^{1/16} \quad (76)$$

At the two-phase to vapour transition region, a cubic spline is generated to interpolate between the single phase (vapour) HTC at a quality of 1 and the two-phase HTC at a quality of 0.95. The resulting heat transfer distribution, applied to the steady-state model, can be seen in Figure 47 below.

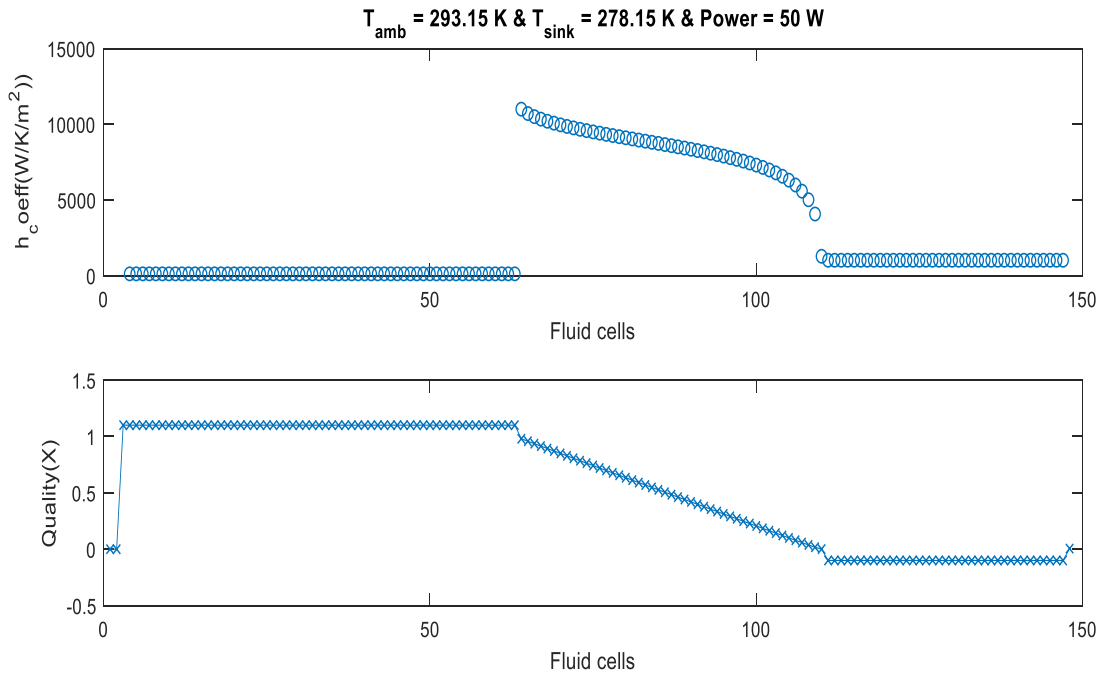


Figure 47: Steady-State Model Heat Transfer Coefficient Distribution along LHP

## 5.5 RESULTS & VALIDATION OF MODEL WITHOUT PRV

The results obtained from the mathematical model before implementing the two-way PRV are shown in Section 5.5.1 and validated in Section 5.5.2. Validation is done by comparing the model behaviour to experimental results previously obtained at Carleton University and published in [19].

### 5.5.1 Results

The results shown below were produced by running the steady-state model with the LHP parameters that are shown in Table 1 and with case-to-wick and wall-to-sink heat transfer coefficients of  $10,000 \text{ Wm}^{-2}\text{K}^{-1}$  and  $250 \text{ Wm}^{-2}\text{K}^{-1}$  respectively. The ambient temperature was set to  $24.7 \text{ }^\circ\text{C}$  and the sink temperatures was set to  $14.3 \text{ }^\circ\text{C}$ .

Figure 48 below shows the resulting performance curve produced by varying the applied power from  $1 \text{ W}$  to  $200 \text{ W}$  at the evaporator. Interface, CC, and vapour line temperatures are observed to behave together, displaying an initial decrease in temperature as the mass flow rate increases and fluid in the transportation lines is exposed to ambient temperatures for shorter periods. At powers greater than  $17.5 \text{ W}$ , interface, CC and vapour line temperatures start increasing which, as explained in Section 2.2, is due to the condenser being fully utilized and no longer able to dissipate larger amounts of energy. As seen below, condenser outlet temperatures stay near sink temperatures until  $17.5 \text{ W}$ , at which point temperatures increase and eventually match CC temperatures. This is a clear indication of the condenser being fully open and no longer able to reduce the fluid temperature to the sink temperature.

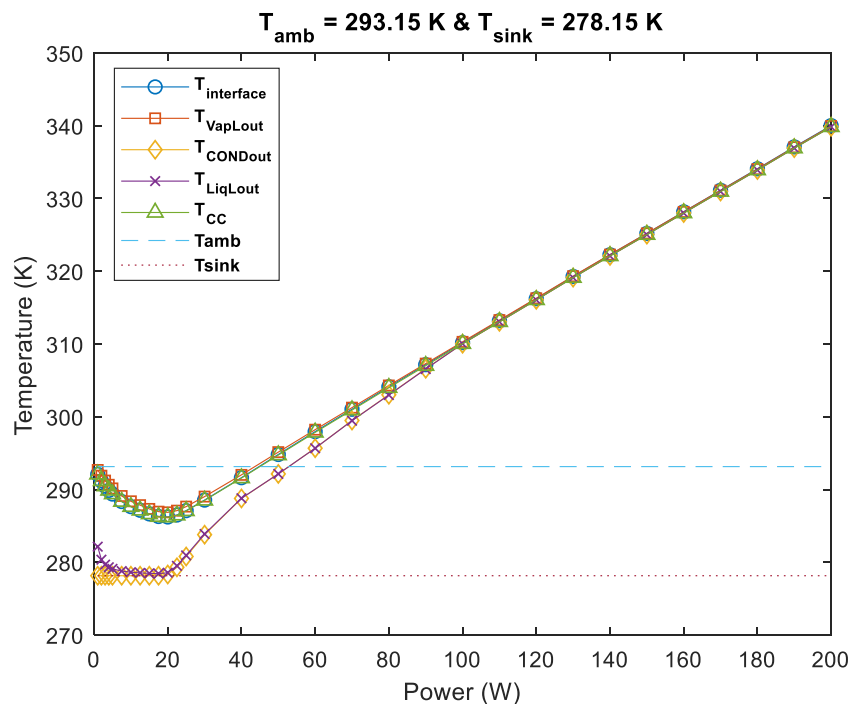


Figure 48: Steady-State Model Performance Curve

Figure 49 and Figure 50 show fluid and solid cell temperatures along the LHP for 15 W and 110 W, respectively, and how the vapour quality changes within the LHP. Based on the geometry of the LHP and the model discretization technique, cells 1 – 3 correspond to the evaporator, 4 – 63 to the vapour line, 64 – 111 to the condenser, 112 – 147 to the liquid line, and 148 to the CC.

Figure 49 is an example of the LHP operating at low heat loads with the condenser not being fully open (resulting in the subcooling of fluid). Within the condenser, fluid cell temperatures remain constant between 64 and 92 as the fluid changes state from vapour to liquid (quality constantly decreasing). By cell 93, the fluid is entirely liquid, and temperatures drop as it is being subcooled to temperatures near the sink temperature. In contrast, Figure 50 shows a fully utilized condenser where the heat load is large enough that the fluid cannot be converted entirely from vapour to liquid, and the temperature remains constant throughout the entire condenser.

In Figure 49, fluid and solid cell temperatures gradually increase along both vapour and liquid lines. This demonstrates the effect that the parasitic heat exchange from ambient has on LHP temperatures when ambient temperatures are greater than fluid temperatures. Because the mass flow rate increases with increasing heat loads, this effect is much more noticeable at 15 W (Figure 49) as opposed to 110 W (Figure 50) where temperatures along the transportation lines seem constant throughout. Higher mass flow rates mean that the fluid is exposed to parasitic heat exchange for lower periods of time, causing a lesser change in temperature.

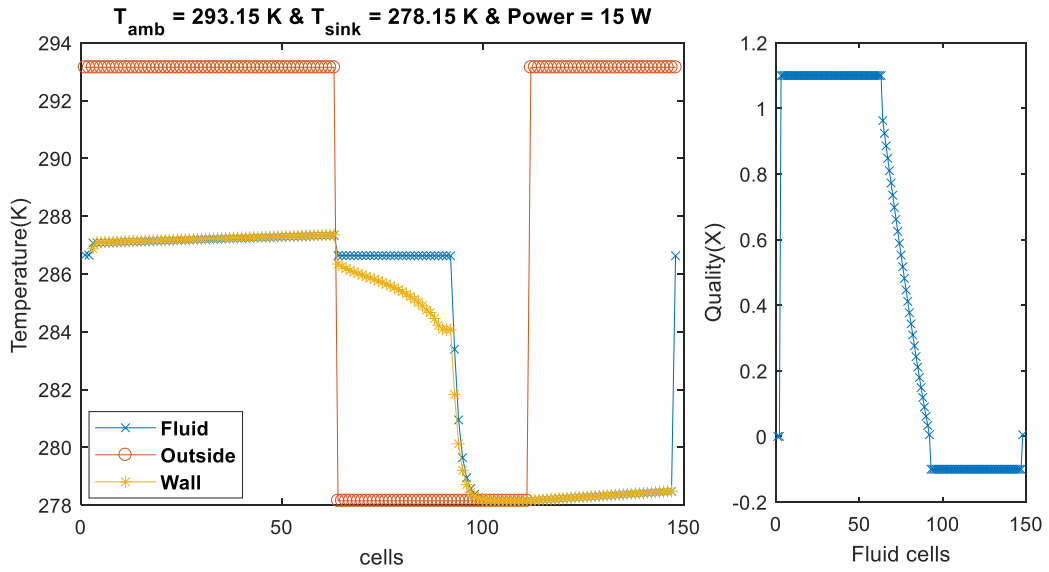


Figure 49: Steady-State Model Temperature and Quality at discretized LHP locations at 15 W

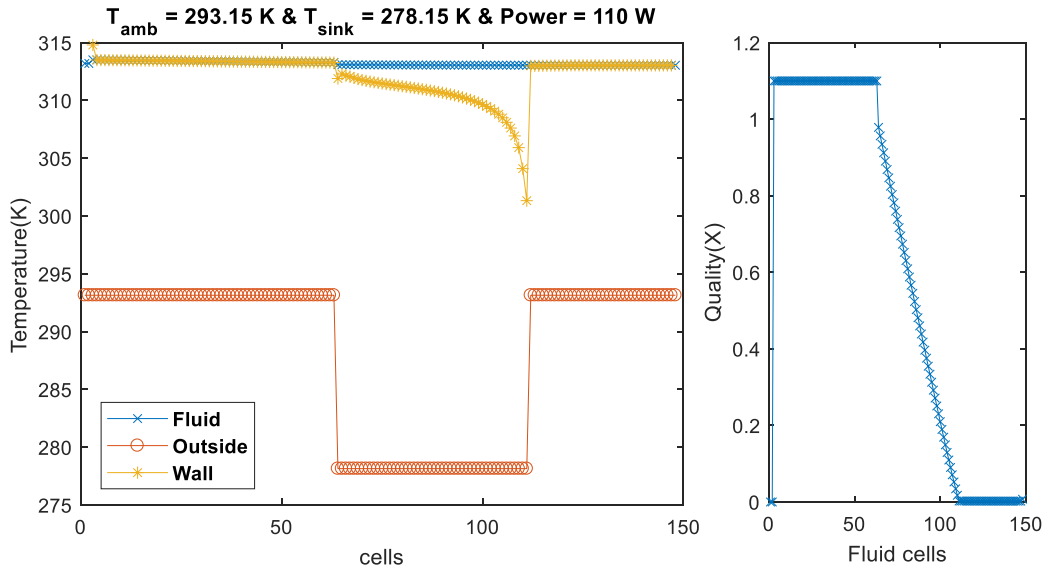


Figure 50: Steady-State Model Temperature and Quality at discretized LHP locations at 110 W

### 5.5.2 Experimental Validation

Given the complex geometry of the IE LHP and many unknown proprietary parameters surrounding the PRV, experimental validation was done using results from a LHP with a more simplified geometry and a horizontal condenser. Steady-state model parameters were modified to match the physical properties and geometry of the simplified LHP. These parameters can be found in [19] along with details regarding the experimental setup.

As seen in Figure 51, the performance curve produced by the steady-state model agrees with both experimental results obtained by Kaya et al. [19]. These results were obtained by setting the case-to-wick heat transfer coefficient to  $10,000 \text{ Wm}^{-2}\text{K}^{-1}$  and a wall-to-sink heat transfer coefficient of  $2,500 \text{ Wm}^{-2}\text{K}^{-1}$ . Ambient and sink temperatures were set to  $24.7 \text{ }^\circ\text{C}$  and  $14.3 \text{ }^\circ\text{C}$ , respectively. Comparing steady-state to experiment 1 results (shown in blue) produce a maximum relative difference in evaporator temperature of  $4.6 \%$ , where comparison to experiment 2 (shown in red) produces a maximum relative difference of  $2.9 \%$ . Based on these errors, it can be stated that the results produced by the mathematical model can properly describe the steady-state behaviour of LHPs. It should be noted that there is an uncertainty for the exact values of both heat transfer coefficients (case-to-wick and wall-to-sink). These parameters were varied within expected range to obtain a good match between model and experimental results. Once a calibration is done for a given case, the model can be used to predict the LHP behaviour for other conditions.

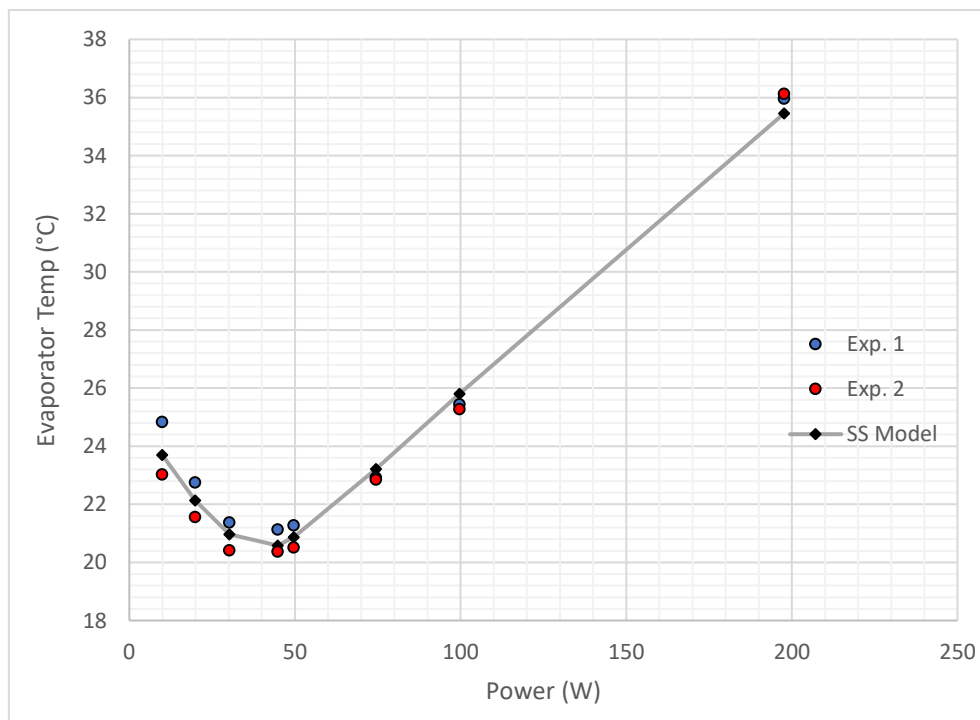


Figure 51: Experimental vs. model results

## 5.6 PRV IMPLEMENTATION AND RESULTS

To model the effects of the two-way PRV, a function that introduces a pressure drop at the location of the PRV was derived from experimental results obtained using the IE LHP. The function was designed in such a way that the pressure drop (and hence performance degradation) mimics the valve position at a given power since modeling of the PRV directly was not possible due to the design parameters of the PRV being proprietary.

To obtain the function, an additional pressure drop term was introduced just after the entrance of the vapour line in the transportation line algorithm. The pressure drop was manually adjusted for input powers below 140 W such that the evaporator casing temperature would match the average evaporator temperatures recorded using the IE LHP (31 °C). This process is illustrated in Figure 52, which shows the results of manually adjusting the pressure drop (at values less than 140 W) such that the standard mathematical model (shown in red) outputs evaporator casing temperatures near the experimental results (blue).

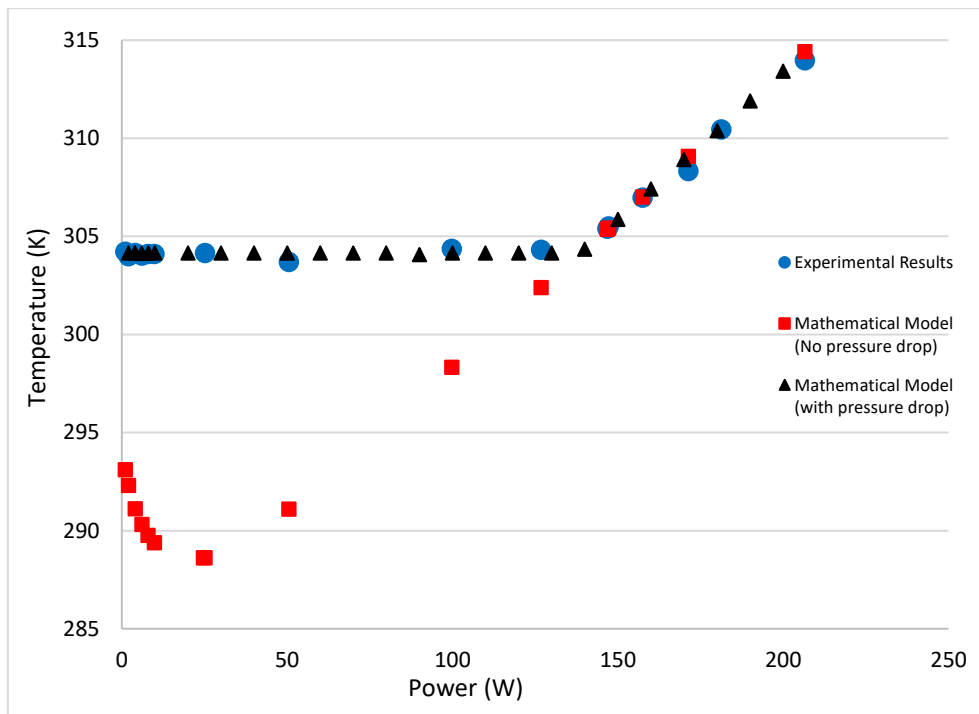


Figure 52: Standard Model vs Pressure Adjusted Results

Having determined the pressure drop values which cause the model evaporator temperature to match the experimentally recorded casing temperatures, a pressure vs. input power function was determined by means of a 3<sup>rd</sup>-order polynomial regression as shown in Figure 53. This resulted in the function shown in Eq. 77 which was implemented in the steady-state model.

$$P_{PRV,drop} = 0.0033P^3 - 3.8272P^2 + 452.51P + 2300.6 \quad (77)$$

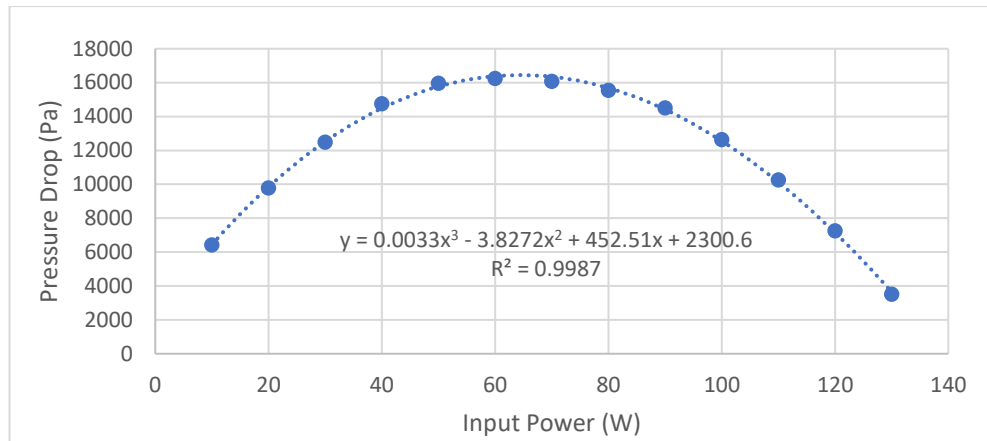


Figure 53: Derived PRV Pressure Drop Law

The additional pressure drop caused by the PRV was only modelled for input powers below 140 W because, as can be seen in Figure 52, the LHP operates in constant conductance mode at powers higher than this value. This implies that the valve is fully open, although, it also assumes that the valve does not produce any pressure drop when fully open. The results from implementing the above function in the steady-state model can be found in the figure below.

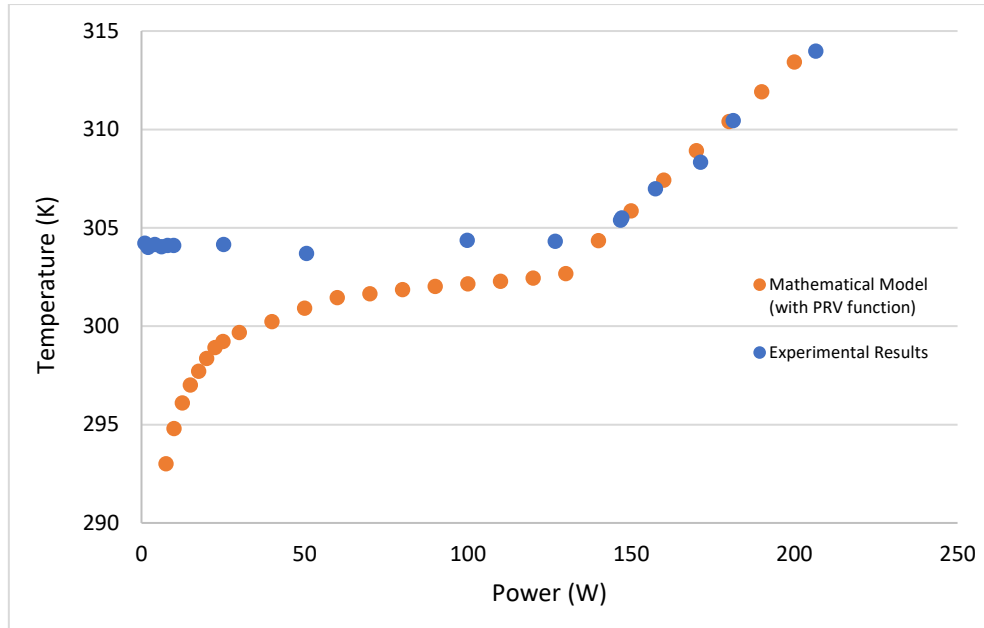


Figure 54: Mathematical Model with PRV effect modelled

As seen above, the obtained law for the PRV did not result in the evaporator casing temperatures matching the expected trend shown in Figure 52. With the coefficient of determination of the 3<sup>rd</sup>-order polynomial being 0.9987, results indicate that the mathematical model is very sensitive to small differences in fluid pressures, and a function that estimates a pressure drop due to the PRV will not produce accurate results due to the nature of the approximation. A small difference in fluid pressure causes large differences in fluid and solid cell temperatures and hence it would be necessary to precisely model pressure drops produced by the PRV. Given the lack of information regarding the PRV due to its proprietary nature (including back pressure, valve geometry, orifice size, etc.), a differential pressure transducer would be required to find the law of the PRV. Using measured casing temperatures and the mathematical model does not produce results that are accurate enough for obtaining the PRV law to be feasible.

# CHAPTER 6 CONCLUSIONS AND RECOMMENDATIONS

## 6.1 CONCLUSIONS

The start-up behaviour of the LHP with a two-way PRV was tested at various power levels. At low powers, a start-up was observed at temperatures below the valve setpoint, due to the presence of an orifice in the PRV. This premature start-up was found to be unsustainable due to large mass flow restrictions imposed by the closed PRV. A second, sustainable start-up is finally achieved once the average evaporator temperature reached 31 °C and the PRV is opened. Although this start-up behaviour was observed at higher powers, it became less noticeable as evaporator temperatures rise quicker, eventually avoiding the first unsustainable start-up. By applying step increases in applied power, it was possible to identify that the PRV loses its ability to regulate evaporator temperatures at powers greater than 130 W at a sink temperature of 5 °C. After this point, vapour line and evaporator temperatures increase with increasing power and the LHP was observed to behave in constant conductance mode. While the power was below 130 W, the LHP was seen to regulate evaporator and compensation chamber temperatures to  $(30.49 \pm 0.17)$  °C and  $(31.28 \pm 0.18)$  °C, respectively. In the presence of changing sink temperatures, the LHP was found to better maintain evaporator temperatures at low powers. At a sink temperature of 15 °C, variations of 1.69 °C were observed at a power of 100 W, in contrast to 0.43 °C at 10 W. In both power cycling (at constant sink temperature) and sink cycling (at constant power), large temperature

oscillations were observed in the condenser and liquid line caused by the vapour-to-liquid interface moving between both these sections. These oscillations were observed to affect the LHPs ability to reach steady-state (constant component temperatures), with minor fluctuations in the evaporator and compensation chamber.

A mathematical model capable of solving for the steady-state behaviour of a LHP was developed. When compared to two different experiments conducted on a simple LHP with a horizontal condenser, the model produced results with a maximum relative error of 4.6 %. An attempt to derive a law for describing the effects of the two-way PRV on the LHP was made based on experimental observations on the IE LHP. It was found that introducing an additional pressure drop in the vapour line simulates the opening/ closing of the PRV; nevertheless, given the model's sensitivity to fluid pressure, an overall equation for pressure drop as a function of power does not produce accurate results. It can be concluded that, without knowledge of the PRV design parameters, it is not feasible to determine a law for its behaviour exclusively using measured external temperatures and the mathematical model. It would be necessary to install a differential pressure transducer in the LHP to determine a sufficiently accurate correlation for the mathematical model.

## **6.2 RECOMMENDATIONS FOR FUTURE WORK**

Based on the results obtained through this project, the following recommendations were made for future work.

### **6.2.1 Experimental Setup**

While the equipment available in the LHP laboratory at Carleton University and the experimental setup was adequate to test the overall behaviour and operational characteristics of the IE LHP, improvements can be made to more accurately test and quantify the LHP performance. These include:

- Acquiring a chiller capable of cooling the circulating fluid to lower temperatures so as to test the LHP performance at lower sink temperatures which would also allow testing at higher powers;

- Improve the data acquisition system such that temperature values can be individually examined through the course of each test to quantitatively determine when the LHP has reached steady-state;
- Route voltage and current readings to the DAS to automate the recording of power values against thermocouple readings;
- Automate power cycling to enable more repeatable results; and
- Design and build an environmental chamber to insulate the LHP from changes in ambient temperature and mitigate changes in conditions due to random forced convection during each test. Ideally, the chamber would be able to control ambient temperature.

### 6.2.2 LHP Testing

Further testing may be performed in several new areas, including:

- Studying the effect of varying ambient temperatures;
- Studying the effects of changes in elevation and tilt;
- Studying the effects of small power increments at low powers;
- Studying the effects of rapid sink temperature cycling on the LHPs capability to regulate temperatures; and
- Perform a series of dry-out tests to identify LHP operating limits.

### 6.2.3 Mathematical Modeling

The presented mathematical model has shown to produce accurate estimates of the LHP behaviour when compared to experimental data. Further advances that can be made to improve results include:

- Implementing a model for calculating the in-tube heat transfer coefficient for the boiling condition;
- Incorporating the effects of elevation and tilt on LHP operation;
- Investigating the definition of the PRV law using other parameters such as velocity;
- Implementing an algorithm for the modeling of the PRV given all PRV design parameters are known;
- Performing a parametric study of the LHP performance characteristics to further determine the model capabilities.

## REFERENCES

- [1] A. Torres, D. Mishkinis and T. Kaya, "Mathematical modeling of a new satellite thermal architecture system connecting the east and west radiator panels and flight performance prediction," *Applied Thermal Engineering*, vol. 65, pp. 623-632, 2014.
- [2] D. Reay, P. Kew and R. McGlen, *Heat Pipes Theory, Design and Applications*, Oxford: Butterworth-Heinemann, 2014.
- [3] J. Deverall and J. Kemme, "USAEC Report LA - 3278, Contract W-7405-eng-36 Satellite Heat Pipe," California, 1970.
- [4] Y. F. Maydanik, "Loop Heat Pipes," *Applied Thermal Engineering*, no. 25, pp. 635 - 657, 2005.
- [5] J. Ku, "Operating Characteristics of Loop Heat Pipes," in *29 International Conference on Environmental System*, Denver, Colorado, 1999.
- [6] T. Kaya and J. Ku, "A Parametric Study of Performance Characteristics of Loop Heat Pipes," SAE Technical Paper Series, Colorado, 1999.
- [7] J. He, J. Miao, L. Bai, G. Lin, H. Zhang and D. Wen, "Effect of Non-Condensable Gas on the Startup of a Loop Heat Pipe," *Applied Thermal Engineering*, no. 111, pp. 1507-1516, 2017.
- [8] S. Vershinin and Y. Maydanik, "Investigation of Pulsations of the Operating Temperature in a Miniature Loop Heat Pipe," *International Journal of Heat and Mass Transfer*, no. 50, pp. 5232-5240, 200.
- [9] T. Kaya and D. Mishkinis, "Accurate Temperature Control Using Heat Pipes," *International Review of Mechanical Engineering*, vol. xx, no. x, 2008.
- [10] A. Torres, D. Mishkinis, A. Kulakov, F. Romera, C. Gregori and T. Kaya, "Thermal Control of Loop Heat Pipe with Pressure Regulating Valve," IberEspacio Tecnologia Aeroespacial, Madrid.
- [11] A. Torres, "Numerical Investigation and Experimental Validation of a Novel Thermal Architecture for Spacecraft Thermal Management," Carleton University, Ottawa, 2014.
- [12] Keithley Instruments, Inc. , *Integra Series Multimeter/Switch Systems*, 2003.
- [13] A. Siddiqui, "An Experimental and Numerical Investigation of Capillary Limit in an Arterial Heat Pipe," Carleton University , Ottawa, 2009.

- [14] T. Kaya and A. Siddiqui, "Mathematical Modeling of an Arterial Heat Pipe with Excess Fluid Charge," *Applied Thermal Engineering*, vol. 30, pp. 2019-2025, 2010.
- [15] H. W. Coleman and W. G. Steele, *Experimentation, Validation and Uncertainty Analysis for Engineers*, New Jersey: John Wiley & Sons, Inc., 2009.
- [16] A. Torres, D. Mishkinis and T. Kaya, "Mathematical Model Validation of a Thermal Architecture System Connection East/West Radiators by Flight Data," *Applied Thermal Engineering*, vol. 66, pp. 1-14, 2014.
- [17] T. Kaya and T. T. Hoang, "Mathematical Modeling of Loop Heat Pipes and Experimental Validation," *Journal of Thermophysics and Heat Transfer*, vol. 13, no. 3, pp. 314-320, 1999.
- [18] M. Nishikawara, H. Nagano and T. Kaya, "Transient Thermo-fluid Modeling of Loop Heat Pipes and Experimental Validation," *Journal of Thermophysics and Heat Transfer*, vol. 27, no. 4, pp. 641-647, 2013.
- [19] T. Kaya, R. Perez, C. Gregori and A. Torres, "Numerical Simulation of Transient Operation of Loop Heat Pipes," *Applied Thermal Engineering*, vol. 28, no. 8, pp. 967-974, 2008.
- [20] J. Holman, *Heat Transfer*, NY: McGraw-Hill, 1997.
- [21] M. Awad and Y. Muzychka, "Effective Property Models for Homogeneous Two-Phase Flows," *Experimental Thermal and Fluid Science*, vol. 33, no. 1, pp. 106-113, 2008.
- [22] S. Churchill, "Friction Factor Equation Spans all Fluid-flow Regimes," *Chem. Eng.*, vol. 84, no. 24, pp. 94-95, 1977.
- [23] T. Bergman, A. Lavine, F. Incropera and D. DeWitt, *Fundamentals of Heat and Mass Transfer*, 7th ed., NY: John Wiley & Sons, 2010.
- [24] D. Edwards and V. M. A. Deny, *Transfer Processes*, 2nd ed., Washington DC: Hemisphere Pub. Corp, 1979.
- [25] V. Gnielinski, "New Equations for Heat and Mass Transfer in Turbulent Pipe and Channel Flow," *International Chemical Engineering*, vol. 16, pp. 359-368, 1976.
- [26] C. Y. Park and P. Hrnjak, "NH<sub>3</sub> in-tube Condensation Heat Transfer and Pressure Drop in a Smooth Tube," *International Journal of Refrigeration*, vol. 31, pp. 643-651, 2008.

- [27] G. Montenegro and e. al., "Slug Catcher Multiphase CFD Modelling: Optimization and comparison with Industrial Standards," in *7th International Exergy, Energy and Environment Symposium*, 2015.
- [28] J. El Hajal, J. Thome and A. Cavallini, "Condensation in Horizontal Tubes, Part 1: Two-Phase Flow Pattern Map," *International Journal of Heat and Mass Transfer*, vol. 46, pp. 3349-3363, 2003.
- [29] J. Thome, J. El Hajal and A. Cavallini, "Condensation in Horizontal Tubes, Part 2: New Heat Transfer Model Based on Flow Regimes," *International Journal of Heat and Mass Transfer*, vol. 46, pp. 3365-3387, 2003.
- [30] B. Munson, T. Okiishi, W. Huebsch and A. Rothmayer, *Fundamentals of Fluid Mechanics*, 7th ed., Hoboken, NJ: John Wiley & Sons, 2013.

## APPENDIX A – Wall Temperature Iteration

As the model iterates until the wall temperature values converge, fluid cell temperatures are adjusted using two distinct methods depending on convergence behaviour. Both methods and the necessary conditions for each averaging method are explained below.

At each iteration, the model calculates the difference in wall temperature ( $\Delta T_w$ ) and the corresponding fluid temperature ( $T_F$ ) and keeps track and stores these values for the past iteration ( $\Delta T_{w,past}$  and  $T_{F,past}$ ). These values are calculated using the following equations:

$$\Delta T_w = T_{wall1} - T_{wall2} \quad (A1)$$

$$T_F = \left(1 - \frac{Y\Delta T_w}{T_{wall1}}\right) T_F \quad (A2)$$

where the coefficient  $Y$  is set to 0.4 if iterating in a liquid fluid cell and 0.05 if iterating in a vapour fluid cell. If iterating in a two-phase fluid cell, quality ( $X_F$ ) instead of fluid temperature is used for the iteration scheme, and hence Eq. A3 is used instead of Eq. A2.

$$X_F = X_F - 0.5 \times 10^{-1} \times \text{sign}(\Delta T_w) \quad (A3)$$

Past iteration values are kept stored to determine when there is a sign change in  $\Delta T_w$  which indicates that the convergence point is located between the current iteration and the previous iteration. Making use of the knowledge of the convergence point with respect to past iteration values, the model switches from iterating using Eq. A2 or Eq. A3 to Eq. A4.

$$T_F = \frac{T_{F\Delta T_w}^- \Delta T_w^+ + T_{F\Delta T_w}^+ \Delta T_w^-}{\Delta T_w^- + \Delta T_w^+} \quad (A4)$$

where  $T_{F\Delta T_w}^-$  is the fluid temperature that caused a negative  $\Delta T_w$  (whose absolute value is stored as  $\Delta T_w^-$ ) and  $T_{F\Delta T_w}^+$  is the fluid temperature that caused a positive

$\Delta T_w$  (whose absolute value is stored as  $\Delta T_w^+$ ). The values of each of these variables change during each iteration depending on the changes of sign. Note that if iterating in a two-phase fluid cell, all temperatures in Eq. A4 are replaced by quality, but the equation is of the same form.

## APPENDIX B – Heat Leak Iteration

As the model iterates until the heat leak values converge, the evaporator interface temperature is adjusted using two distinct methods depending on convergence behaviour. Both methods and the necessary conditions for each averaging method are explained below.

At each iteration, the model calculates the difference in heat leak ( $\Delta\dot{q}_{hl}$ ) and the corresponding interface temperature ( $T_{int}$ ) and keeps track and stores these values for the past iteration. These values are calculated using the following equations:

$$\Delta\dot{q}_{hl} = \dot{q}_{hl,w} - [\dot{q}_{hl,e} - \dot{m}(h_j - h_{j+1})] \quad (\text{B1})$$

$$T_{int} = T_{int} + MF \times \text{sign}(\dot{q}_{hl,w} - \dot{q}_{hl,e}) \quad (\text{B2})$$

In Eq. B1, enthalpy values correspond to the junctions that are defined at the boundaries of the wick, and this is done to calculate the conductive heat leak based on the CC heat leak that had been calculated using the energy balance of the CC. A marching factor ( $MF$ ) is used in Eq. B2 so that the amount by which the interface temperature is changed between each iteration depends on the magnitude  $\Delta\dot{q}_{hl}$  so as to speed up convergence. As a result, the marching factor is given a value based on the following formula:

$$MF = \begin{cases} 3 & , \text{if } \Delta\dot{q}_{hl} > 10 \\ 10 \times 10^{|\log \Delta\dot{q}_{hl}|} & , \text{if } 10 > \Delta\dot{q}_{hl} > 10^{-7} \\ 10^{-7} \cdot 0.1 & , \text{if } \Delta\dot{q}_{hl} < 10^{-7} \end{cases} \quad (\text{B3})$$

Past iteration values are kept stored to determine when there is a sign change in  $\Delta\dot{q}_{hl}$  which indicates that the convergence point is located between the current iteration and the previous iteration. Making use of the knowledge of the convergence point with respect to past iteration values, the model switches from iterating using Eq. B2 to Eq. B4.

$$T_{int} = \frac{T_{int\Delta\dot{q}_{hl}}^- \Delta\dot{q}_{hl}^+ + T_{int\Delta\dot{q}_{hl}}^+ \Delta\dot{q}_{hl}^-}{\Delta\dot{q}_{hl}^+ + \Delta\dot{q}_{hl}^-} \quad (\text{B4})$$

where  $T_{int\Delta\dot{q}_{hl}}^-$  is the interface temperature that caused a negative  $\Delta\dot{q}_{hl}$  (whose absolute value is stored as  $\Delta\dot{q}_{hl}^-$ ) and  $T_{int\Delta\dot{q}_{hl}}^+$  is the interface temperature that caused a positive  $\Delta\dot{q}_{hl}$  (whose absolute value is stored as  $\Delta\dot{q}_{hl}^+$ ). The values of each of these variables change during each iteration depending on the changes of sign.